

Nanoscale structural phenomena in perovskite-type relaxor ferroelectrics studied by resonance Raman spectroscopy

MASTERARBEIT

zur Erlangung des Grades

Master of Science

im Studiengang Geowissenschaften

an der Fakultät Mathematik, Informatik und Naturwissenschaften

der Universität Hamburg

vorgelegt von

André Rohrbeck

Referenten:

PD Dr. Boriana Mihailova
Prof. Dr. Ulrich Bismayer

Bearbeitungszeit:

WS 2014/2015 – SS 2015

Nanoscale structural phenomena in perovskite-type relaxor ferroelectrics
studied by resonance Raman spectroscopy

Eidesstattliche Erklärung

Hiermit versichere ich an Eides statt und durch meine Unterschrift, dass die vorliegende Arbeit von mir selbstständig, ohne fremde Hilfe angefertigt worden ist. Inhalte und Passagen, die aus fremden, insbesondere aus Internet-Quellen stammen und direkt oder indirekt übernommen worden sind, wurden als solche kenntlich gemacht. Ferner versichere ich, dass ich keine andere, außer der im Literaturverzeichnis angegebenen Literatur verwendet habe. Diese Versicherung bezieht sich sowohl auf Textinhalte sowie alle enthaltenden Abbildungen, Skizzen und Tabellen. Die Arbeit wurde bisher keiner Prüfungsbehörde vorgelegt und auch noch nicht veröffentlicht. Die auf dem elektronischen Speichermedium eingereichte Fassung entspricht der eingereichten schriftliche Fassung der Arbeit. Ich erkläre mich damit einverstanden, dass ein Exemplar der Abschlussarbeit der Institutsbibliothek zur Verfügung gestellt wird.

Ort, Datum

Unterschrift

Contents

Abstract	VII
List of Figures.....	IX
List of Tables.....	XIII
List of Abbreviations	XV
Acknowledgements	XVII
1 Introduction.....	1
2 Objectives.....	5
3 Methods and theoretical basis.....	7
3.1 Electromagnetic radiation	7
3.2 Lattice dynamics of crystals	8
3.3 Raman spectroscopy	9
3.4 Resonance Raman spectroscopy	12
3.5 Multi-phonon Raman scattering	15
3.6 Group theory analysis and Raman selection rules.....	16
4 Samples and experimental conditions	19
4.1 Samples	19
4.1.1 B-site doping.....	20
4.1.2 A-site doping.....	20
4.2 Experimental conditions	23
5 Results and Discussion	25
5.1 $\text{PbSc}_{0.5}\text{Ta}_{0.5}\text{O}_3$ (PST) & $\text{PbSc}_{0.5}\text{Nb}_{0.5}\text{O}_3$ (PSN) model compounds.....	25
5.1.1 RRS at ambient conditions	25
5.1.2 Selection rules for resonance Raman scattering on perovskites	29
5.1.3 Selection rules for multi-phonon resonance and non-resonance Raman scattering.....	32
5.1.4 RRS at different temperatures	34
5.1.5 RRS at high pressures	36
5.2 Effect of doping	38
5.2.1 RRS at room temperature	38
5.2.2 A-site substitution for Pb by cations with larger ionic radius: the effect of doping with Ba.....	53
5.2.3 A-site substitution for Pb by cations with smaller ionic radius: the effect of doping with La & Sr.....	56
6 Conclusion.....	61

7	References.....	63
8	Appendix.....	69
8.1	Spectra collected under non-resonance conditions ($\lambda = 514.5$ nm).....	69
8.2	Spectra collected under resonance conditions ($\lambda = 325$ nm)	72

Abstract

Resonance Raman spectroscopy with $\lambda = 325$ nm has been applied to study lead-based perovskite-type (ABO_3) relaxor ferroelectric $PbSc_{0.5}Ta_{0.5}O_3$ (PST) and $PbSc_{0.5}Nb_{0.5}O_3$ (PSN) as well as related doped compounds with Bi, Ba, La and Sr, partially substituting for Pb on the A site and compounds with a third type of B-site cation (Nb or Sn substituting for Ta). The excitation with radiation exhibiting energy slightly above the optical absorption edge E_g and corresponding to the maximum of the optical dielectric permittivity as a function of photon energy promotes the enhancement of intrinsic antisymmetric BO_6 bending and stretching vibrations associated with polar LO phonon modes due to Fröhlich interactions as well as the appearance of intense two-phonon scattering from the same vibrations. The performed group theory analysis on the resonance Raman scattering (RRS) allowed in cubic as well as in possible polar and non-polar ferroic phases, together with the temperature dependency of the observed RRS reveals that the enhanced Raman scattering by resonance due to Fröhlich interactions arises exclusively from ferroelectric domains and polar nanoregions (PNR) i.e. polar structural distortions, while the scattering contribution from the average cubic non-polar matrix is below the detection limit upon the experimental setup. The pressure evolution of RRS collected from PST reveals that the polarity of the structure persists up to 10 GPa. Resonance Raman scattering of A- and B-site doped compounds in general follows the previously established trends (by XRD and non-RRS) about the effect of different type of chemical substitution. The Ba-doped compounds were found to show an increased individual polarity while the coherence of polar coupling and thus the formation of ferroelectric long-range order is disturbed, although the overall polarity appears to be strongly increased by small amounts of Ba. A completely different nature of deformation could be found for compounds heavily doped with La or Sr, respectively. In this case, the facilitation of antiphase BO_6 octahedral tilts and the simultaneous suppression of B-cation off-centered shifts leads to a drastic decrease of polarity while the doubling of the unit cell inherently induces a coherent, inferior polarity of symmetric BO_6 stretching vibrations due to the deformation of adjacent BO_6 octahedra by different A-site cation surroundings.

In contrast to previously used methods as non-resonant Raman spectroscopy and XRD, resonance Raman spectroscopy allows to selectively studying the ferroic phases of the perovskite-type relaxor compounds and enables to distinguish between polarity generated by the mean-size of polar structural regions, polarity due to individual local distortion as well as the overall polarity of different compounds.

List of Figures

- Fig. 1: Hysteresis loop of the net polarization (P) as a function of external electric field (E). After all ferroelectric domains are aligned in the same direction (arrows) a saturation of the polarization is reached. By removing the external electric field, a remanent polarization (P_r) still exists. The net polarization can be suppressed to zero by applying a coercive electric field (E_c). 2
- Fig. 2: The aristotype perovskite structure with symmetry $Pm\bar{3}m$ and unit cell parameter a_0 . Large grey sphere at the center of the cube represents the A-site cation. Small, grey spheres at the corners of the cube are B-site cations and white spheres are anions i.e. oxygen atoms. By doubling the structure (8 primitive cubic unit cells in total with unit cell length $2 \times a_0$) changes the symmetry to $Fm\bar{3}m$ (Mihailova, et al., 2008 a). 3
- Fig. 3: a) Sketch of the structural state of Pb-based relaxors at ambient conditions. Competitive polar and antiferrodistortive ferroic order simultaneously exists on a mesoscopic scale, while the average, long-range order shows cubic symmetry (Waesermann, et al., 2013). b) Ferro- plus antiferroelectric order results in a ferrielectric state..... 4
- Fig. 4: Dispersion relation of a one-dimensional, diatomic chain with the phonon angular frequency (ω) as a function of the phonon wavevector (k). The point at $k = 0$ corresponds to the center of the FBZ whereas π/a and $-\pi/a$ represent the boundary of the FBZ with “a” being the unit cell parameter. Acoustic phonons (red) show strong dispersion and $\omega(k)$ becomes zero at the FBZ center. Optical phonons (blue) have non-zero frequency for any wavevector throughout the FBZ..... 8
- Fig. 5: Elastic (Rayleigh) and inelastic (Stokes & anti-Stokes) light scattering and corresponding transitions between vibrational states during the Raman scattering process.10
- Fig. 6: Elastic (Rayleigh) and inelastic (Stokes) light scattering and corresponding transitions between vibrational states under resonance and under non-resonance conditions. In the case of RRS the intermediate state is an eigenstate and not a virtual state.....13
- Fig. 7: Resonance (solid lines) and non-resonance Raman spectra (dashed lines) of PST ($PbSc_{0.5}Ta_{0.5}O_3$), measured in parallel (XX) and cross-polarized (XY) scattering geometry. The peaks arising from antisymmetric bending (AB) and antisymmetric stretching (AS) as well as the corresponding two-phonon scattering (two overtones and one combination) are labelled.

The spectra are vertically shifted for clarity. The non-resonance spectra are normalized by the same coefficient to match the vertical size of RRS.26

Fig. 8: Resonance (solid lines) and non-resonance Raman spectra (dashed lines) of PSN ($\text{PbSc}_{0.5}\text{Nb}_{0.5}\text{O}_3$), measured in parallel (XX) and cross-polarized (XY) scattering geometry. The peaks arising from antisymmetric bending (AB) and antisymmetric stretching (AS) as well as the corresponding two-phonon scattering (two overtones and one combination) are labelled. The spectra are vertically shifted for clarity. The non-resonance spectra are normalized by the same coefficient to match the vertical size of RRS.27

Fig. 9: Splitting of the electron states of B-cation d and oxygen 2p level for the cubic point symmetry ($m\bar{3}m$) representing the non-polar matrix. Additionally, splitting of electron states due to rhombohedral deviation from the ideal cubic structure in the form of polar ferroic ($3m, \bar{3}$) and antiferrodistortive ferroic species ($\bar{3}m, \bar{3}$) is illustrated. In contrast to phonon modes, the irreducible representations of electron states are labeled following the Mulliken notation, but lowercase letters are used instead of uppercase.31

Fig. 10: Temperature dependent parallel and cross-polarized RRS of PST. The spectra are shifted vertically for clarity. On cooling signals start to appear at temperatures near T^*34

Fig. 11: Temperature dependent parallel and cross polarized RRS of PSN. The spectra are shifted vertically for clarity. On cooling signals start to appear at temperatures near T^*35

Fig. 12: Parallel polarized resonance Raman spectra of PST under high pressure at room temperature. The spectra are vertically shifted for clarity. The spectrum at ambient pressure has been collected after decompression.37

Fig. 13: Parallel and cross polarized RRS spectra of PST related compounds. Spectra are only corrected for the glass-contribution but not for the Bose-Einstein distribution and vertically shifted for clarity. The intensity and the position of the continuum photoluminescence maximum (dotted lines) are different for all compounds. Especially PST-Ba shows very strong luminescence background with maximum very close to the incident photon energy.38

Fig. 14: Maxima of the continuum photoluminescence background for PST and PSN as well as their related doped compounds. For nearly all compounds there is a clear energy down shift with respect to the incident laser energy. Only PST-Ba shows a photoluminescence maximum that is very close to the excitation wavelength of 325 nm. For all samples the error is below 0.002 eV.39

Fig. 15: Parallel and cross polarized RRS spectra of PSN related compounds. Spectra are only corrected for glass-contribution but not for the Bose-Einstein distribution and vertically shifted for clarity. The intensity and the position of the continuum photoluminescence maximum (dotted lines) are different for all compounds.....	40
Fig. 16: The wavenumber-ratio of 2 nd (II) and corresponding 1 st (I) order RRS. The upper part shows the ratio of antisymmetric bending (AB) + antisymmetric stretching (AS) vs. the combinational mode (ABAS). In the middle antisymmetric bending and its overtone are plotted. The lower part shows the antisymmetric stretching and its overtone. For all compounds and vibrational modes, the ratio is nearly equal to unity.	41
Fig. 17: Parallel and cross-polarized spectra of PST-related compounds at ambient conditions. The spectra have been corrected for the contribution of photoluminescence and are vertically shifted for clarity.....	42
Fig. 18: Total scattering intensity of the RRS spectra of all measured samples at ambient conditions in counts per second (cps) upon scattering geometry Z(XX)Z	43
Fig. 19: Parallel and cross-polarized spectra of PSN-related compounds at ambient conditions. The spectra have been corrected for the contribution of photoluminescence.....	45
Fig. 20: Total fraction of 2 nd -order resonance Raman scattering as a function of A-site doping content at ambient conditions. A-site substitution for Pb strongly affects the ratio of 1 st - and 2 nd -order RRS.....	46
Fig. 21: Integrated intensity ratio of 2 nd - and corresponding 1 st -order RRS of different spectral features. The upper plot shows the ratio between antisymmetric stretching (I AS) and its overtone (II AS), in the middle antisymmetric bending (I AB) and its overtone (II AB) are concerned while at the bottom both fundamentals (I AB & I AS) and the combinational mode (II ABAS) are presented. The normalized intensity of the fundamental modes has been squared in order to follow the cross sectional dependence for two-phonon scattering.	47
Fig. 22: Intensity of internal BO ₆ vibrations for all measured samples normalized to the total intensity of 1 st -order RRS. The upper plot shows antisymmetric BO ₆ bending, the middle antisymmetric BO ₆ stretching and in the bottom plot symmetric BO ₆ stretching is concerned.....	50
Fig. 23: Intensity of the single internal BO ₆ vibrations with respect to the total scattering intensity from of all internal BO ₆ vibrations. Especially for the fraction of antisymmetric bending in the upper plot it can be seen, that the Ba doped compounds behave differently compared with the other samples.....	52

Fig. 24: Parallel polarized spectra of three different compounds with varying amount of Ta⁵⁺ and Nb⁵⁺ on the B-site and their corresponding materials doped with Ba²⁺ on the A-site at ambient conditions. The content of Ba increases from bottom to top. The spectra are normalized to unity for better comparability.53

Fig. 25: Parallel and cross polarized RRS of PST-Ba as a function of temperature. Similar to pure PST no signals are detected at 800 K. Unlike pure PST, PST-Ba shows well pronounced RRS already well above T*54

Fig. 26: Normalized intensity as a function of temperature for all three phonon modes with involved Pb-vibrations. The lines represent fits to data points by Boltzmann functions. The inflection points for all three modes are around 340 K. The trend of all three modes represents the evolution of fraction and size of PNR in PST-Ba with decreasing temperature.55

Fig. 27: Parallel polarized spectra of PST, PSN and their corresponding materials doped with La³⁺ or Sr²⁺ on the A site at ambient conditions, respectively. The amount of doping on the A-site increases from bottom to top. The spectra are normalized to unity for better comparability.....57

Fig. 28: Parallel and cross polarized resonance Raman spectra of PSN-La for different temperatures. At T* considerable scattering signals appear, while 2nd-order RRS is nearly completely suppressed even at very low temperatures.58

Fig. 29: Parallel and cross polarized resonance Raman spectra of PSN-Sr for different temperatures. In general 2nd-order RRS is nearly entirely suppressed, whereas especially a considerable intensity of the symmetrical stretching overtone can be observed. The overall scattering intensity remains minor even for low temperatures.59

List of Tables

Table 1: Irreducible representations of optical phonon modes in Pb-based perovskite-type relaxors with Pm3m symmetry, along with their Raman/IR-activity, approximate wavenumbers and the type of atomic vibrations after (Welsch, et al., 2011). For completeness: the irreducible representation of the acoustic mode is T_{1u}	16
Table 2: Irreducible representations of optical phonon modes in Pb-based perovskite-type relaxors with Fm3m symmetry, along with their Raman/IR-activity, approximate wavenumbers and the type of atomic vibrations after (Welsch, et al., 2011). For completeness: the irreducible representation of the acoustic mode is T_{1u}	18
Table 3: List of chemical compositions, abbreviations and tolerance factors of the samples studied in this thesis.....	19
Table 4: Peak positions of 1 st -order RRS generated by antisymmetric BO ₆ bending (AB) and antisymmetric BO ₆ stretching (AS) as well as the corresponding 2 nd -order RRS by 2AB, AB+AS and 2AS for PST and PSN at ambient conditions in cm ⁻¹ . Good accordance of the wavenumber for 1 st - and 2 nd -order RRS confirms the origin of the observed spectral features.....	28
Table 5: Group-subgroup relation between the irreducible representations of the cubic aristotype perovskite structure and the rhombohedral polar as well as the antiferrodistortive structural deviations, respectively. Irreducible representations that are Raman-active under non-resonance conditions are marked red. Representations put in large brackets are complex conjugated but only one peak would be detected due to them. The relations have been calculated by using the tool “CORRELATIONS POINTS” of the Bilbao Crystallographic Server (Aroyo, et al., 2006 a; Aroyo, et al., 2006 b; Aroyo, et al., 2011).	31

List of Abbreviations

FBZ	First Brillouin zone
LPE	Lone-pair electrons
PNR	Polar nanoregions
PSN	$\text{PbSc}_{0.5}\text{Nb}_{0.5}\text{O}_3$
PSN-Ba	$\text{Pb}_{0.93}\text{Ba}_{0.07}\text{Sc}_{0.5}\text{Nb}_{0.5}\text{O}_3$
PSN-Bi	$\text{Pb}_{0.96}\text{Bi}_{0.02}\square_{0.02}\text{Sc}_{0.51}\text{Nb}_{0.49}\text{O}_{3-0.06}$
PSN-La	$\text{Pb}_{0.70}\text{La}_{0.23}\square_{0.07}\text{Sc}_{0.62}\text{Nb}_{0.38}\text{O}_{3-0.075}$
PSN-Sr	$\text{Pb}_{0.66}\text{Sr}_{0.34}\text{Sc}_{0.5}\text{Nb}_{0.5}\text{O}_3$
PST	$\text{PbSc}_{0.5}\text{Ta}_{0.5}\text{O}_3$
PST-Ba	$\text{Pb}_{0.78}\text{Ba}_{0.22}\text{Sc}_{0.5}\text{Ta}_{0.5}\text{O}_3$
PST-La	$\text{Pb}_{0.86}\text{La}_{0.08}\square_{0.06}\text{Sc}_{0.53}\text{Ta}_{0.47}\text{O}_{3-0.075}$
PSTN	$\text{PbSc}_{0.5}\text{Ta}_{0.36}\text{Nb}_{0.14}\text{O}_3$
PSTN-Ba	$\text{Pb}_{0.88}\text{Ba}_{0.12}\text{Sc}_{0.5}\text{Ta}_{0.38}\text{Nb}_{0.12}\text{O}_3$
PSTS	$\text{PbSc}_{0.40}\text{Ta}_{0.38}\text{Sn}_{0.22}\text{O}_3$
RRS	Resonance Raman scattering
T_B	Burns temperature
T^*	Intermediate temperature
T_c	Curie temperature
T_f	Freezing temperature
T_m	Temperature of the dielectric permittivity maximum

Acknowledgements

Patience and support by everyone involved were the ingredients to do this thesis. Thanks to my family, my partner in life and especially my supervisor Boriana Mihailova.

“Mentoring is a brain to pick, an ear to listen, and a push in the right direction.”

- John C. Crosby, American politician from the U.S. state of Massachusetts

1 Introduction

Relaxor ferroelectrics have attracted much attention since decades as they possess interesting and useful properties. This includes for example high dielectric response over a wide temperature range, as well as high electro-optic, electro-elastic, piezo- and pyroelectric coefficients. Therefore, they are applicable for a variety of purposes such as ferroelectric memories, small-size actuators (Granzow, et al., 2004), ultrasonic sensors and capacitors (Yamashita, et al., 1998) etc. It is well established that the properties of relaxor ferroelectrics arise from their complex nanoscale structure due to the existence of coherent structural polar distortions called polar nanoregions (PNR). Those PNR are spatial regions of coupled atomic displacements from the atomic positions in the aristotype structure, embedded in a pseudo-cubic non-polar matrix consisting of uncoupled atomic displacements. The size of PNR is insufficient to form ferroic order on the length scale detectible by X-ray or neutron diffraction. Although there have been extensive structural studies in the past, there is still an ongoing discussion about the origin of the relaxor state and how chemical variation influences the size and formation of PNR (Bokov & Ye, 2006). PNR have directly been observed by high resolution transmission electron microscopy (Bursill, et al., 1995) and are responsible for the diffuse X-ray scattering (Paściak, et al., 2007), diffuse neutron scattering (La-Orauttapong, et al., 2001) as well as for the anomalous Raman scattering in the paraelectric phase (Mihailova, et al., 2002). Furthermore, PNR in relaxors have been for example studied by applying Brillouin spectroscopy (Kim, et al., 2012) and neutron pair distribution function analysis (Jeong, et al., 2005).

Ferroelectricity is the property of certain materials to show a spontaneous net polarization that can be switched between at least two different states by applying an external electric field. Materials showing this phenomenon are called ferroelectrics. By cooling down from high temperatures, typically these materials show a paraelectric-to-ferroelectric phase transition at the so-called Curie temperature T_c , where domains with long-range ferroelectric order develop in symmetry allowed orientations. Ferroelectric domains carry electrical polarization P and thus generate an electric field. Upon an external electric field E the spontaneously formed domains realign giving rise to a hysteresis loop (Fig. 1). The domains

are forced to align their orientation to the direction of the external electric field. When all domains are aligned in the same direction, a saturation of the net polarization is established. By removing the external electric field the domains behave inertially and a net polarization remains (P_r). Only by applying a coercive electric field (E_c) with reverse orientation and magnitude the total net polarization becomes zero again.

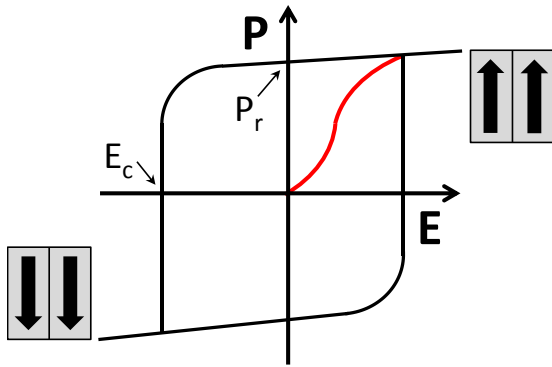


Fig. 1: Hysteresis loop of the net polarization (P) as a function of external electric field (E). After all ferroelectric domains are aligned in the same direction (arrows) a saturation of the polarization is reached. By removing the external electric field, a remanent polarization (P_r) still exists. The net polarization can be suppressed to zero by applying a coercive electric field (E_c).

The establishment of polar properties depends on the crystal symmetry. Structural polarity is allowed only in the absence of a center of inversion and in the presence of a polar axis (axis of symmetry with no mirror plane perpendicular to it). The former is fulfilled for 20 point groups (piezoelectric crystal classes), while the latter only for 10 point groups (polar crystal classes). Hence, the para-to-ferroelectric phase transition should be accompanied by a change of the crystal point symmetry. A characteristic property of ferroelectrics is to show a sharp maximum of the dielectric

permittivity at the phase transition temperature T_c . Relaxor ferroelectrics in this context show a broad, strong frequency-dependent maximum of the dielectric permittivity $\epsilon(T)$ due to their nanoscale structural arrangement, and the maximum of $\epsilon(T)$ is often in the vicinity of room temperature. The dielectric permittivity describes the resistivity that is encountered by a dielectric material when an electric field is formed within it. The name of relaxors stems from their distinctive different dielectric relaxation behavior compared to classical ferroelectrics. The vast majority of relaxors has perovskite-type structure (ABO_3) where the A site usually is occupied by Pb^{2+} while the B site accommodates at least two chemical elements. There are also other structure types bearing materials with relaxor behavior e.g. the tungsten bronze (Stephanovich, 2010) and pyrochlore structure (Du, et al., 2008).

The perovskite-type structure (Fig. 2) allows the incorporation of various cations on the A and B site, where the range of ionic radii is limited by a relation called the tolerance factor, introduced by V. M. Goldschmidt in 1926.

$$t = \frac{r_A + r_0}{\sqrt{2} (r_B + r_0)} \quad \text{Eq. 1}$$

Eq. 1 gives the tolerance factor, where r_A and r_B represent the ionic radius of the A- and B-site cation respectively, r_0 is the ionic radius of the anion, which is oxygen in most of the

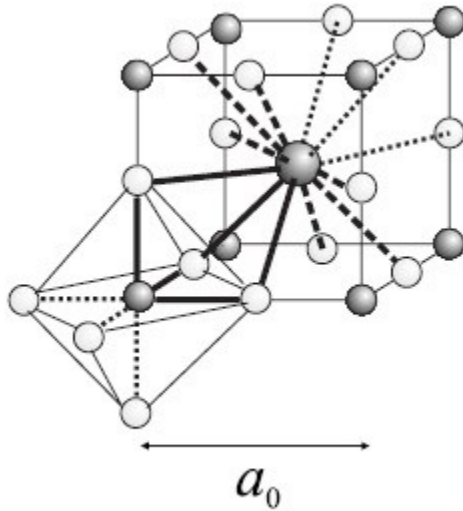


Fig. 2: The aristotype perovskite structure with symmetry $Pm\bar{3}m$ and unit cell parameter a_0 . Large grey sphere at the center of the cube represents the A-site cation. Small, grey spheres at the corners of the cube are B-site cations and white spheres are anions i.e. oxygen atoms. By doubling the structure (8 primitive cubic unit cells in total with unit cell length $2 \times a_0$) changes the symmetry to $Fm\bar{3}m$ (Mihailova, et al., 2008 a).

cases. Perovskite-type relaxors are A-site and/or B-site complex. The A site is typically occupied by Pb^{2+} , Ba^{2+} , Na^+ , K^+ , Sr^{2+} , La^{3+} and/or Bi^{3+} . The B site should be occupied by a d-element as Ta^{5+} , Nb^{5+} , Ti^{4+} in combination with Mg^{2+} , Zn^{2+} , Sc^{3+} , In^{3+} , Fe^{3+} and/or Zr^{4+} . Due to the occupation of the same crystallographic site by at least two ions of difference valence and/or different ionic radius, electric and/or elastic fields are chemically induced to the structure. These electric and elastic fields are assumed to be the basis for relaxor properties. For a long time, the common opinion was that the imbalance of charge and ionic radii is the reason for dynamic nanosize polar structural species called polar nanoregions (PNR) to

appear. These PNR are embedded in a non-polar, cubic matrix. At temperatures hundreds of Kelvin above the maximum of the dielectric permittivity (T_m), only uncoupled polar shifts exist. By cooling down, at the so-called Burns temperature (T_B), these uncoupled polar shifts merge to nucleate PNR (Burns & Scott, 1973). In this ergodic state (accessible microstates are equiprobable over a long period of time), PNR flip dynamically along symmetry-allowed orientations. At further cooling, once the characteristic temperature T^* is reached, the dynamic of present PNR slows down and they merge to form larger polar clusters. T^* clearly can be identified e.g. via acoustic emission (Dul'kin, et al., 2010). In the regime down to room temperature the lifetime of individual polar clusters approx. is 10^{-4} to 10^{-5} s (Blink, et al., 2000) according to nuclear magnetic resonance (NMR) spectroscopy. Finally by passing

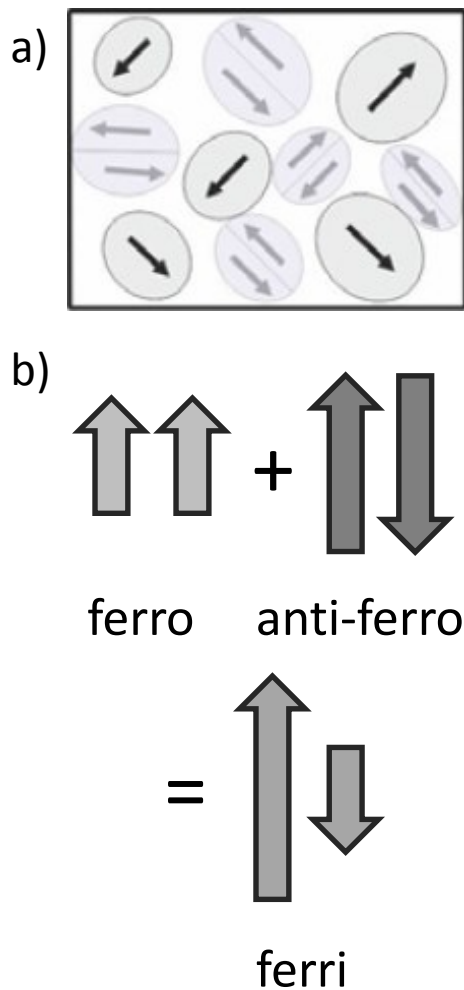


Fig. 3: a) Sketch of the structural state of Pb-based relaxors at ambient conditions. Competitive polar and antiferrodistortive ferroic order simultaneously exists on a mesoscopic scale, while the average, long-range order shows cubic symmetry (Waesermann, et al., 2013). b) Ferro- plus antiferroelectric order results in a ferrielectric state.

T_m , for lower temperatures there are different possibilities for structural evolution. Some relaxors undergo a para-to-ferroelectric phase transition with the development of long-range ferroelectric order. Others, the so-called canonical relaxors do not show any ferroelectric long-range order down to 4 K but PNR eventually become static at the freezing temperature (T_f) leading to a non-ergodic state (Bokov & Ye, 2006).

Studies during the last years promoted the perception, that perovskite-type relaxors with a complex occupied A- and/or B-site possess an average cubic structure with two additional competitive mesoscopic ferroic orders which have a *polar* and *antiferrodistortive* character, respectively (Waesermann, et al., 2011). Due to the coexistence of these two types of ferroic order in Pb-based relaxors (Fig. 3a), the structural state of these materials can be described as frustrated *ferrielectric* (Fig. 3b) (Mihailova, et al., 2015).

2 Objectives

The scope of this thesis is to study perovskite-type relaxor ferroelectrics with various A- and B-site doping by resonance Raman scattering (RRS). For this purpose stoichiometric $\text{PbSc}_{0.5}\text{Ta}_{0.5}\text{O}_3$ (PST) and $\text{PbSc}_{0.5}\text{Nb}_{0.5}\text{O}_3$ (PSN), A-site doped PST and PSN with Ba^{2+} , Sr^{2+} , La^{3+} , Bi^{3+} as well as B-site doped PST with Nb^{5+} and Sn^{4+} were considered. The basic motivation at this is to improve the understanding of the relationship between relaxor properties and their complex nanoscale structure. The first aim was to establish whether RRS has the potential to selectively enhance the Raman scattering arising from PNR while suppressing scattering from non-polar cubic structural species. In this context the polarity of single atomic vibrational modes could be clarified and furthermore, how the temperature evolution of ferroic structural species takes place. Second, RRS spectra of different doped compounds at ambient conditions were compared in order to determine the influence of atomic substitution on the size, fraction and coherence of polar structural species as well as on the electron-phonon coupling. Third, the distinctive difference of an increased and decreased tolerance factor due to doping compared with pure compounds was estimated by considering RRS spectra of materials with A-site dopants having larger or smaller ionic radii than Pb^{2+} as a function of temperature. The evaluation of the measured spectra is supported by RRS selection rules derived from group theory analysis. Moreover, pressure-dependent Raman spectroscopy under resonance conditions was applied to characterize the competitive behavior of polar and antiferrodistortive ferroic order.

A deeper understanding of the connection between the complex nanoscale structure influenced by a varying chemistry and the remarkable properties of perovskite-type relaxor ferroelectrics may allow developing new useful ferroic materials in the future.

3 Methods and theoretical basis

The data underlying this thesis were all conducted using resonant and non-resonant Raman spectroscopy. The following sections should give an overview of the methodological issues as well as of the fundamental theory of crystal lattice dynamics and the relevant scattering processes.

3.1 Electromagnetic radiation

In order to understand the used experimental methods, it is necessary to characterize the properties of the utilized information carrier. In general the electromagnetic radiation is described as a wave of oscillating electric and magnetic field perpendicular to each other while the direction of propagation is perpendicular to both fields (transversal). The connection between the frequency of oscillation (f) and the wavelength (λ) is given by

$$\lambda = \frac{c}{f} \tag{Eq. 2}$$

where c is the speed of light in vacuum. The quantum of an electromagnetic wave is represented by an elementary particle called photon, while the energy of a photon is given by

$$E_{\text{photon}} = hf = \hbar\omega \tag{Eq. 3}$$

where h is the Planck constant, \hbar is the reduced Planck constant ($= h/2\pi$) and ω ($= 2\pi f$) is the angular frequency. Photons interact with matter in terms of transmission, absorption or scattering. Depending on their energy, photons can induce electron transitions or interact with atomic vibrations and thus provide information about structure and chemical bonding.

Raman spectroscopy is based on the scattering of photons by atomic vibrations i.e. lattice vibrations or phonons in crystals. The energy of these photons typically is in the near-infrared (1400 to 780 nm), visible (780 to 380 nm) or UV spectral range (380 to 240 nm).

3.2 Lattice dynamics of crystals

Even though Raman spectroscopy is also used to study molecules of gases and fluids, since the thesis is focused on crystalline compounds, this paragraph only deals with the consideration of atomic dynamics of solids, more precisely crystals.

All vibrations in a crystal lattice can be described by the superposition of its normal vibrational modes, which correspond to the irreducible representations in terms of the crystal symmetry. Each atom in a crystal has 3 degrees of freedom, one along each direction of space. The number of normal vibrational modes in a crystal is given by $3 \times N$, with N atoms

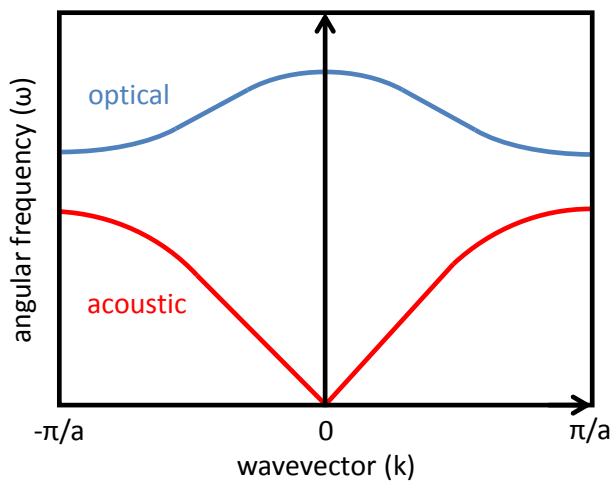


Fig. 4: Dispersion relation of a one-dimensional, diatomic chain with the phonon angular frequency (ω) as a function of the phonon wavevector (k). The point at $k = 0$ corresponds to the center of the FBZ whereas π/a and $-\pi/a$ represent the boundary of the FBZ with “ a ” being the unit cell parameter. Acoustic phonons (red) show strong dispersion and $\omega(k)$ becomes zero at the FBZ center. Optical phonons (blue) have non-zero frequency for any wavevector throughout the FBZ.

in the primitive unit cell. The energy of lattice vibrations is quantized, just like the energy of an electromagnetic wave, and the quantum of lattice vibration is represented by quasiparticles called phonons. The phonon density of states is the complete set of phonon branches within the first Brillouin zone (FBZ). The FBZ is the Wigner-Seitz cell of the reciprocal space, where the Wigner-Seitz cell is one type of primitive unit cell confined by planes, bisecting the distance between one lattice point and all its direct neighboring lattice points. The phonon branches describe the dispersion throughout the FBZ i.e. the angular frequency as a function of the wavevector (k). In general three phonon modes are acoustic (A), meaning the participating atoms move in phase and behave as sound waves. Basically, those modes define the velocity of sound in crystals. If the atomic basis consists of at least two atoms, $3N - 3$ phonon modes are optic (O). For optical phonons atoms move out of phase which induces a dipole moment due to the off-shifting of the center of gravity of negative charge carriers with respect to that of positive charge carriers. This dipole moment is capable to interact with the electric field of light.

The principle dispersion relation of phonons is shown in Fig. 4, using the example of a one-dimensional diatomic chain. In this case the number of phonon branches is determined by 1 (dimensions) x 2 (number of atoms the primitive unit cell) yielding 2 branches. The upper band with relatively small dispersion is the optical branch, whereas the acoustic branch below shows strong dispersion throughout the FBZ with zero-frequency at the center (Γ -point). Phonons are additionally characterized by the orientation of atomic displacement vectors to the direction of propagation. If atoms vibrate along the direction of propagation the wave-character is longitudinal (L), whereas in the case of atoms vibrating perpendicular to the wave propagation it is transversal (T). Thus, altogether there are four different combinations of dispersion relation and wave character: LO, TO, LA, TA.

$$\omega = \sqrt{\frac{K}{m}} \quad \text{Eq. 4}$$

The underlying basis of modelling lattice vibrations is the harmonic oscillator (Eq. 4) with ω the angular frequency, K the force constant and m the atomic mass, i.e. vibrations involving heavy atoms and/or weaker interatomic interactions have lower frequency. Therefore the phonon energy $E = \hbar\omega$ is mainly determined by the mass of participating atoms and by the bonding forces between these atoms.

3.3 Raman spectroscopy

Raman spectroscopy is based on the Raman effect, which was already predicted in 1923 by the Austrian physicist A. Smekal, and was first experimentally proven for crystals by G. Landsberg and L. I. Mandelstam in 1928. Some days after them C.V. Raman and K.S. Krishnan found the same effect for liquids and gases, however both groups published their results almost at the same time, the phenomenon was named Raman scattering and in 1930 Raman received the Nobel Prize for his work.

Raman scattering can be considered as inelastic scattering of electromagnetic radiation by atomic vibrations. Usually a sample is irradiated with a laser-beam of well-defined wavelength of the visible/near-visible spectrum and as a result energy shifts of the scattered from the incident photon energy are detected. Figure 5 shows different scattering processes including the corresponding energy levels of atomic vibrations. Basically, the incident photon excites the sample to an intermediate virtual state and it subsequently relaxes back to a vibrational state. In the most probable case the incident and the final vibrational state coincide and the incident as well as the scattered photon has the same energy, thus the photon is scattered elastically (Rayleigh). Since the probability for inelastic scattering is dramatically smaller than for elastic scattering only one of 10^6 to 10^8 photons is scattered inelastically (Smith & Dent, 2005, p. 73). Thus, the intensity of Raman scattering is weak compared with Rayleigh scattering. If the final vibrational state has higher energy than the incident level, the scattered photon shows lower energy than the incident photon. This is a so-called Stokes process. By contrast an anti-Stokes process involves an initial vibrational state with higher energy than the final state.

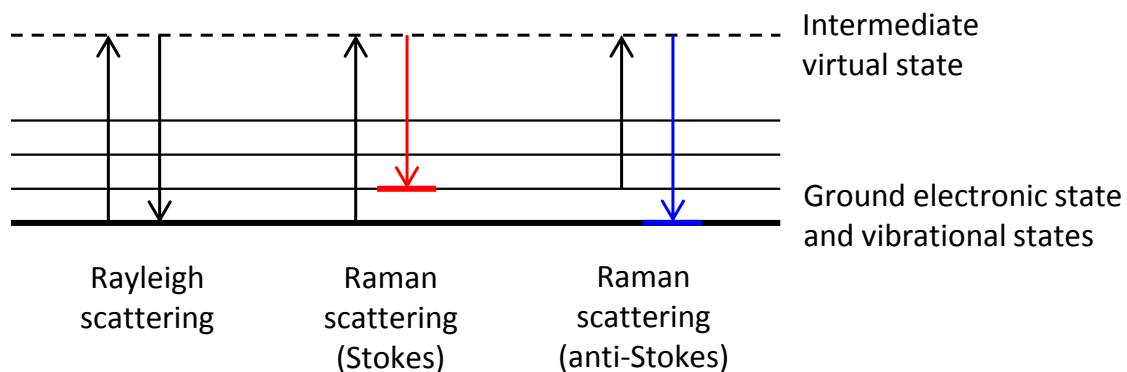


Fig. 5: Elastic (Rayleigh) and inelastic (Stokes & anti-Stokes) light scattering and corresponding transitions between vibrational states during the Raman scattering process.

Both Stokes as well as anti-Stokes are referred to as Raman shifts. For an anti-Stokes shift a higher vibrational level has already to be populated in order to increase the energy of a scattered photon. Raman spectra are typically plotted with intensity as a function of the Raman-shift wavenumber, usually given in inverse centimeters, i.e. inversely proportional to the wavelength (Eq. 5).

$$\tilde{\nu} = \frac{1}{\lambda} \quad \text{Eq. 5}$$

The ratio between the intensity of Stokes and anti-Stokes inelastic scattering is given by

$$\frac{I_{anti-Stokes}}{I_{Stokes}} = \left(\frac{\tilde{\nu}_i + \tilde{\nu}_s}{\tilde{\nu}_i - \tilde{\nu}_s} \right)^4 \exp \left(-\frac{\tilde{\nu}_s}{k_B T} \right) \quad \text{Eq. 6}$$

where $\tilde{\nu}_i$ is the wavenumber of the incident photon, $\tilde{\nu}_s$ is the wavenumber of the scattered photon, k_B is the Boltzmann constant and T is the absolute temperature. From the second term of the equation it follows, that up to temperatures where crystals can typically be studied without melting, the intensity of anti-Stokes is usually weaker than the intensity of Stokes, whereby the ratio between anti-Stokes and Stokes scattering increases with the temperature.

However, Raman scattering cannot be observed for all phonons within the FBZ. The scattering of a photon by a phonon must obey the energy and momentum conservation law. This means only phonons with wavevector $q \approx 0$ from the center of the FBZ at the Γ point can be observed, since the magnitude of the incident radiations wavevector has typical order of 10^3 to 10^6 cm^{-1} (infrared to ultra-violet).

Phonons can be Raman-active, IR-active or silent. In order to be Raman-active the atom movement of a vibrational mode must induce a change of the bond-polarizability which is given by

$$P_i = \alpha_{ij} E_j \quad \text{Eq. 7}$$

where P is the polarization induced by an electric field E and α is the polarizability tensor. In the case of Raman scattering, the polarizability is the tendency of the electron cloud around atomic bonds to be distorted by the electric field of light. Whether a phonon is Raman-active can be calculated by applying group theory analysis, which will be treated later on.

Raman spectroscopy offers some advantages in structural analysis. The time resolution is high due to the short lifetime of excited virtual states in a Raman scattering process (ca. 10^{-14} s)¹ and corresponds to the period of atomic vibrations which is usually about 10^{-13} s (Quinn & Yi, 2009, p. 45). Furthermore, the Raman scattering event in semiconductors and insulators occurs within the range of a few unit cells. In combination, this allows detection of signals from local, small-scale structural states which at the same time may show strong dynamics, just like PNR in relaxor ferroelectrics.

The intensity of Raman scattering depends on a variety of parameters. As can be seen in Eq. 7, Raman scattering on the one hand depends on the direction, since the polarizability is expressed via a 2nd-rank tensor. On the other hand, the population of vibrational states depends on temperature. Since phonons are bosons (have integer spin), this population follows the Bose-Einstein distribution. The occupation factor “n” for a vibrational state “s” with wavenumber $\tilde{\nu}$ therefore is given by Eq. 8.

$$n_s(\tilde{\nu}) = \frac{1}{\exp\left(\frac{\tilde{\nu}}{k_B T}\right) - 1} \quad \text{Eq. 8}$$

In order to compare spectra measured at different temperatures, it is necessary to correct for this dependence. Additionally, the overall intensity increases with the 4th power of incident photon energy (Kuzmany, 2009, p. 191).

3.4 Resonance Raman spectroscopy

Resonance Raman scattering (RRS) occurs, if the wavelength and thus the energy of the incident radiation is close to or coincident with an allowed electric dipole transition. Under such conditions the incident photon excites also the corresponding electron, along with phonons. Hence, fundamental RRS is a process of three-particle interaction: photon, phonon and electron. Consequently, the scattering intensity can be enhanced by a factor of 10^3 to

¹ (Ferraro & Nakamoto, 1994, p. 17)

10^4 (Smith & Dent, 2005, p. 93). This makes resonance Raman spectroscopy a technique very sensitive even for a small sample size. Besides, by utilizing RRS the selection rules change compared to the non-resonance case, because the activated electron transition has to be taken into account. For example, this can be the way to observe phonon modes which are symmetry forbidden under non-resonance conditions. Figure 6 expands the Raman scattering process shown in Fig. 5 by the process of RRS with involved electronic and vibrational energy levels. The striking difference compared to the non-resonant case is the fact that the excited electron energy level corresponding to the incident photon energy i.e. the intermediate state is not a virtual state but an eigenstate of the sample.

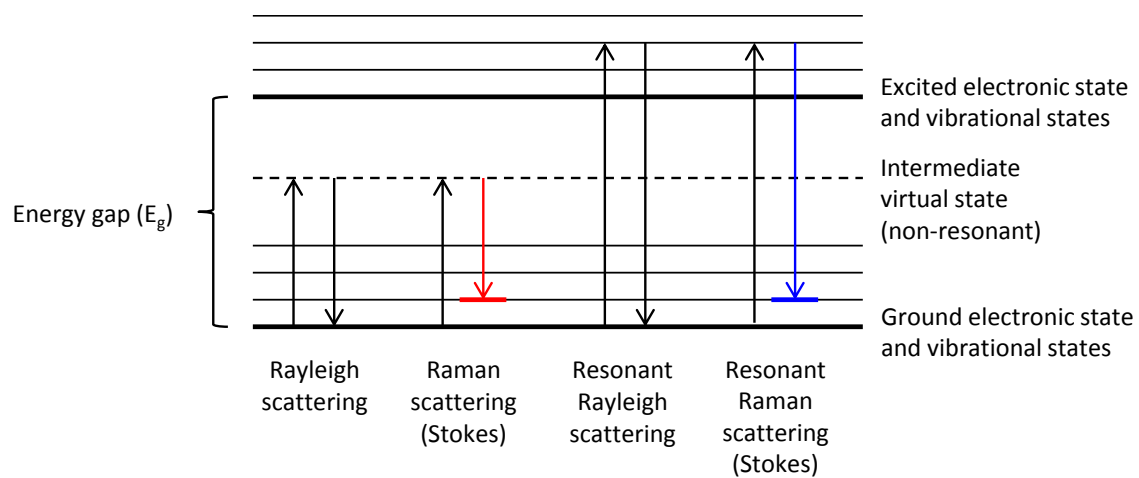


Fig. 6: Elastic (Rayleigh) and inelastic (Stokes) light scattering and corresponding transitions between vibrational states under resonance and under non-resonance conditions. In the case of RRS the intermediate state is an eigenstate and not a virtual state.

That means that the incident photon excites the electron in accordance with symmetry-allowed electron transitions. Thus, during a RRS process not only the vibrational but also the electronic energy state changes. In consequence of the fact that a transition to an eigenstate occurs, the lifetime of the intermediate excited state is strongly increased and this promotes the probability of phonon creation (Kuzmany, 2009, p. 205).

The underlying phenomenon is Heisenberg's uncertainty principle that limits the precision with which two complementary particle properties can be determined. One of those pairs is time (t) together with energy (E) (Eq. 9).

$$\Delta t \Delta E \leq \frac{\hbar}{2} \quad \text{Eq. 9}$$

The energy conservation law is less violated by an intermediate state which is an eigenstate of the system, thus the excitation is more stable.

Basically, RRS depends on the electron-phonon interaction i.e. the strength of electron-phonon coupling for a certain material or more precisely the coupling of specific phonons to the excited electrons. Optical phonons can be considered as instantaneous structural distortions and there are at least two different mechanisms of electron-phonon interaction related with insulators and also semiconductors concerning optical phonons. On the one hand, enhancement of Raman scattering signals from optical phonon modes due to resonance can be achieved by the so-called *deformation-potential* interaction between electrons and optical phonons. This term considers the capability of optical phonons to influence the electronic band structure i.e. electron energy levels due to a change of bond angles and bond lengths during corresponding atomic vibrations (Cardona & Yu, 2005, p. 132). This type of RRS involves both LO and TO phonons. On the other hand the RRS process can also be dominated by the so-called *Fröhlich interaction*. It is based on electrostatic interaction between electrons and the electric field that is generated by longitudinal optical (LO) phonons that carry polarity, i.e. which involve displacements of oppositely charged ions (Cardona & Yu, 2005, p. 134).

In 1st-order RRS (one photon interacting with one phonon) usually phonons near the center of the FBZ interact with the electron excited due to the incident photon energy, since the majority of related electron transitions will be direct processes i.e. vertical. An electron transition is called direct if the highest energy state of the valence band and the lowest energy state of the conduction band share the same momentum at the center of the FBZ. However, indirect processes can also be realized by additional momentum due to a phonon.

Acoustic phonons can also become Raman-active under resonance conditions e.g. due to the piezoelectric effect. In piezoelectric materials (no center of inversion) the strain accompanied by acoustic phonons is able to induce an electric field which in turns interacts with the electric field of electrons (Cardona & Yu, 2005, p. 131).

3.5 Multi-phonon Raman scattering

In principle, photons are also capable to interact with more than one phonon during a single Raman scattering event. This phenomenon commonly is called multi-phonon or higher-order scattering while one-phonon scattering is denoted as *fundamental* or 1st-order. The most probable multi-phonon scattering implies the participation of two phonons and it is called 2nd-order Raman scattering. For insulators, under non-resonant conditions, multi-phonon scattering is usually expected to show very weak intensities i.e. it can hardly be observed. Under resonance conditions, however, multi-phonon Raman scattering often can be triggered and is significantly enhanced.

Whereas fundamental Raman scattering is restricted to phonons at the Γ point (FBZ center) due to the already mentioned energy and momentum conservation, multi-phonon Raman scattering can involve also contribution from non-center phonons, if the vector sum of phonon momenta is zero. Thus, 2nd-order Raman scattering basically reflects the corresponding phonon dispersion, depending on whether there are distinctive varying frequencies for other points of the FBZ with respect to the Γ point.

Two types of multi-phonon scattering can be distinguished. Interactions between phonon modes with identical mechanical representation and the same energy are called *overtones*. Interplays between phonon modes having different mechanical representations and/or different energies are called *combinations* or *difference modes*, depending on whether the resulting frequency corresponds either to the sum or to the difference of the involved fundamentals. Multi-phonon Raman scattering can be realized in two ways: (i) by a single multi-phonon scattering event or (ii) due to rescattering of individual phonons at the Γ point (Sherwood, 1972, p. 141f.). In the course of these both processes, the latter is most often negligible due to low probability of the event. The former should involve phonon-phonon coupling given by the anharmonic term in the crystal potential.

The relationship between the wavenumber of fundamental and the corresponding multi-phonon scattering is approximately given by the absolute sum i.e. difference of involved fundamental phonon modes. This implies e.g. for 2nd-order overtone scattering that $\tilde{\nu}_{overt.} = \tilde{\nu}_{fund.} * 2$. Nevertheless, due to the anharmonic character of phonon-

phonon interaction regarding the crystal potential i.e. the binding energy of the corresponding phonons usually $\tilde{\nu}_{overt.}$ will be slightly shifted to lower wavenumbers.

The temperature dependence of multi-phonon Raman scattering is dominated by the increase in the thermal phonon population by increasing temperature just as fundamental Raman scattering. Thus, the intensity of multi-phonon Raman scattering is promoted at high temperatures. However, the influence of thermally populated vibrational states on two-phonon scattering is stronger than compared to 1st-order Raman scattering. This is due to the fact that the intensity of fundamentals is enhanced by $[n(\tilde{\nu}) + 1]$ (cf. Eq. 8) while 2nd-order scattering intensity is increased by $[n(\tilde{\nu}) + 1]^2$ (Sherwood, 1972, p. 150). Since $n(\tilde{\nu})$ is an exponential function, its slope becomes higher by squaring. Thus thermal coefficients of Raman scattering intensity with significant values appear also for higher wavenumbers compared to fundamental Raman scattering.

3.6 Group theory analysis and Raman selection rules

Group theory is a mathematical discipline, which deals with the symmetrical aspects of algebraic structures. In terms of physics, it is a useful tool to describe the connection between structure and properties of a crystal. Group theory analysis can be performed to determine selection rules for electron as well as phonon transitions. In this sense group-

Table 1: Irreducible representations of optical phonon modes in Pb-based perovskite-type relaxors with $Pm\bar{3}m$ symmetry, along with their Raman/IR-activity, approximate wavenumbers and the type of atomic vibrations after (Welsch, et al., 2011). For completeness: the irreducible representation of the acoustic mode is T_{1u} .

Irreducible representation	Optical activity	Approx. wavenumber	Vibrations
T_{2u}	-	300, 350 cm^{-1}	Pb-O bond stretching within the {111} plane can be considered as BO_6 tilting
T_{1u}	IR	140 cm^{-1}	Pb- BO_3 translation
T_{1u}	IR	430 cm^{-1}	anti-symmetric BO_6 bending vibrations
T_{1u}	IR	700 cm^{-1}	anti-symmetric BO_6 stretching vibrations

theory analysis is applied to predict which normal phonon modes of a point group are Raman-active under different conditions (non-resonance, resonance, 1st-order, 2nd-order

etc.). In the context of group theory, crystal normal modes are irreducible representations of the crystal dynamics (Jacobs, 2005, p. 81).

Irreducible representations can be expressed via different notations. One way is to use the Miller-Love notation, which is often used in inelastic neutron scattering experiments and model calculations, when the wavenumber dispersions are studied. (Miller & Love, 1967). The main character denotes the corresponding point of the FBZ (e.g. Γ for the center) while the subscript number ascendingly labels the irreducible representations starting with $i = 1$ from the highest to the lowest symmetry (Γ_i). The preferred style in connection with this thesis to express the irreducible representations of specific space groups is the Mulliken notation after the US physicist Robert Sanderson Mulliken. In this notation, "A" and "B" represent the non-degenerate states which are symmetric or antisymmetric with respect to rotations about the principal axis, respectively, whereas "E" and "T" denote the doubly and triply degenerate states. The subscripts "g" (German: gerade) and "u" (German: ungerade) label representations that are symmetric or antisymmetric with respect to the center of inversion. In the same manner, "1" and "2", respectively the superscripts (') and (''), indicate whether a representation is symmetric or antisymmetric to a mirror plane either vertical or perpendicular to the principal axis of rotation. The degeneracy of an irreducible representation is equivalent to the superposition of energetically indiscernible, symmetrically related normal vibrational modes.

For a single perovskite cubic structure ($Pm\bar{3}m$) which is associated with chemically B-site disordered relaxors studied here, there are no phonon modes that are Raman-active under non-resonance conditions (Table 1). As mentioned in the introduction, despite of chemical disorder, on a local scale chemical B-site order dominates in perovskite-type $PbB'B''O_3$ relaxors, thus the Raman spectra of perovskite-type relaxor ferroelectrics with a complex occupied crystallographic B-site must be interpreted by considering a doubled perovskite structure ($Fm\bar{3}m$). The irreducible representations of phonon modes for this space group and their Raman-activity are given in Table 2.

Table 2: Irreducible representations of optical phonon modes in Pb-based perovskite-type relaxors with $Fm\bar{3}m$ symmetry, along with their Raman/IR-activity, approximate wavenumbers and the type of atomic vibrations after (Welsch, et al., 2011). For completeness: the irreducible representation of the acoustic mode is T_{1u} .

Irreducible representation	Optical activity	Approx. wavenumber	Vibrations
A_{1g}	Raman	820 cm^{-1}	symmetric BO_6 stretching
E_g	Raman	800 cm^{-1}	symmetric B-O stretching
T_{2u}	-	$300, 350\text{ cm}^{-1}$	Pb-O bond stretching within the $\{111\}$ plane can be considered as BO_6 tilting
T_{2g}	Raman	50 cm^{-1}	Pb vibrations
T_{2g}	Raman	550 cm^{-1}	O-B-O symmetrical bending vibrations
T_{1u}	IR	140 cm^{-1}	Pb- BO_3 translation
T_{1u}	IR	240 cm^{-1}	B-site cation vibrations
T_{1u}	IR	430 cm^{-1}	anti-symmetric BO_6 bending vibrations
T_{1u}	IR	700 cm^{-1}	anti-symmetric BO_6 stretching vibrations
T_{1g}	-	230 cm^{-1}	BO_3 rotations

According to Table 2 four phonon modes are expected to be observed in Raman experiments under non-resonance conditions for the cubic matrix: $A_{1g} + E_g + 2T_{2g}$. The T_{1u} modes are IR-active and thus carry polarity. It is basically possible that phonon modes are simultaneously Raman and IR-active but for centrosymmetric structures there is a mutual exclusion rule for this to occur. The A_{1g} mode embodies the so-called totally symmetric representation of the corresponding space group $Fm\bar{3}m$. This is important for the later discussion of the selection rules for resonance Raman scattering.

4 Samples and experimental conditions

4.1 Samples

All measured samples are relaxor ferroelectric single crystals that are based on the two model compounds PST and PSN. In the context of previous studies, both have been doped with different cations on the perovskite A and/or B site in order to study the consequences on their structural state i.e. their ferroic properties. All samples are listed with their chemistry, tolerance factor and abbreviation in Table 3.

Table 3: List of chemical compositions, abbreviations and tolerance factors of the samples studied in this thesis.

Sample	Chemical composition	Tolerance factor
PSN	$\text{PbSc}_{0.5}\text{Nb}_{0.5}\text{O}_3$	0.977
PSN-Ba	$\text{Pb}_{0.93}\text{Ba}_{0.07}\text{Sc}_{0.5}\text{Nb}_{0.5}\text{O}_3$	0.981
PSN-Bi	$\text{Pb}_{0.96}\text{Bi}_{0.02}\square_{0.02}\text{Sc}_{0.51}\text{Nb}_{0.49}\text{O}_{3-0.06}$	0.976
PSN-La	$\text{Pb}_{0.70}\text{La}_{0.23}\square_{0.07}\text{Sc}_{0.62}\text{Nb}_{0.38}\text{O}_{3-0.075}$	0.926 / 0.961*
PSN-Sr	$\text{Pb}_{0.66}\text{Sr}_{0.34}\text{Sc}_{0.5}\text{Nb}_{0.5}\text{O}_3$	0.971
PST	$\text{PbSc}_{0.5}\text{Ta}_{0.5}\text{O}_3$	0.977
PST-Ba	$\text{Pb}_{0.78}\text{Ba}_{0.22}\text{Sc}_{0.50}\text{Ta}_{0.50}\text{O}_3$	0.985
PST-La	$\text{Pb}_{0.86}\text{La}_{0.08}\square_{0.06}\text{Sc}_{0.53}\text{Ta}_{0.47}\text{O}_{3-0.075}$	0.941 / 0.971*
PSTN	$\text{PbSc}_{0.5}\text{Ta}_{0.36}\text{Nb}_{0.14}\text{O}_3$	0.977
PSTN-Ba	$\text{Pb}_{0.88}\text{Ba}_{0.12}\text{Sc}_{0.5}\text{Ta}_{0.38}\text{Nb}_{0.12}\text{O}_3$	0.979
PSTS	$\text{PbSc}_{0.40}\text{Ta}_{0.38}\text{Sn}_{0.22}\text{O}_3$	0.977

* tolerance factor without taking into account existing vacancies

PST and PSN have a very similar chemistry where only the second B-cation is different. Ta^{5+} and Nb^{5+} possess the same charge and the same ionic radius in octahedral coordination. Thus, the tolerance factor of both materials is equal. However, neither the mass nor the B-O bond constant for Ta and Nb is the same. Although PST and PSN are quite similar, these differences provide individual behavior and properties. At low temperatures, for PST the coupling and off-centering shifts of Pb atoms are predominantly favored, while in the case of

PSN primarily off-centered shifts of B-cations and their coupling can be observed. In addition, it is known, that the size of PNR in PST is larger than in PSN. Regardless of this, both compounds share to show a phase transition accompanied by the development of ferroelectric long-range order at lower temperatures.

4.1.1 B-site doping

In order to estimate the influence of the complex B-site occupancy on the relaxor behavior in the $AB'B''O_3$ -type relaxors, PST samples with a third type of B-site cation have been synthesized (Mihailova, et al., 2007 c). PST has been doped with Nb^{5+} for an isovalent substitution of Ta^{5+} on the ferroelectrically active B site (PSTN), whereas the incorporation of Sn^{4+} (PSTS) simultaneously substitutes for both types of B-site cations (Sc^{3+} and Ta^{5+}). In both cases the tolerance factor does not change compared to pure PST, thus only the influence of different cation mass, force constants and charge imbalance is defining the differences to stoichiometric PST. PSTN and PSTS have been probed in earlier studies by non-resonance Raman scattering and X-ray diffraction (XRD), at different temperatures as well as high pressures (Welsch, et al., 2011; Mihailova, et al., 2013).

For both PSTN and PSTS the development of long-range ferroelectric order at low temperatures is suppressed. T^* is slightly shifted to lower temperatures for PSTS, while for PSTN it shows a value similar to pure PST. For PSTN the pressure induced phase transition p_{c1} realized via octahedral tilting is up-shifted to 2.5 GPa whereas for PSTS it is down-shifted to 1.3 GPa towards 1.9 GPa for PST.

4.1.2 A-site doping

Relaxor properties can also be induced by a complex A-site occupancy of the perovskite structure ($A'A''BO_3$). One representative of this group of relaxor ferroelectrics is for example $Na_{0.5}Bi_{0.5}TiO_3$ (Saïd & Mercurio, 2001). In lead-based relaxors with mixed B-site occupation e.g. PST, properties are also strongly influenced by additional A-site substitution. PST and PSN compounds with simultaneous A- and B-site substitution have been synthesized in order to study the significance of A-site cations for relaxor properties. In this context the question

may be answered whether it is possible to completely substitute lead for different elements, by avoiding the use of lead concerning its health risk (Tong, et al., 2000). In fact, Pb^{2+} possess so-called *stereochemically active lone pair electrons* (LPE), which have proven to be crucial for the coherence of polar shift in relaxor ferroelectrics and thus cannot easily be spared (Cohen, 1992).

4.1.2.1 Bi doping

In the context of earlier studies the model compound PSN doped with Bi^{3+} ($r_{\text{ionic}} = 1.45 \text{ \AA}$ in twelvefold coordination)² has been examined by synchrotron single-crystal and high-resolution powder XRD as well as by polarized Raman spectroscopy. The objective was to determine the effect of substitution of Pb^{2+} for a cation with similar ionic radius and the same outermost electron shell (tendency to form LPE), but inducing additional electric fields due to higher charge compared to Pb^{2+} (Maier, et al., 2009). Previous studies by complementing non-resonance Raman scattering and XRD showed that doping the A-site with Bi^{3+} indeed promotes the formation of ferroelectric long-range order and leads to a structural state in which the fraction of the ferroelectric phase dominates over the persisting non-polar cubic matrix. On the other hand, the average size of ferroelectric domains detectible by XRD is smaller in PSN-Bi. Due to the fact that it bears analogy to Pb, Bi is a common ingredient for lead-free perovskite-type relaxors with a complex occupied A site which are also recently studied (Kirsever & Yılmaz, 2015).

4.1.2.2 Ba doping

The incorporation of Ba^{2+} ($r_{\text{ionic}} = 1.61 \text{ \AA}$ in twelvefold coordination)² into the model compounds PST and PSN represents a substitution of Pb^{2+} with a cation exhibiting an isotropic outermost electron shell and thus has no affinity to form LPE. In addition doping with Ba^{2+} induces local elastic fields to the structure due to a larger ionic radius with respect

² (Okawa, et al., 2002)

to Pb^{2+} . PST and PSN in earlier studies have been doped with Ba^{2+} for the purpose of considering the effect of local elastic vs. local electric fields (Marinova, et al., 2006). Several methods have been applied to PST-Ba e.g. XRD, dielectric measurements, Raman scattering, and optical absorption spectroscopy. Also high-temperature synchrotron single-crystal XRD and high-temperature Raman spectroscopy (Mihailova, et al., 2008 a) as well as temperature-dependent Raman spectroscopy under an external dc electric field (Maier, et al., 2012) has been applied to gain a further insight into the effect of Ba doping. The analysis shows that Ba doping suppresses the development of long-range ferroelectric order and drives the PST and PSN compounds to a structural state of canonical relaxors.

4.1.2.3 La and Sr doping

Twelvefold coordinated La^{3+} ($r_{\text{ionic}} = 1.36 \text{ \AA}$)³ and Sr^{2+} ($r_{\text{ionic}} = 1.44 \text{ \AA}$)³ possess a smaller ionic radius compared with Pb^{2+} ($r_{\text{ionic}} = 1.49 \text{ \AA}$)³. PST and PSN have been doped with La^{3+} to study the effect the substitution of Pb for a heterovalent cation with smaller ionic radius and no affinity to form LPE (Maier, et al., 2011 a). The comparison to Sr doped PSN was performed to distinguish between effects on the relaxor state arising from local elastic strain and/or local electric fields. Doping the A site with cations having a smaller ionic radius with respect to Pb leads to a lowering of the tolerance factor compared with the pure model compounds, which favors the development of BO_6 tilting. Furthermore, La^{3+} and Sr^{2+} both disturb the system of LPE associated with Pb, while La^{3+} induces additional electric fields due to its higher charge. It has been shown that the incorporation of La^{3+} as well as of Sr^{2+} reduces the coupling between Pb and B-cation off-centered shifts and simultaneously promotes the antiphase tilting of BO_6 octahedra at ambient conditions. Thus, due to the disturbance of the system of LPE and a lower tolerance factor, a dominance of the antiferrodistortive ferroic order is achieved, whereas the polar ferroic order becomes strongly suppressed. From this it could be deduced, that strain effects are rather important towards charge effects concerning the local structural inhomogeneity of lead-based perovskite-type relaxors. In fact, doping

³ (Shannon, 1976)

with La and Sr induces a structural state which for the pure compounds can only be achieved by high pressures (Mihailova, et al., 2011).

4.2 Experimental conditions

All Raman scattering experiments were conducted using a Horiba Jobin-Yvon T64000 triple-grating spectrometer equipped with an Olympus BX41 microscope. The two excitation wavelengths were provided by two different lasers. The first one is a Coherent Ar⁺ laser that has several available laser lines in the visible and UV range. The green line at 514.5 nm (2.41 eV) was used to perform Raman spectroscopy under non-resonance conditions. The used objective for the visible range enables magnification 50x. The second device is a Kimmon He-Cd (metal vapor) laser, also emitting in the visible and the UV range. The UV laser line at 325.0 nm (3.81 eV) was used for resonance Raman spectroscopy. The corresponding UV objectives provided magnification 40x for measurements at ambient conditions and 10x for experiments under different temperatures and pressures. The measured spectral range under non-resonant conditions involves 15 to 2000 cm⁻¹, while for resonance Raman spectra 30 to 2300 cm⁻¹. Holographic gratings of 1800 grooves/mm and 2400 grooves/mm were used in visible and UV Raman spectroscopic experiments. The samples were orientated with the cubic crystallographic axis [100] (cubic edge) or [110] (cubic face diagonal) along the polarization of the incident light. The analysis of the data was focused on $\bar{Z}(XX)Z$ and $\bar{Z}(XY)Z$ spectra, where X, Y, and Z are respectively along the three principle cubic crystallographic axes a, b and c. The scattering geometry is given by the Porto notation, named after the Brazilian physicist Sérgio Pereira da Silva Porto. In general terms the Porto notation is given by a(bc)d, where “a” and “d” represent the direction and “b” and “c” indicate the polarization of the incident and the scattered photon, respectively. The Raman spectra were conducted in backscattering geometry and studied with parallel and crossed polarization.

Temperature dependent measurements were conducted with a Linkam THMS-E600 stage by cooling down from 800 to 100 K. For collecting high-pressure Raman spectra a Boehler-Almax diamond anvil cell has been used with a 16:3:1 methanol-ethanol-water mixture as a pressure-transmitting medium. This mixture ensures hydrostatic pressure up to 9.8 GPa

(Angel, et al., 2007). The pressure was determined from the pressure-induced shift of the R1 photoluminescence line of ruby (Munro, et al., 1985).

The procedure of spectral evaluation starts with subtraction of background (if necessary) caused e.g. by the pressure medium, measured aside from the sample. After that a correction for the Bose-Einstein distribution is performed, eliminating the contribution from thermally populated excited vibrational states. Following this, the spectra are reduced by their individual acquisition time to receive intensity in counts per second (cps). Finally the spectra are fitted with pseudo-Voigt functions ($PV = q \cdot L + 1 - q \cdot G$, with L and G the Lorentzian and Gaussian profile functions and a weight coefficient q) to determine peak positions, full width at half maxima (FWHM) as well as integrated intensities.

Due to the weak signal and the necessity to use prolonged acquisition time, all spectra collected under resonance conditions with $\lambda = 325$ nm were interfered by the scattering from the glass of the deployed objective. The attendant contribution from glass could be selectively measured by using a gold wafer and was subsequently subtracted from the spectra. In this context, a gold wafer is sufficient to collect a reference spectrum due to the scattering from the optics directing the beam, because it is well crystalline and its structure ($Fm\bar{3}m$) depending on occupied Wyckoff positions shows no Raman-active phonon modes and especially because noble metals simply reflect the photons without inelastically scattering them. In addition, the resonance Raman spectra showed continuum photoluminescence background due to electron-transitions that had to be removed by applying an appropriate polynomial function, prior fitting the Raman peaks arising from phonon excitations.

5 Results and Discussion

In the following at first Raman spectra of PST & PSN as relaxor model compounds will be compared for non-resonance and resonance conditions at room temperature. Subsequently the observations will be set in context with the results from previous studies reporting about the structural state of lead-based perovskite-type relaxors with a complex occupied B site. Furthermore, selection rules for resonance Raman scattering will be derived and employed on the spectral features. After that, the effect of doping the A and/or B site on the structural state of the studied compounds under ambient conditions as well as the difference between the temperature evolution of Ba and La/Sr doped compounds will be discussed.

5.1 $\text{PbSc}_{0.5}\text{Ta}_{0.5}\text{O}_3$ (PST) & $\text{PbSc}_{0.5}\text{Nb}_{0.5}\text{O}_3$ (PSN) model compounds

RRS on the two model compounds PST & PSN at ambient conditions was first considered in order to apply group theory to the observed spectral features. One mayor point is to clarify in which way the complex nanoscale structure contributes to the RRS spectra and if there is a possibility to separate signals arising from non-polar and polar structural species.

5.1.1 RRS at ambient conditions

The RRS spectra of PST (Fig. 7) and PSN (Fig. 8) for $\lambda = 325$ nm (3.81 eV), well above the energy gap E_g (~ 3.2 eV) in the range of the maximum of the optical dielectric permittivity of both compounds (Mihailova, et al., 2007 a), show distinctive differences compared to the non-resonance spectra measured with an excitation wavelength of 514.5 nm (2.41 eV). RRS and non-resonant Raman scattering differ from each other first of all by a drastic change of intensity ratios. Under non-resonance conditions and with parallel polarization the peak with the highest wavenumber (~ 820 cm^{-1}) arises from the symmetrical stretching mode associated with the totally symmetric representation (A_{1g}) of the ideal, doubled perovskite structure. The RRS spectra by contrast additionally show features up to 1600 cm^{-1} . Under

resonance conditions two peaks around 440 cm^{-1} and 700 cm^{-1} related to antisymmetric BO_6 bending (AB) and stretching (AS) modes, respectively, are strongly enhanced. In addition, strong RRS near 1135 and 1405 cm^{-1} is observed for both PST and PSN, which should arise from multi-phonon processes.

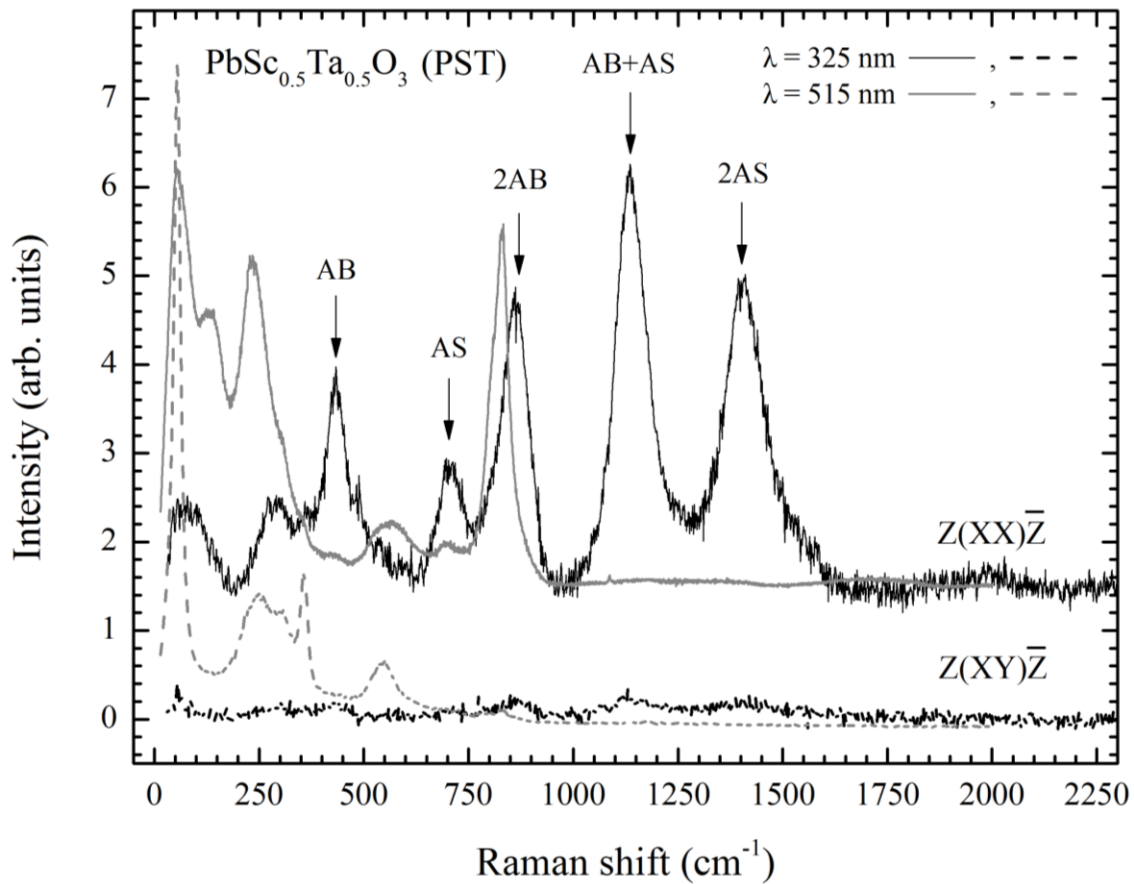


Fig. 7: Resonance (solid lines) and non-resonance Raman spectra (dashed lines) of PST ($\text{PbSc}_{0.5}\text{Ta}_{0.5}\text{O}_3$), measured in parallel (XX) and cross-polarized (XY) scattering geometry. The peaks arising from antisymmetric bending (AB) and antisymmetric stretching (AS) as well as the corresponding two-phonon scattering (two overtones and one combination) are labelled. The spectra are vertically shifted for clarity. The non-resonance spectra are normalized by the same coefficient to match the vertical size of RRS.

The signals near 430 and 700 cm^{-1} are associated with T_{1u} LO phonons that are IR-active for the ideal cubic perovskite structure and thus carry polarity. Hence, also the subgroup representations of cubic T_{1u} due to polar rhombohedral distortion are supposed to carry a certain amount of polarity. The enhancement of LO phonon modes due to RRS is well known to be triggered by electron-longitudinal-optical-phonon interaction, also called *Fröhlich interaction*. At the same time the peaks related to phonon modes comprising mainly vibrations of Pb and/or B-cations are strongly suppressed. The energy gap (E_g) of perovskite-type materials incorporating transition elements (with occupied d orbitals) on the B site is formed by the 2p level of oxygen and the d level of the B cation (Wolfram & Ellialtioglu, 2006, p. 8).

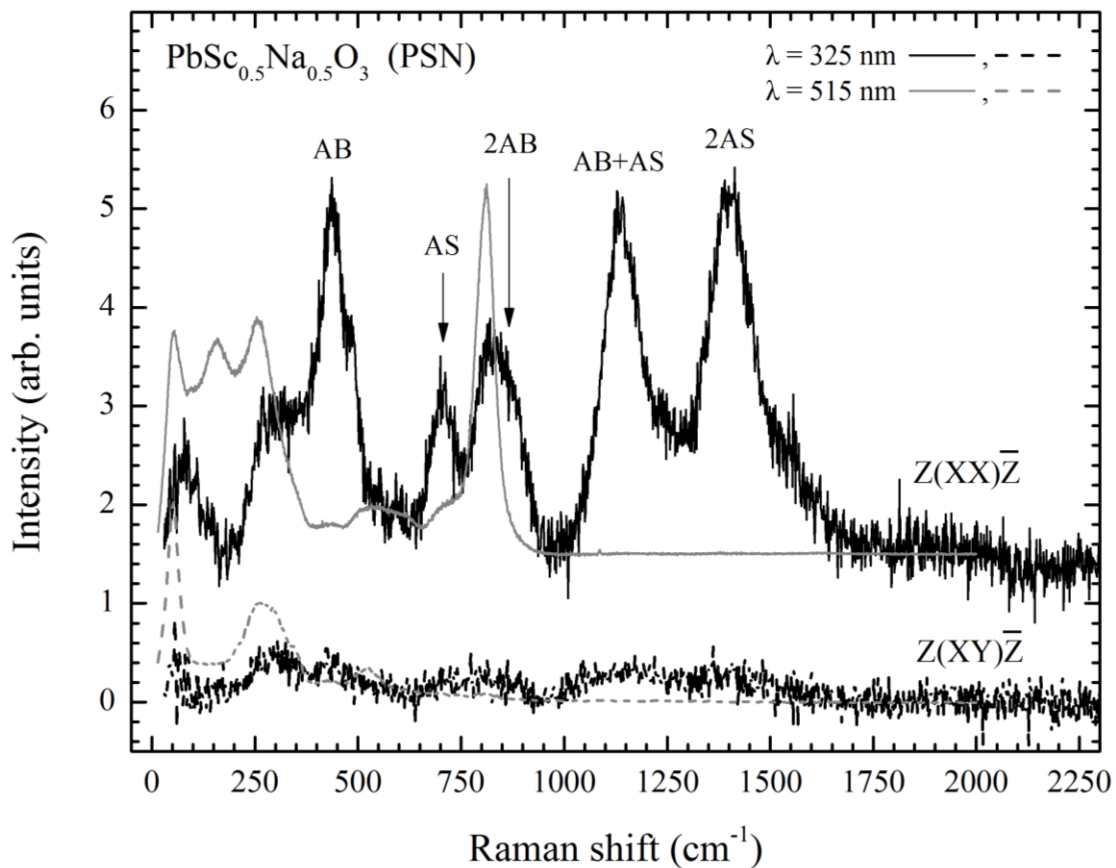


Fig. 8: Resonance (solid lines) and non-resonance Raman spectra (dashed lines) of PSN ($\text{PbSc}_{0.5}\text{Nb}_{0.5}\text{O}_3$), measured in parallel (XX) and cross-polarized (XY) scattering geometry. The peaks arising from antisymmetric bending (AB) and antisymmetric stretching (AS) as well as the corresponding two-phonon scattering (two overtones and one combination) are labelled. The spectra are vertically shifted for clarity. The non-resonance spectra are normalized by the same coefficient to match the vertical size of RRS.

Therefore, the excitation with photon energy above E_g is expected to enhance polar internal BO_6 modes due to their coupling with the intrinsic BO_6 electron transition regarding RRS and this can be confirmed by the measured spectra.

The appearance of strong peaks above 830 cm^{-1} is seen only under resonance conditions. They are most probably attributed to 2^{nd} -order Raman scattering (two-phonon scattering). This can be confirmed by comparing the wavenumber ratio of 1^{st} - and expected 2^{nd} -order scattering. By the tolerance of small deviation, the wavenumber of overtones and combinations should be equal to the sum of the wavenumbers of the corresponding fundamentals (Table 4). The wavenumber deviation for all 2^{nd} -order scattering peaks concerning their corresponding fundamentals sum is lower than 1 %. Additionally, this is in accordance with the approach of Fröhlich interactions since this mechanism is well known to enhance 2^{nd} -order Raman scattering (Abrashev, et al., 1997; Andreasson, et al., 2008).

Table 4: Peak positions of 1^{st} -order RRS generated by antisymmetric BO_6 bending (AB) and antisymmetric BO_6 stretching (AS) as well as the corresponding 2^{nd} -order RRS by 2AB, AB+AS and 2AS for PST and PSN at ambient conditions in cm^{-1} . Good accordance of the wavenumber for 1^{st} - and 2^{nd} -order RRS confirms the origin of the observed spectral features.

	AB	AS	2AB	AB+AS	2AS
PST	435 ± 1	707 ± 1	865 ± 2	1135 ± 1	1408 ± 1
PSN	439 ± 1	706 ± 1	871 ± 6	1137 ± 1	1403 ± 1

As mentioned in section 3.5, concerning the conservation of momentum 2^{nd} -order Raman scattering in principle is allowed to arise from phonons throughout the whole FBZ (Sherwood, 1972, p. 145). For Fröhlich interactions the contribution of phonons follows a dispersion relation of q^{-1} , where q is the phonon wavevector. Thus, especially Γ -point phonons are involved in Fröhlich interactions. This is due to the fact, that the largest magnitude of atomic displacement in LO modes is achieved for small values of q . If there would be a considerable contribution of zone-edge phonons to the 2^{nd} -order Raman scattering, the corresponding peaks would be expected to show several maxima according to the two-phonon density of states including non-center phonons at high symmetry points of the FBZ (at least for a comparable strong dispersion of the fundamental phonon modes).

In addition to 2^{nd} -order, also 3^{rd} -order Raman scattering can be observed in the spectra. For example, the peak around 1260 cm^{-1} towered over by the 2^{nd} -order features is attributed to

be a triple overtone of the antisymmetric BO_6 bending ($\approx 3\cdot 430\text{ cm}^{-1}$). In the same manner the peak around 2000 cm^{-1} probably is a triple overtone of antisymmetric BO_6 stretching ($\approx 3\cdot 700\text{ cm}^{-1}$). By careful consideration also peaks from three-phonon combinations can be observed around $1560 (2\cdot\text{AB} + \text{AS})$ and $1830\text{ cm}^{-1} (\text{AB} + 2\cdot\text{AS})$.

The cross-polarized spectra measured under resonance conditions of both PST and PSN show nearly negligible intensities compared to the parallel polarization. Under non-resonance conditions especially there is a peak associated with cubic T_{2g} representation arising from Pb-localized vibrations around 55 cm^{-1} . Thus, also the cross-polarized spectra indicate strong suppression of Pb- and B-cation localized modes, explicitly of those that are related to the cubic non-polar matrix.

Which phonon modes are Raman-active under non-resonance conditions for the cubic matrix ($\text{Fm}\bar{3}\text{m}$) can be predicted by Raman selection rules as mentioned in section 3.6. In the next section, selection rules for resonance Raman scattering regarding studied perovskite-type relaxors will be derived.

5.1.2 Selection rules for resonance Raman scattering on perovskites

The prototype (aristotype) structure of PST and PSN is cubic with symmetry $\text{Pm}\bar{3}\text{m}$ (single-perovskite) or $\text{Fm}\bar{3}\text{m}$ (doubled-perovskite) depending on whether the compounds do not or exhibit chemical 1:1 B-site order. Most of the compounds studied here show subtle or no long-range B-site chemical order, according to X-ray and neutron diffraction. However, all compounds possess chemical B-site order on the length scale of sensitivity of Raman spectroscopy.

Furthermore, these materials show intermediate-range polar as well as antiferrodistortive ferroic order. The intermediate-range order evolves at low temperatures into rhombohedral long-range ferroelectric order with symmetry $R\bar{3}\text{m}$ or $R\bar{3}$ depending on whether it starts from single- or doubled- perovskite structure, respectively. Under high pressure the antiferrodistortive ferroic order develops into long-range order according to the same principle by transforming into $R\bar{3}\text{c}$ or $R\bar{3}$. In order to derive RRS selection rules from group

theory analysis, all the corresponding point groups of the mentioned space groups have to be considered.

Deriving selection rules for RRS requires the appropriate combination of vibrational as well as electronic selection rules (de la Flor, et al., 2014). Dipole electron transitions are symmetrically allowed (Eq. 10) if the direct product of the representation of the initial electron state (Γ_{e^i}), the vectorial representation (Γ_V) and the final electron state representation (Γ_{e^f}) contains the totally symmetric irreducible representation (A).

$$\Gamma_{e^i} \otimes \Gamma_V \otimes \Gamma_{e^f} \subset A \quad \text{Eq. 10}$$

For those electron transitions which are symmetrically allowed, the formula can be expanded by the contribution of compatible phonon modes. Therefore, the initial (Γ_{v^i}) and the final vibrational state (Γ_{v^f}) are also taken into account (Eq. 11).

$$\Gamma_{e^i} \otimes \Gamma_{v^i} \otimes \Gamma_{e^f} \otimes \Gamma_{v^f} \cap \Gamma_{[V^2]} \neq 0 \quad \text{Eq. 11}$$

The formula can be simplified by cutting the initial vibrational state, since the transition usually starts from the vibrational ground state and the corresponding representation is totally symmetric ($\Gamma_{v^i} = A$). Involving this character into a product is similar to a multiplication by unity and hence does not change the result. In this respect the formula can be given as:

$$\Gamma_{e^i} \otimes \Gamma_{e^f} \otimes \Gamma_{v^f} \cap \Gamma_{[V^2]} \neq 0 \quad \text{Eq. 12}$$

Eq. 12 implies that a vibrational transition under resonance conditions is symmetrically allowed, if the intersection between the symmetrized square of the vector representation $\Gamma_{[V^2]}$ and the direct product of the representations of all considered states differs from zero.

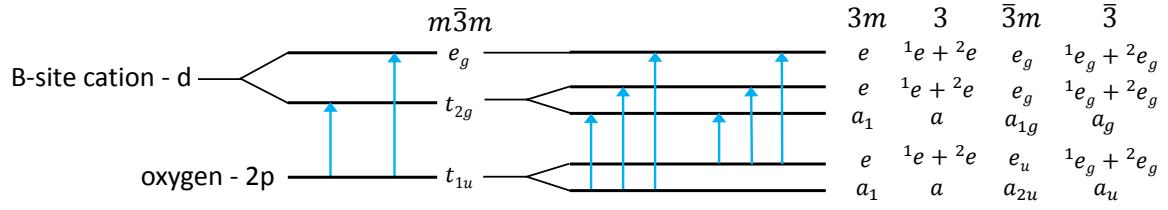


Fig. 9: Splitting of the electron states of B-cation d and oxygen 2p level for the cubic point symmetry ($m\bar{3}m$) representing the non-polar matrix. Additionally, splitting of electron states due to rhombohedral deviation from the ideal cubic structure in the form of polar ferroic ($3m, 3$) and antiferrodistortive ferroic species ($\bar{3}m, \bar{3}$) is illustrated. In contrast to phonon modes, the irreducible representations of electron states are labeled following the Mulliken notation, but lowercase letters are used instead of uppercase.

As already mentioned, the band gap in perovskites with a transition metal (partially filled d subshell) on the B site is usually determined by the oxygen p level at the top of the valence band and the B-site cation d level at bottom of the conduction band.

The symmetry of the aristotype perovskite structure is represented by the point group $m\bar{3}m$, in which the p-electron state transforms as a triply degenerate representation (t_{1u}), whereas the d-electron state of the octahedrally coordinated cation transforms as a doubly (e_g) and a triply (t_{2g}) degenerate representation (Fig. 9). Thus two electron transitions are possible: (i) from initial t_{1u} to final t_{2g} and (ii) from initial t_{1u} to final e_g .

Table 5: Group-subgroup relation between the irreducible representations of the cubic aristotype perovskite structure and the rhombohedral polar as well as the antiferrodistortive structural deviations, respectively. Irreducible representations that are Raman-active under non-resonance conditions are marked red. Representations put in large brackets are complex conjugated but only one peak would be detected due to them. The relations have been calculated by using the tool "CORRELATIONS POINTS" of the Bilbao Crystallographic Server (Aroyo, et al., 2006 a; Aroyo, et al., 2006 b; Aroyo, et al., 2011).

Cubic matrix	Polar structure		Antiferrodistortive structure	
	$3m$	3	$\bar{3}m$	$\bar{3}$
A_{1g}	*	A	*	A_g
E_g	*	$\{^2E, ^1E\}$	*	$\{^2E_g, ^1E_g\}$
T_{1g}	*	$A + \{^2E, ^1E\}$	*	$A_g + \{^2E_g, ^1E_g\}$
T_{1u}	$A_1 + E$	$A + \{^2E, ^1E\}$	$A_{2u} + E_u$	$A_u + \{^2E_u, ^1E_u\}$
T_{2g}	*	$A + \{^2E, ^1E\}$	*	$A_g + \{^2E_g, ^1E_g\}$
T_{2u}	$A_2 + E$	$A + \{^2E, ^1E\}$	$A_{1u} + E_u$	$A_u + \{^2E_u, ^1E_u\}$

* subgroup-related irreducible representations which are not present for $Pm\bar{3}m$

By applying these considerations to Eq. 10 both electron transitions are found to be symmetrically allowed. Following this, the selection rules for 1st-order RRS can be calculated by applying the irreducible representations of $Fm\bar{3}m$ symmetry (Table 2) to Eq. 12. After performing these calculations for all possible combinations of electron states and vibrational irreducible representations by applying $\Gamma_V = t_{1u}$ and $\Gamma_{[V^2]} = a_{1g} + e_g + t_{2g}$, it appears that for the cubic matrix only T_{1u} and T_{2u} modes are allowed to give rise to RRS triggered by the intrinsic BO_6 related electron transition. In contrast to T_{1u} modes, T_{2u} modes do not carry polarity and thus they are not capable to be enhanced via Fröhlich interaction. For the rhombohedral distortion of the cubic symmetry, the electron states further split and the number of possible transitions increases (Fig. 9). For space groups that are associated with the antiferrodistortive ferroic order ($R\bar{3}c$ and $R\bar{3}$) many phonon modes are allowed to be resonantly enhanced. However, for $R\bar{3}c$ resonance Raman scattering is forbidden in connection with A_{1g} , A_{2g} and E_g , and for $R\bar{3}$ when A_g and E_g are involved. By taking into account the group-subgroup relation of representations (Table 5) in connection with the atomic displacements of the corresponding vibrations (Table 2) it can be established that symmetrical stretching of BO_6 octahedra from non-polar structural species is not allowed to give rise to RRS when this certain electron transition from oxygen p to B-cation d level is concerned.

For polar rhombohedral symmetry ($3m$ and 3) all irreducible representations and thus signals associated with all vibrations are allowed to be enhanced under resonance conditions.

5.1.3 Selection rules for multi-phonon resonance and non-resonance Raman scattering

The selection rules for multi-phonon, non-resonance and resonance Raman scattering concerning the Γ -point phonons can be calculated by the direct product of the symmetrical representations of all participating phonons. The direct product must contain at least one Raman-active symmetrical representation (de la Flor Martin, 2013, p. 141).

In this context, under non-resonance conditions overtones and combinations of the Raman-active cubic representations A_{1g} , E_g and F_{2g} related to the cubic matrix are allowed. But also modes that are forbidden for 1st-order Raman scattering may be allowed to contribute to 2nd-order Raman scattering.

For example, the direct product of T_{1u} and T_{1u} contains even three Raman-active irreducible representations (red-labeled in Eq. 13) and therefore overtones of T_{1u} are symmetrically allowed under non-resonance conditions. However, the 2nd-order Raman scattering of PST and PSN is extremely weak under non-resonance conditions (see Fig. 7 and 8).

$$T_{1u} \otimes T_{1u} \subset A_{1g} + E_g + T_{2g} + T_{1g} \quad \text{Eq. 13}$$

Whether the 2nd-order scattering of certain phonon modes is symmetrically allowed under resonance conditions can be calculated by the direct product of the two participating phonons irreducible representations, including the RRS selection rules given in section 5.1.2. Thus, following the selection rules for 2nd-order RRS, the direct product of the multi-phonon involved representations is applied to Eq. 12 as the final vibrational state Γ_{vf} .

If the selection rules for 2nd-order RRS from the cubic matrix with point symmetry $m\bar{3}m$ are taken into account, it can be proven that overtones and combinations of representations having the same parity (e.g. “g” and “g” or “u” and “u”) are not allowed. Particularly overtones and combinations of T_{1u} modes including internal antisymmetric BO_6 vibrations are forbidden for both possible electron transitions between the oxygen electron p level and the B-cation d levels. The same applies to overtones and combinations of non-polar rhombohedral symmetries ($\bar{3}m$ and $\bar{3}$). Only for the polar rhombohedral symmetries ($3m$ and 3) all overtones and combinations are symmetrically allowed to become enhanced by RRS under these specific conditions.

By taking into account the selection rules for 1st- and 2nd-order RRS and combining them with the assumption that Fröhlich interactions are the crucial mechanism of resonance enhancement of Raman scattering for perovskite-type relaxor ferroelectrics, it is possible to draw some conclusions. The simultaneous enhancement of the fundamental Raman scattering from BO_6 antisymmetric bending and stretching around 430 and 700 cm^{-1} as well as their overtones and the combination around 870, 1405 and 1135 cm^{-1} , is exclusively

allowed only in *polar* structures, i.e. the observed RRS is explicitly related to *polar* structural species (de la Flor, et al., 2014). From this point of view, it might be possible to selectively study polar structural species i.e. PNR by applying resonance Raman spectroscopy.

5.1.4 RRS at different temperatures

As already mentioned, the behavior of PNR strongly depends on temperature. Thus, by considering the evolution of RRS as a function of temperature, it should be possible to confirm what is indicated by selection rules and theoretical contemplations.

Under non-resonance conditions the spectra of PST show a considerably large intensity at high temperatures, prevalently from those phonon modes related to the cubic matrix. Under

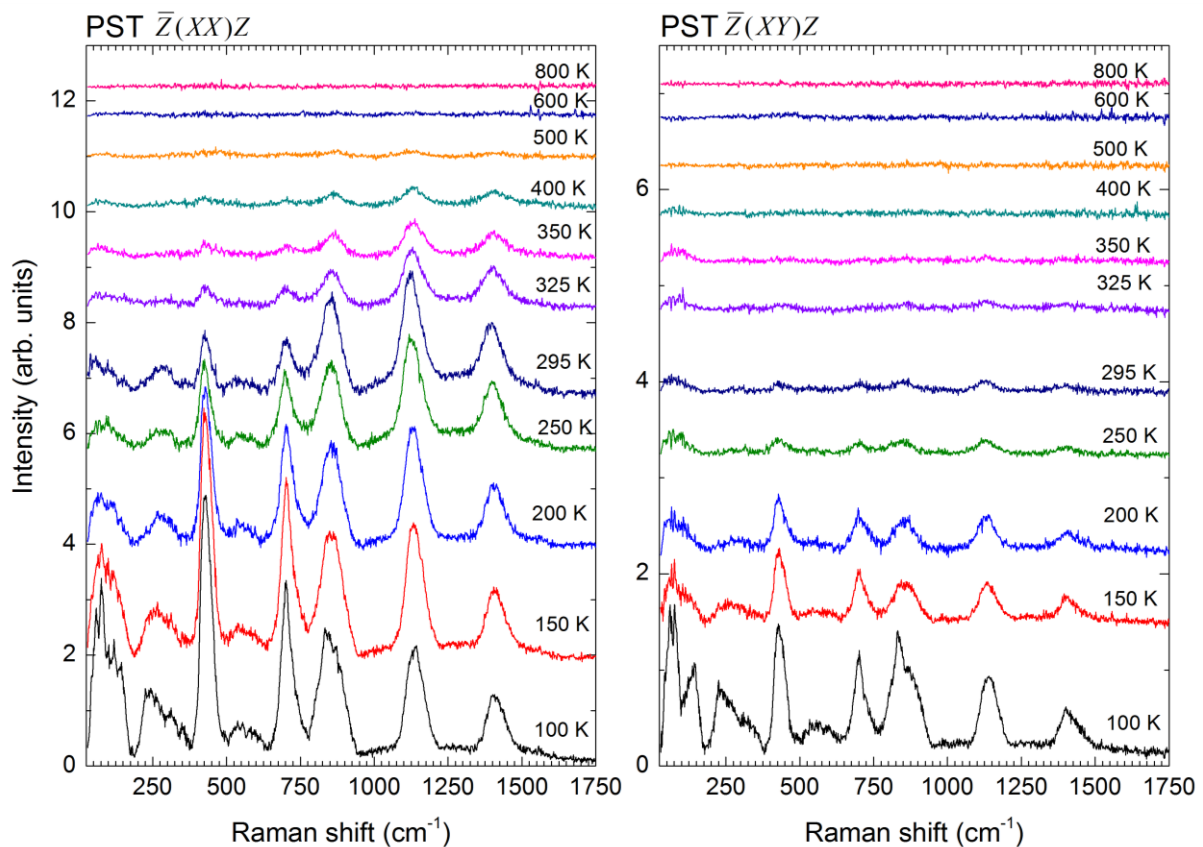


Fig. 10: Temperature dependent parallel and cross-polarized RRS of PST. The spectra are shifted vertically for clarity. On cooling signals start to appear at temperatures near T^* .

resonance conditions, in the vicinity of T_B , where PNR nucleate, RRS signals could be detected neither in the parallel nor in cross-polarized spectra (Fig. 10). This behavior indicates that the Fröhlich interactions for polar phonons of the cubic phase are too weak to

generate RRS detectable with the experimental setup used. With decreasing temperature reaching the proximity of T^* , scattering intensities are distinctly enhanced. Since at T^* PNR merge and become substantially larger the associated electric fields simultaneously increase in magnitude. As a consequence Fröhlich interactions are supposed to become amplified and enhance the intensity of peaks that are related to PNR.

At further cooling the overall scattering intensity strongly increases, while especially the signals in the range from 50 to 200 cm^{-1} are significantly enhanced. At the same time, the depolarization ratio increases as can be seen in the cross-polarized spectra. This trend is mainly due to the phase transition that PST undergoes around 280 K. The depolarization indicates the development of ferroelectric long-range order.

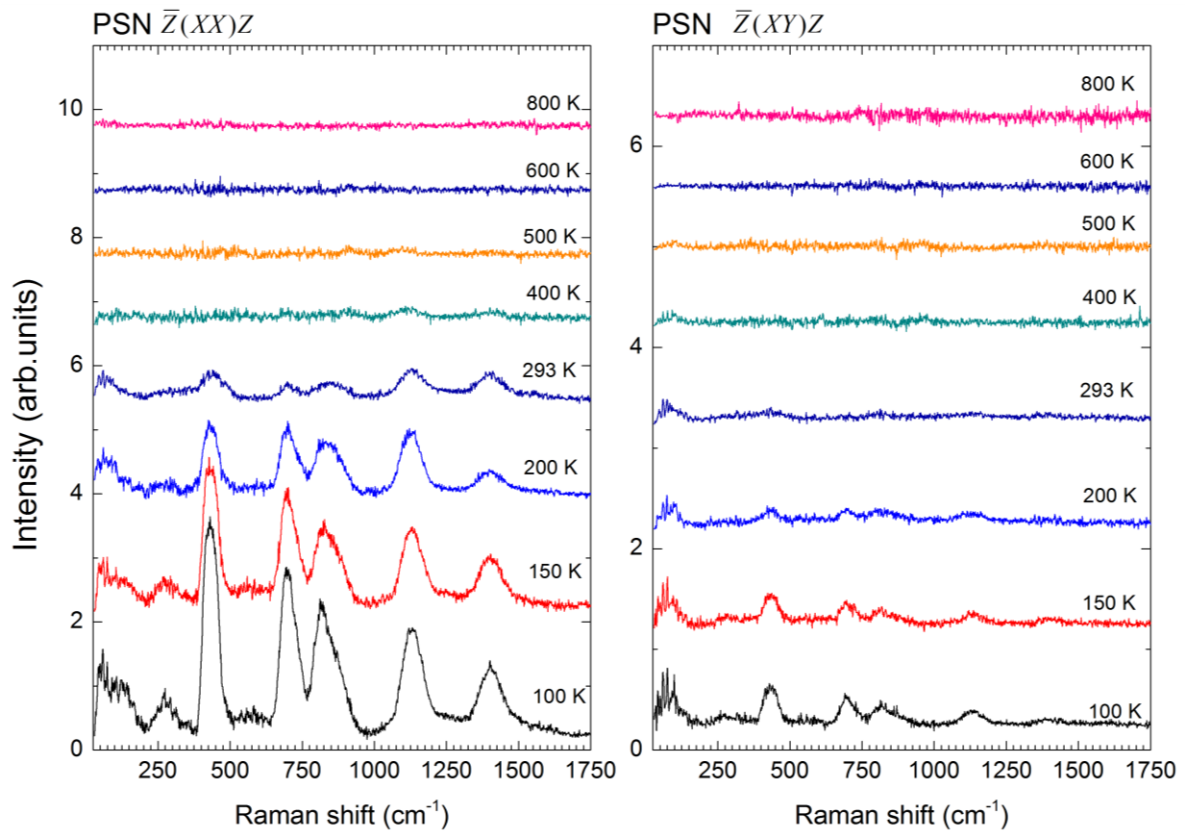


Fig. 11: Temperature dependent parallel and cross polarized RRS of PSN. The spectra are shifted vertically for clarity. On cooling signals start to appear at temperatures near T^* .

A very similar trend can also be observed for PSN (Fig. 11). However, the depolarization ratio of RRS for PSN is less pronounced as compared with PST. This is in accordance with the fact that the coherence of polar coupling as well as the size of ferroelectric domains is less in PSN

(Mihailova, et al., 2005), although T_c around 370 K is at higher temperatures compared to PST. The temperature evolution of the RRS for both compounds confirms the assumption that RRS arises only from polar structural species, while the scattering from the non-polar cubic matrix is completely suppressed. Therefore one can conclude, that the intensity of RRS is directly correlated with the size or magnitude of spontaneous polarization of spatial polar regions (PNR or ferroelectric domains), which in turn is determined by the individual polarity of the polar species and the length of coherence between the individual polar species. The letter actually represents the mean size of PNR or ferroelectric domains.

The temperature dependent measurements of PST and PSN also reveal that the spectral feature between 800 and 880 cm^{-1} is not only composed of the 2nd-order RRS from antisymmetric bending around 430 cm^{-1} but also contains contribution from symmetrical BO_6 stretching which in the cubic prototype structure is associated with the totally irreducible representation A_{1g} . This mode is not supposed to carry polarity in non-centrosymmetric structures but it also becomes enhanced under resonance conditions, indicating a polar doubled-perovskite structure.

5.1.5 RRS at high pressures

Resonance Raman spectra under high pressure have been conducted for PST (Fig. 12). The spectral feature corresponding to the overtone of antisymmetric stretching unfortunately could not be evaluated, since there was a strong contribution by the diamond anvils above 1250 cm^{-1} . Thus, the pressure-dependent spectra are cut after the combinational mode of antisymmetric bending and stretching. PST undergoes pressure-induced phase transitions at $p_{c1} = 1.9$ GPa (Mihailova, et al., 2008 b) and p_{c2} around 5.5 GPa (Maier, et al., 2011 b). At p_{c1} PST develops long-range antiferrodistortive BO_6 tilts with rhombohedral symmetry where this structural state is supposed to be non-polar due to a center of inversion ($R\bar{3}$). With increasing pressure at p_{c2} a further lowering of the symmetry occurs including antiparallel Pb^{2+} displacements as well as mixed in- and antiphase tilts of BO_6 octahedra, where the space group of the latter phase was awaited to be $P2_1/c$.

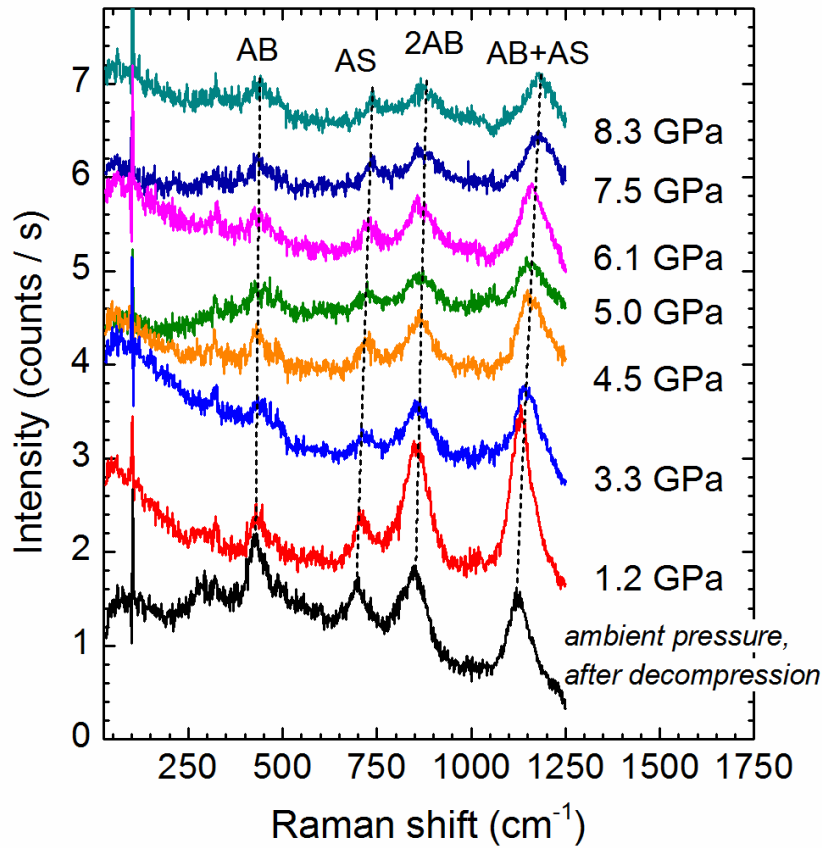


Fig. 12: Parallel polarized resonance Raman spectra of PST under high pressure at room temperature. The spectra are vertically shifted for clarity. The spectrum at ambient pressure has been collected after decompression.

It follows from the group theory analysis, that for both symmetries ($R\bar{3}$ and $P2_1/c$) the simultaneous enhancement of 1st- and 2nd-order RRS is symmetry-forbidden. Consequently, the high pressure structural state of PST even well above p_{c2} has a partial *polar* character and in addition the implicit polar structural species is distinctive enough to give rise to RRS. Since under ambient conditions signals at first appear in the vicinity of T^* , the remaining polar order under high pressure must produce sufficient magnitudes of electric field to be worth noting and hence cannot be entirely suppressed by the domination of antiferrodistortive ferroic order. Thus, in despite of structural relaxation via antiphase tilts, the BO_6 octahedra are slightly distorted from their ideal shape even under high pressure.

The sensitivity of RRS for structural polarity appears to be rather high and it can be shown that resonance Raman spectroscopy in general possesses a certain potential to study local structural inhomogeneities of advanced ferroelectric materials.

5.2 Effect of doping

In this section the resonance Raman spectra of doped PST and PSN are treated. The effects of doping on the structural state are basically determined by previous studies as mentioned in section 4.1. In this sense, the spectral evolution of RRS as a function of A- and B-site doping is compared with available information about the single compounds, in order to prove the potential of RRS to distinguish between different types of polar distortions and different mechanisms of coupling processes.

5.2.1 RRS at room temperature

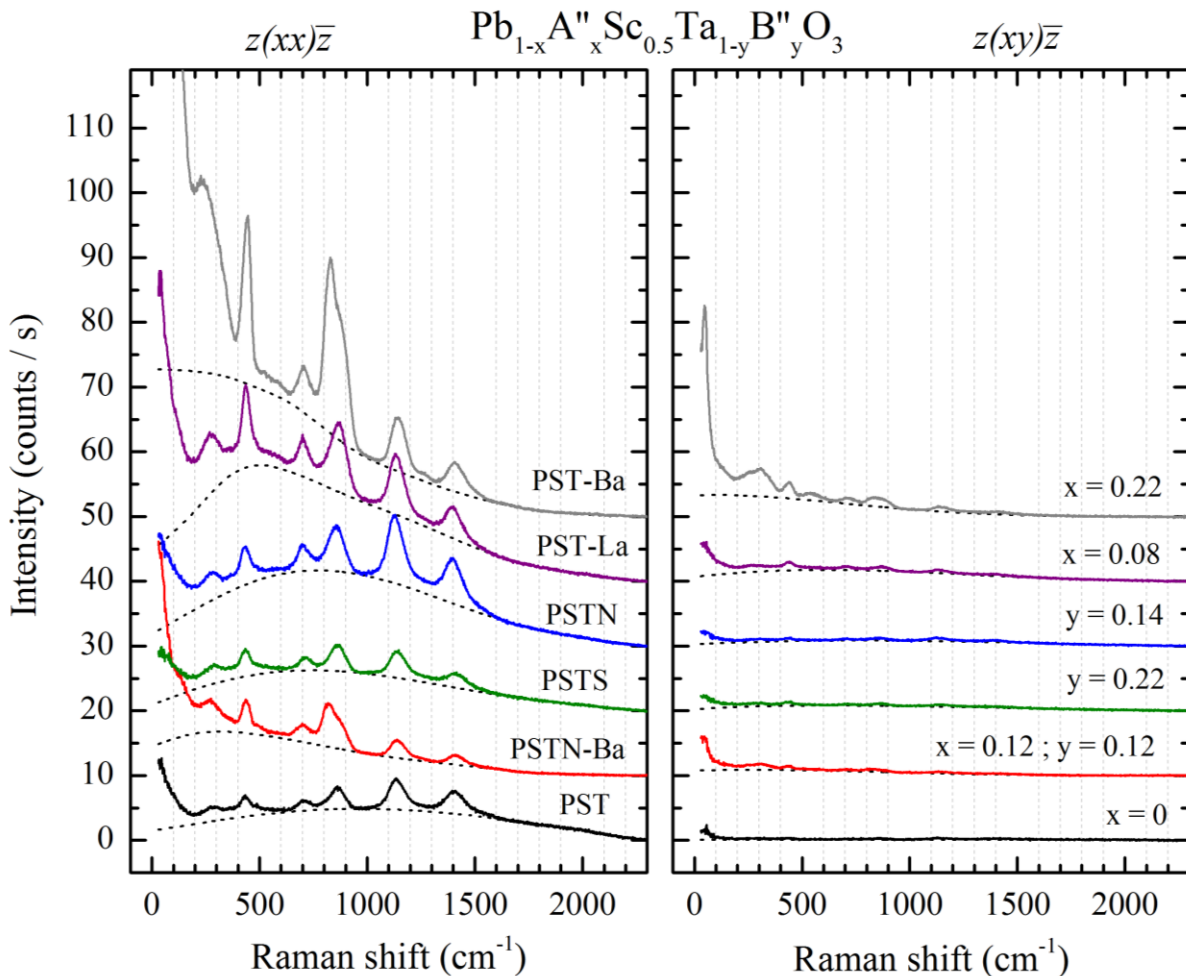


Fig. 13: Parallel and cross polarized RRS spectra of PST related compounds. Spectra are only corrected for the glass-contribution but not for the Bose-Einstein distribution and vertically shifted for clarity. The intensity and the position of the continuum photoluminescence maximum (dotted lines) are different for all compounds. Especially PST-Ba shows very strong luminescence background with maximum very close to the incident photon energy.

RRS spectra from all doped PST and PSN were collected at ambient conditions. The spectra are expected to provide information about the vibrational as well as the electronic states of the studied materials. In this manner, one spectral feature which can be observed for all compounds is directly related with the electron band structure of the single compounds: there is an obvious appearance of photoluminescence as a background. Fig. 13 shows the as-measured spectra for all PST-compounds, where only the glass-contribution has been subtracted. The strong slope for low wavenumbers is owed to the already mentioned thermal population of vibrational states following the Bose-Einstein distribution (Eq. 8). The parallel polarization spectra are plotted on the left-hand side. Each sample shows a different

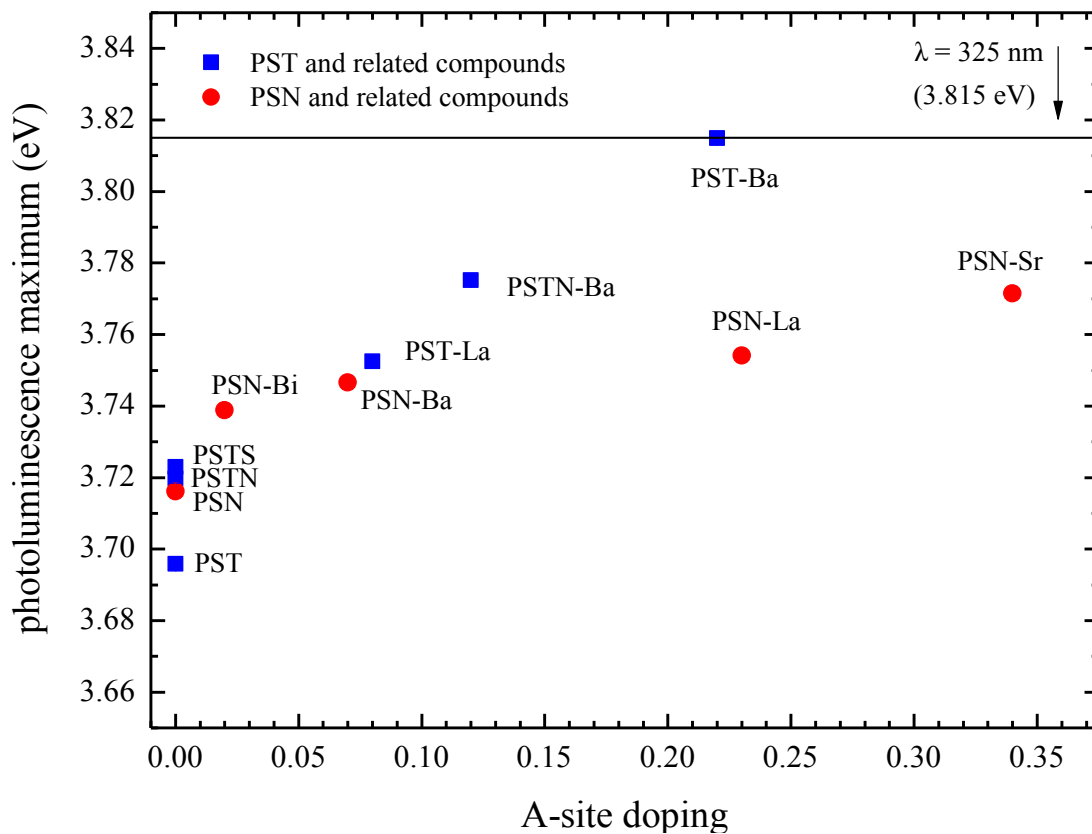


Fig. 14: Maxima of the continuum photoluminescence background for PST and PSN as well as their related doped compounds. For nearly all compounds there is a clear energy down shift with respect to the incident laser energy. Only PST-Ba shows a photoluminescence maximum that is very close to the excitation wavelength of 325 nm. For all samples the error is below 0.002 eV.

photoluminescence background, while for all materials except for PST-Ba the maximum of this background distinctly is within the spectral range of strong Raman scattering. The shift of the luminescence maximum for different compounds should be due to a change in the electronic band structure induced by different amount and type of doping. In general, photoluminescence is a Stokes process (Kitai, 1993, p. 25), thus the maximum of

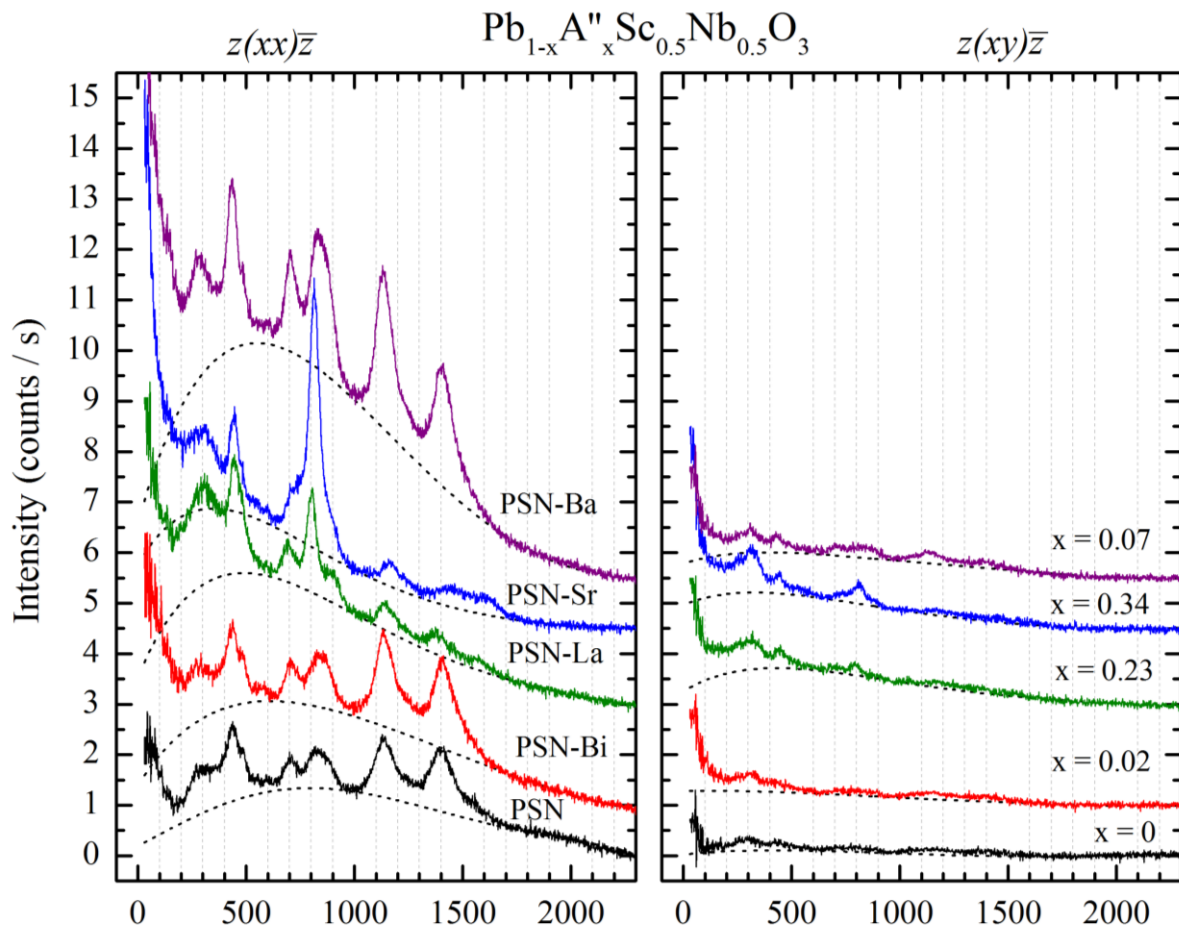


Fig. 15: Parallel and cross polarized RRS spectra of PSN related compounds. Spectra are only corrected for glass-contribution but not for the Bose-Einstein distribution and vertically shifted for clarity. The intensity and the position of the continuum photoluminescence maximum (dotted lines) are different for all compounds.

luminescence is expected to be at lower energy compared to the incident photon. The difference in energy between the absorbed and the emitted photon can be due to different effects here. One aspect is the influence of doping on the energy gap and on the optical dielectric permittivity maximum, respectively. Another point might be how the relaxation of the excited electron level proceeds. If the emission of the photon starts from the vibrational ground level of the excited electron state following Kasha's rule, then the difference in the photon energy corresponds to the gap between the involved electron states. If there is

practically no relaxation and the photon is emitted from the excited vibrational level of the excited electron state, it is about so-called hot luminescence. In Fig. 14 the maxima of the luminescence signals for all measured samples are plotted. It appears that the pure compounds show the largest shift with respect to the excitation wavelength of 325 nm. With the increasing amount of A-site doping the difference decreases with a higher slope for PST and its related compounds. Eventually, for PST-Ba there is at least no detectable shift of the luminescence maximum. All of this presumably indicates that heavy A-site doping considerably influences the electron configuration with respect to pure PST especially when

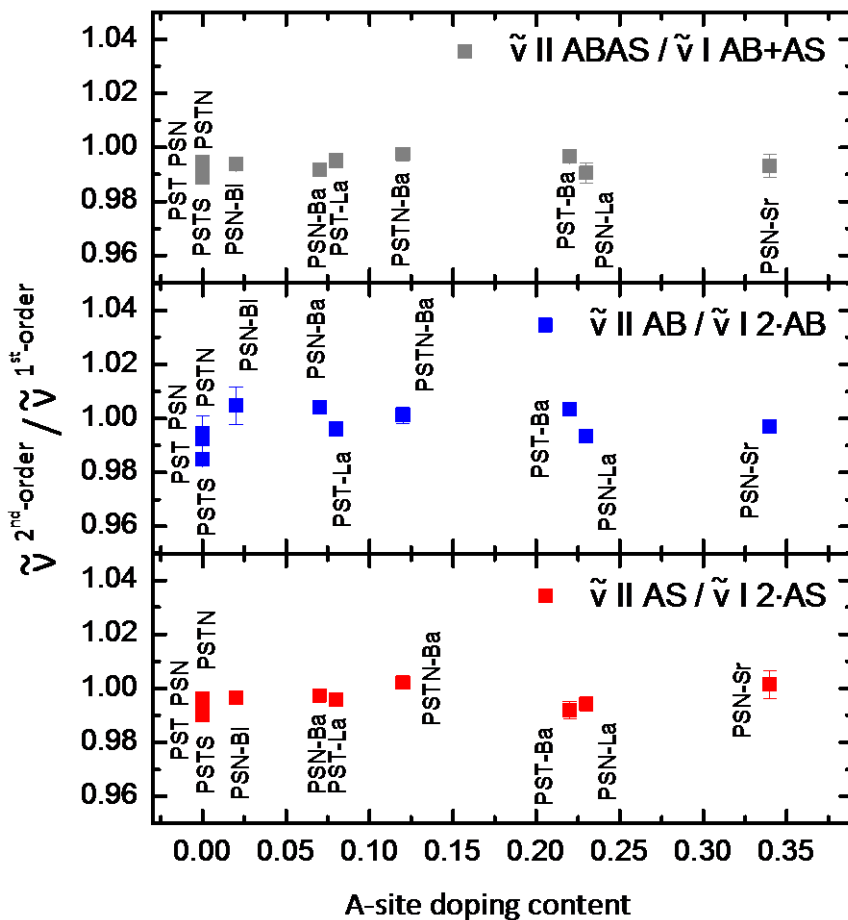


Fig. 16: The wavenumber-ratio of 2nd (II) and corresponding 1st (I) order RRS. The upper part shows the ratio of antisymmetric bending (AB) + antisymmetric stretching (AS) vs. the combinational mode (ABAS). In the middle antisymmetric bending and its overtone are plotted. The lower part shows the antisymmetric stretching and its overtone. For all compounds and vibrational modes, the ratio is nearly equal to unity.

luminescence shows a noticeable degree of depolarization for PSN-Ba, PSN-La and PSN-Sr. If the spectra of PST and the related doped compounds are considered carefully, it can be observed that also for the A-site doped PST compounds there is a depolarization of the

Pb is partially substituted for Ba. On the right-hand side of Fig. 13 the cross polarized spectra are plotted. For all measured compounds except for PST-Ba the depolarization ratio of the luminescence is extremely low. Fig. 15 shows all measured spectra related with PSN. These spectra show similar trends as those of PST with some interesting differences.

Considering the cross-polarization spectra it can be seen that the

photoluminescence, whereas the pure compounds and those with doping on the B-site preferably show no depolarization of the same. Hence, this is further evidence that A-site doping has a considerable impact on the electron configuration although the energy gap basically is formed by oxygen and B-site cation levels. This is generally supposed to be due to defects induced by the complex A-site occupancy and the responding B-site-cation arrangement.

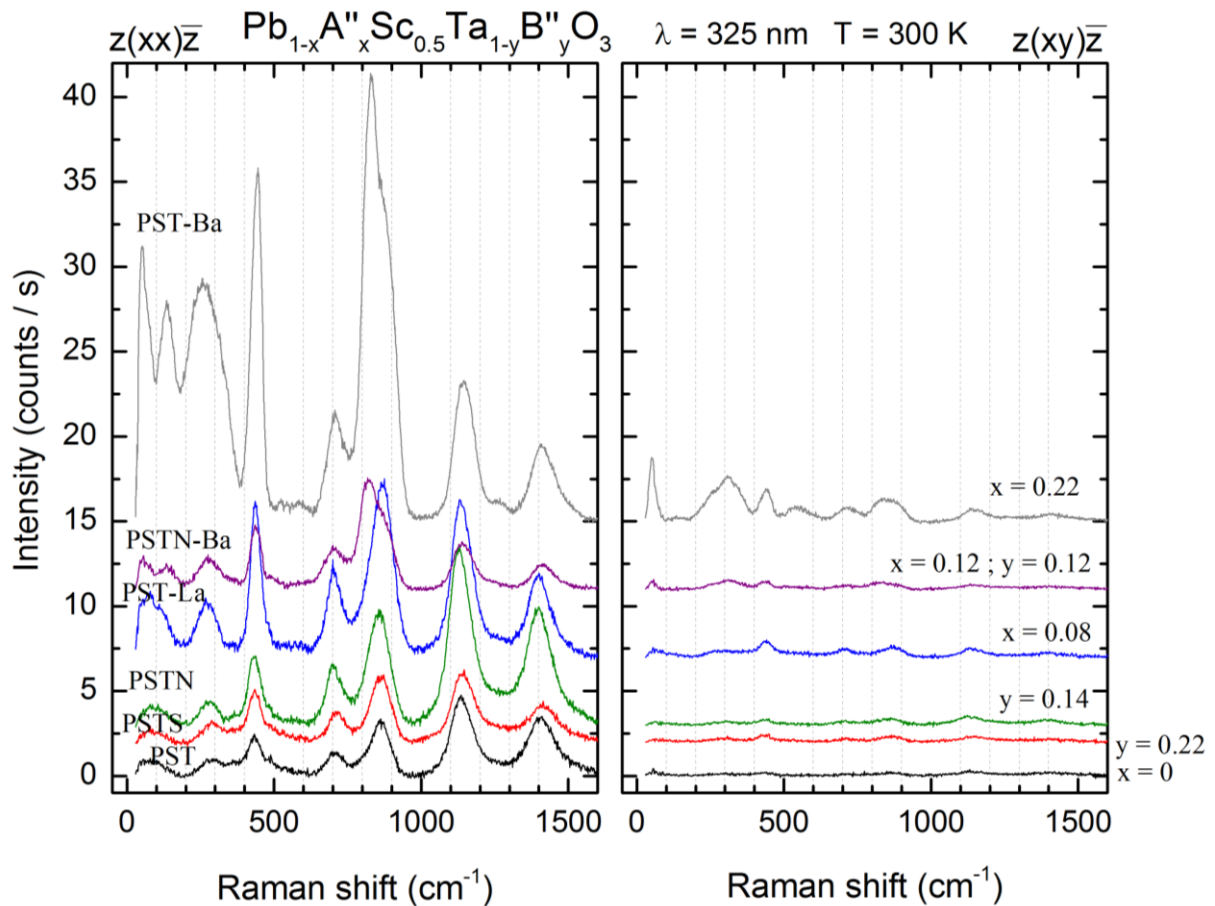


Fig. 17: Parallel and cross-polarized spectra of PST-related compounds at ambient conditions. The spectra have been corrected for the contribution of photoluminescence and are vertically shifted for clarity.

In the subsequent analysis the focus is put on the Raman signals. All collected spectra show features related to 2nd-order RRS. As already mentioned in section 3.5, multi-phonon scattering enables contribution of zone-edge phonons in Raman spectra. Thus, the 2nd-order RRS in the spectra might be the sum of interactions between zone-center as well as phonons with $q \neq 0$. In the latter case relatively large deviation of the 2nd-order RRS peak positions from the sum of the corresponding 1st-order peak positions is expected. If however the main mechanism of RRS is Fröhlich interaction, mainly zone-center phonons are active in RRS.

Nevertheless, the mechanism responsible for enhancement of single phonon modes in the spectra carrying strong polarity is supposed to be Fröhlich interactions. Zone-edge phonons are not capable to generate long-range electric fields due to the fact that the scalar potential magnitude of the longitudinal electric field is inversely proportional to the phonon wavevector. Therefore the signals of 2nd-order RRS should correspond to zone-center phonons. As already done for PST and PSN in section 5.1.1, this can be proven by considering the wavenumber-ratio of 2nd- vs. the corresponding sum of 1st-order RRS (Fig. 16). In all three cases the ratio is equal to unity within a deviation range of $\sim 1\%$. A small deviation is expected due to the downshift of energy for 2nd-order scattering by the binding energy in phonon-phonon interaction. From this it follows that for all compounds, the 2nd-order RRS mainly arises from Γ -point phonons. In addition, by this ratio it can be confirmed that all peaks above 830 cm^{-1} arise from 2nd-order RRS.

Signals explicitly arising from RRS can be evaluated easier by subtracting the

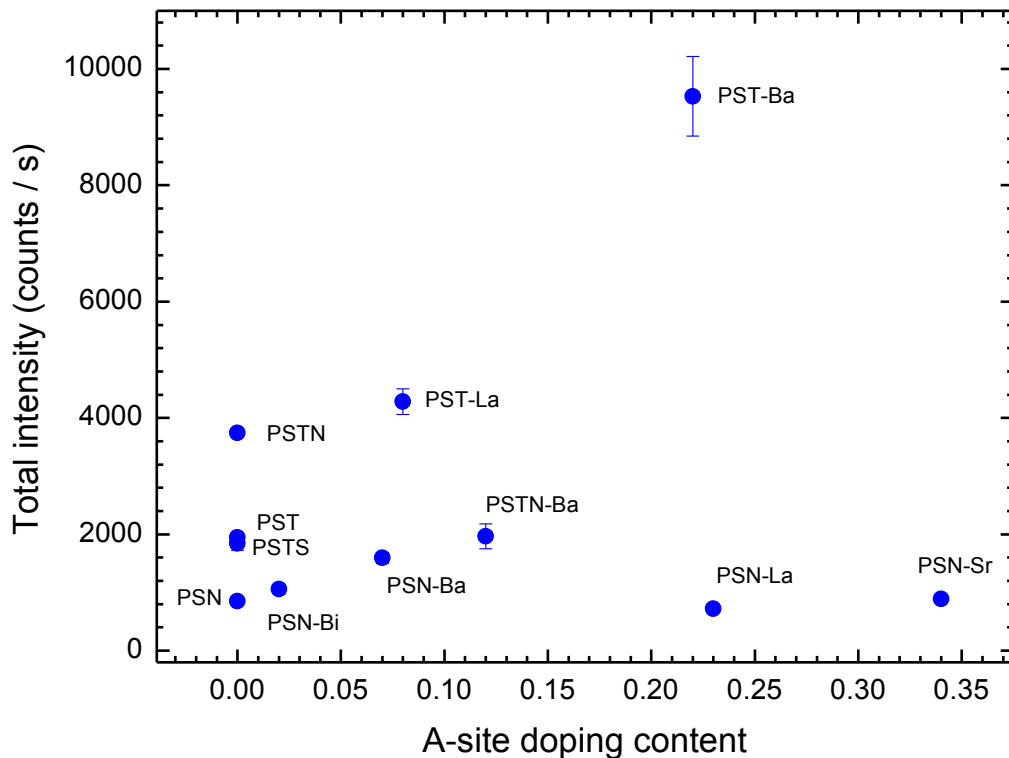


Fig. 18: Total scattering intensity of the RRS spectra of all measured samples at ambient conditions in counts per second (cps) upon scattering geometry $\bar{Z}(XX)Z$.

photoluminescence. This has been done for all measured spectra (Fig. 17 and 19). At first glance it has to be that the total scattering intensity changes with doping. This is especially

valid for PST compounds and minor for PSN compounds. At this point, it should be mentioned that the total scattering intensity depends on several parameters e.g. the focusing, thus this quantity has to be considered carefully to avoid over-interpretation. With respect to all other compounds, PST heavily doped with Ba shows much stronger total scattering intensity (Fig. 18). Furthermore, compared to all other materials, PST-Ba additionally shows a strong enhancement of RRS between 50 and 300 cm^{-1} , which is dominated by modes involving Pb- and B-site cation vibrations.

The reason for all of this is most probably the same as for the remarkable position of the photoluminescence maximum for PST-Ba: The heavy A-site doping influences the electron-band structure in such a way, that the transition energy is noticeably shifted. Optical transmittance spectra from previous studies (Marinova, et al., 2006) show that for heavy doping with Ba the energy gap is shifted from 3.2 to 3.4 eV compared to pure PST at room temperature. Besides, two additional absorption peaks in the visible range were detected near 460 and 730 nm. These measurements indicate that Ba^{2+} has an impacting influence on the electron band structure due to additional elastic fields generated by its larger ionic radius with respect to Pb^{2+} . This has to be taken into account when the spectra of different doped compounds are compared, because due to the strong influence of Ba on the electron configuration, the resonance conditions might change drastically with respect to the other samples.

Another obvious difference between the RRS spectra of pure and doped compounds is the intensity ratio of 2nd- and 1st-order scattering features. 2nd-order RRS is forbidden in non-polar ABO_3 -type relaxors and therefore this intensity ratio is sensitive for the polarity of the studied compounds. The fraction of 2nd-order RRS strongly decreases with A-site doping (Fig. 20). Doping the A-site with elements that have an isotropic outermost electron shell and thus possess LPE disturbs the coupling of atomic shifts and hence reduces the coherence and size of PNR. This model can be confirmed by considering PSN-Bi. Bi^{3+} is the only element among all others used to dope PSN, which shows the affinity to form LPE just as Pb^{2+} .

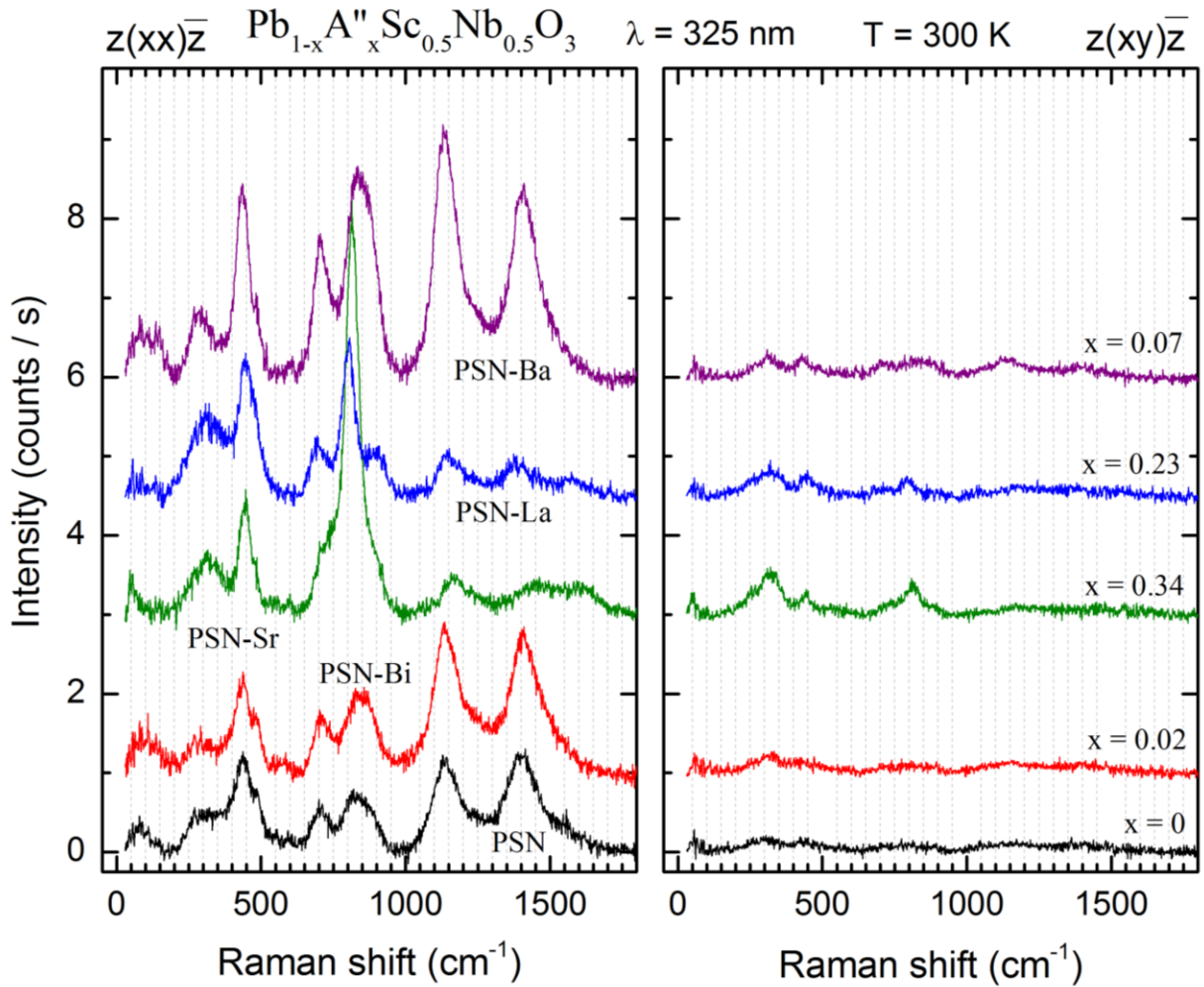


Fig. 19: Parallel and cross-polarized spectra of PSN-related compounds at ambient conditions. The spectra have been corrected for the contribution of photoluminescence.

Bi^{3+} substituting for Pb^{2+} induces extra charge in the structure, which leads to further random electric fields. Since Bi^{3+} possesses an ionic radius similar to that of Pb^{2+} , the induced elastic stress is small. Only for this type of A-site doping the fraction of 2nd-order RRS increases, although the content of Bi is only about 0.02. From previous studies it is well known that doping with Bi enhances the abundance of polar species, although the mean size of long-range ordered ferroelectric domains at low temperatures is smaller (Maier, et al., 2009). Therefore the enhanced 2nd-order RRS is due to the charge imbalance which promotes the nucleation of PNR.

Although La^{3+} also induces additional electric fields due to higher charge compared to Pb^{2+} and Ba^{2+} , the fraction of 2nd-order RRS is not enhanced with respect to the pure or Ba-doped compounds, which show a similar level of A-site substitution. From this it follows that the

major factor for the polar coupling is the system of LPE associated with the A-site cations. Thus, additional charge imbalance is not capable to overcome the coupling of off-centered Pb atoms disturbed by doping with cations with isotropic outermost electron shell.

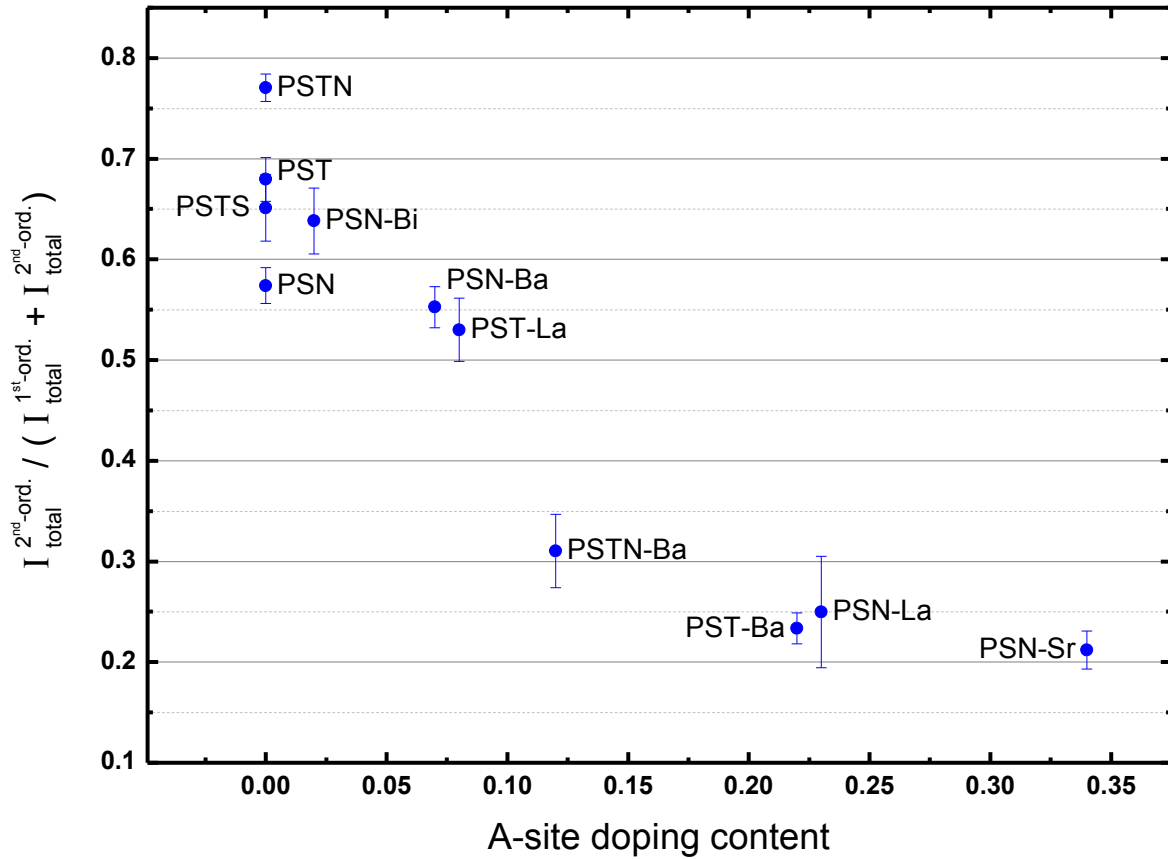


Fig. 20: Total fraction of 2nd-order resonance Raman scattering as a function of A-site doping content at ambient conditions. A-site substitution for Pb strongly affects the ratio of 1st- and 2nd-order RRS.

However, in spite of the amount of A-site substitution, B-site doping also influences the fraction of 2nd-order RRS. For pure PST the ratio is larger than compared with pure PSN. This is in accordance with the fact, that PST shows more coherence in polar coupling and a larger size of PNR (Mihailova, et al., 2005). Doping PST with Sn⁴⁺ (PSTS) slightly decreases the fraction of 2nd-order RRS, whereas doping with Nb⁵⁺ slightly increases it. The behavior of PST doped with Sn on the B-site is in accordance with the observations made for PSTS under pressure (Mihailova, et al., 2013). Partial substitution of Sn⁴⁺ for a pair of B³⁺ and B⁵⁺ cations disturbs the intermediate-range order of B-cation off-centered displacements in PNR and supports the development of antiferrodistortive BO₆ octahedral tilts. The unexpected enhancement of the 2nd-order RRS in PSTN may be explained by considering the intensity

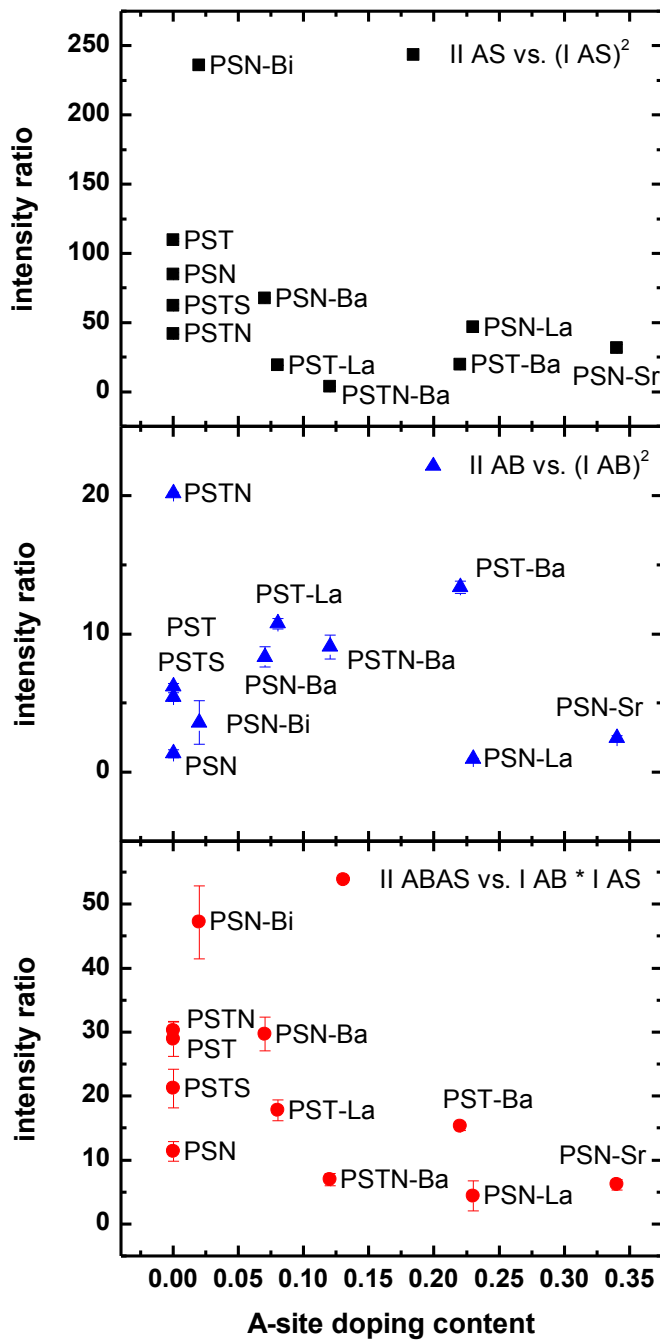


Fig. 21: Integrated intensity ratio of 2nd- and corresponding 1st-order RRS of different spectral features. The upper plot shows the ratio between antisymmetric stretching (I AS) and its overtone (II AS), in the middle antisymmetric bending (I AB) and its overtone (II AB) are concerned while at the bottom both fundamentals (I AB & I AS) and the combinational mode (II ABAS) are presented. The normalized intensity of the fundamental modes has been squared in order to follow the cross sectional dependence for two-phonon scattering.

order RRS and the square of the corresponding 1st-order scattering intensity. The intensity ratio between the antisymmetric stretching overtone (ca. 1400 cm⁻¹) and the fundamental

ratio of single 2nd-order scattering vs. the associated fundamental scattering features, since there are supposed to be different effects leading to the coupling of different vibrations. The high fraction of 2nd-order RRS for PSTN is probably due to an enhancement of the individual local polarity, although the overall coherence of polar coupling is disturbed.

Therefore deeper insights into the polar coupling processes can be gained by comparing the intensity ratio of 2nd- and 1st-order RRS for individual vibrations (Fig. 21). It becomes apparent that the two-phonon coupling between BO₆ antisymmetric bending vibrations and between antisymmetric stretching vibrations (overtones) as well as between both vibrations (combination) is very different for different compounds. The two-phonon scattering cross section is approximately proportional to the squared one-phonon cross section (Scott, 1969). Thus the intensity ratios shown in Fig. 21 are between 2nd-

(ca. 700 cm^{-1}) shows the highest similarity with the trend for the total 2nd-order scattering fraction. This indicates that the coupling between individual antisymmetric stretching vibrations is most sensitive to the polar species due to LPE associated with A-site cations. Thus, the coupling of antisymmetric BO_6 stretching vibrations is most likely related to the abundance as well as the mean size of polar spatial regions: ferroelectric domains or PNR. However, considering the ratio between the intensity of the antisymmetric bending overtone (ca. 880 cm^{-1}) and the fundamental (ca. 440 cm^{-1}) we obtain a rather different picture. For pure PSN and the related doped compounds there is only a considerable change when doping with Ba, whereas in particular La and Sr almost have no effect on the coupling of antisymmetric BO_6 bending vibrations. For Bi there is a slight increase but it is within the error.

For PSTN the ratio is considerably higher than for the majority of all other compounds, but it has to be taken into account that the spectral range of antisymmetric BO_6 bending around 430 cm^{-1} despite appropriate corrections is probably partially biased by a Raman peak from the glass of the used objective. In addition, B-site doping has different effects as compared to substitutions on the A site.

Increased ratios are also observed for Ba doped PST and PSTN. Since we know that incorporation of Ba induces local elastic stress and deformation of BO_6 octahedra as well as an imbalance in the bond lengths of the Pb-O-Ba linkages, the assumption can be suggested that the coupling of antisymmetric BO_6 bending vibrations is most sensitive for the individual polarity of distorted polar species on a local scale. This implies sensitivity for the individual, short correlated distortion of BO_6 octahedra with different neighboring A-site cations. Contrary to Ba doped PST and PSN, for PSTN-Ba the coupling of antisymmetric BO_6 bending vibrations is reduced. Consequently, simultaneous A- and B-site doping in this case reduces the individual polarity. Furthermore, the distribution of data points of the ratio between the intensity of the antisymmetric bending overtone and fundamental is very similar to the total RRS intensity (Fig. 18). If the assumption about the individual polarity is correct, it can be concluded that the RRS process overall is more sensitive for the individual polarity of distorted BO_6 octahedra i.e. for the local polar distortion on a length scale of a few atoms than for the mean size of polar spatial regions.

This can be explained by B-site cations compensating the elastic stress induced by Ba due to a corresponding chemical clustering of B-site cations in the following manner: If we consider two adjacent A-site cavities occupied by Ba and Pb, respectively, and think about their surroundings, the question appears how to distribute the three different B-site cations Sc, Ta and Nb among the cavity-building BO_6 octahedra. Assuming that Nb is preferably coordinated by Pb, while Ta prefers to position next to Ba, the distortion induced by Ba can be compensated by a certain positioning of the B-site cations. This can be enabled via different masses and B-O force constants of Nb and Ta. Nevertheless, this is only a presumption which cannot further be proven by the available data.

For PST-La the coupling between antisymmetric BO_6 bending vibrations increases compared to pure PST, while for PSN-La and PSN-Sr there is no significant change towards pure PSN. A small amount of La obviously does amplify the local distortion of BO_6 octahedra due to additional local electric fields and at the same time the level of doping is moderate enough in order not to suppress the off-center displacements of too many B-site cations, adjacent to La^{3+} . In addition, the substitution of Pb for La induces vacancies and they in turn are known to amplify the relaxor behavior. (Mihailova, et al., 2007 b). Both mechanisms cannot overcome the disturbance of the system of LPE due to heavy La doping on the A-site as in the case of PSN-La.

The coupling between individual antisymmetric BO_6 bending and stretching vibrations represented by combinational two-phonon scattering (ca. 1135 cm^{-1}) is the third interaction to consider. It shows an intermediate behavior compared with the coupling between vibrations enclosing the same atomic displacements. Thus, it most probably reflects the interplay between the individual local polarity and the abundance and/or the mean size of polar spatial regions, respectively. For heavily Ba doped PST the coupling decreases, whereas for PSN-Ba it increases. A small amount of Ba enhances the individual polar distortion while the system of LPE is only slightly disturbed. In the case of heavily doped PST the coupling between Pb atoms is hampered too strong and polar coupling cannot be realized only via an enhanced individual polarity. Thus it can be observed, that depending on different substitution on the A site the predominating type of polarity varies to be either determined by the mean size of polar spatial regions or the individual polarity of distorted BO_6

octahedra. It can be confirmed that the incorporation of Ba leads to a larger distribution in size and shape of polar clusters as already reported (Marinova, et al., 2006).

In conclusion, the coupling between internal BO_6 modes depends on different parameters. The coupling between antisymmetric BO_6 stretching vibrations strongly depends on the system of LPE and thus becomes weaker if Pb is partially substituted by a cation with an isotropic outermost electron shell e.g. Ba. By contrast, the coupling between antisymmetric

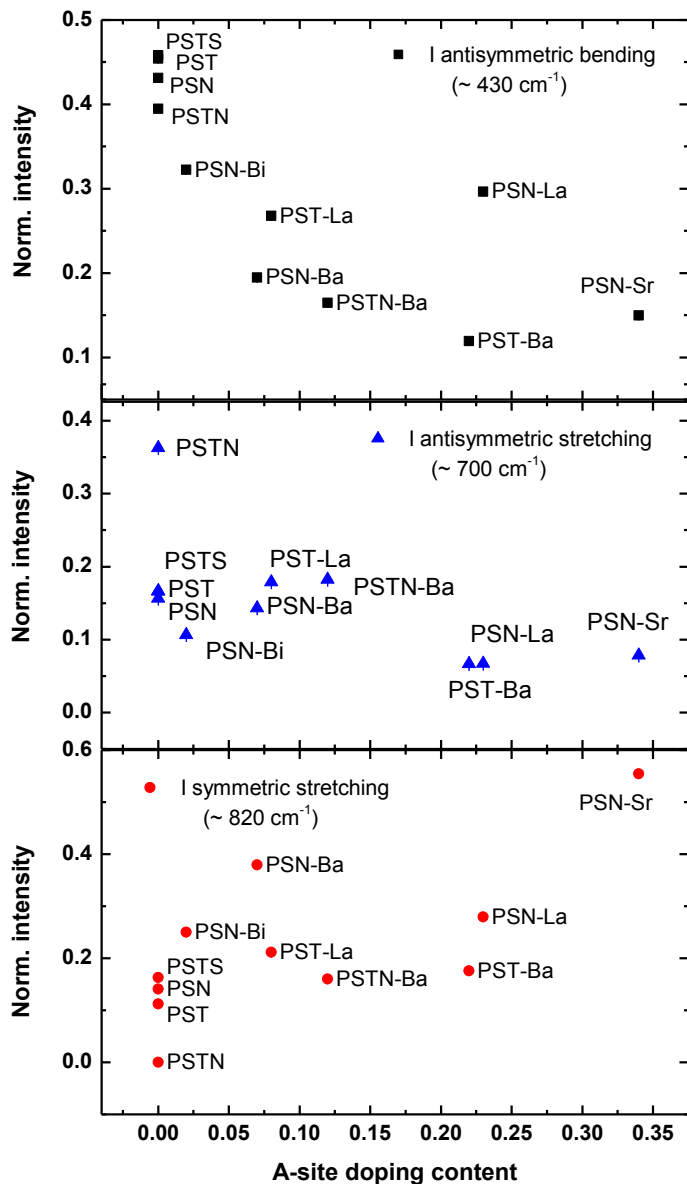


Fig. 22: Intensity of internal BO_6 vibrations for all measured samples normalized to the total intensity of 1st-order RRS. The upper plot shows antisymmetric BO_6 bending, the middle antisymmetric BO_6 stretching and in the bottom plot symmetric BO_6 stretching is concerned.

BO_6 bending vibrations does not depend as strong on the system of LPE but increases for A-site doping which favors the distortion of BO_6 octahedra. This is explicitly valid for doping with Ba since it possesses a larger ionic radius compared with Pb. Since the antisymmetric stretching is basically associated with changing bond lengths and the antisymmetric bending with varying bond angles, one can follow that there are at least two different coupling mechanisms responsible for the polarity of Pb-based relaxors.

As expected, the elastic fields generated by the incorporation of Ba seem to have a crucial impact on the antisymmetric bending vibrations of the BO_6 octahedra due to preferred changes in the O-B-O

bond angles. Hence, this should also be seen by considering the

normalized intensities of RRS from different internal BO_6 vibrations.

In Fig. 22 the scattering intensity from all three internal octahedral vibrations normalized to the total 1st-order RRS is plotted. If the intensity of antisymmetric bending is considered, it becomes apparent that the expected influence of Ba is absent and cannot be observed. Instead of becoming enhanced, the fraction of scattering from antisymmetric bending further decreases with Ba doping. This is most probably due to the presence of strong peaks in the range from 50 to 300 cm^{-1} for Ba doped PST and PSTN. For antisymmetric stretching vibrations the intensity decreases with increasing A-site doping content, while for PSTN the intensity is significantly higher than for all other compounds. However, the scattering from symmetric BO_6 stretching increases with increasing A-site doping. First of all the question should be answered, why Ba in contradiction to all expectations has no impact on the normalized intensity of antisymmetric BO_6 bending vibrations.

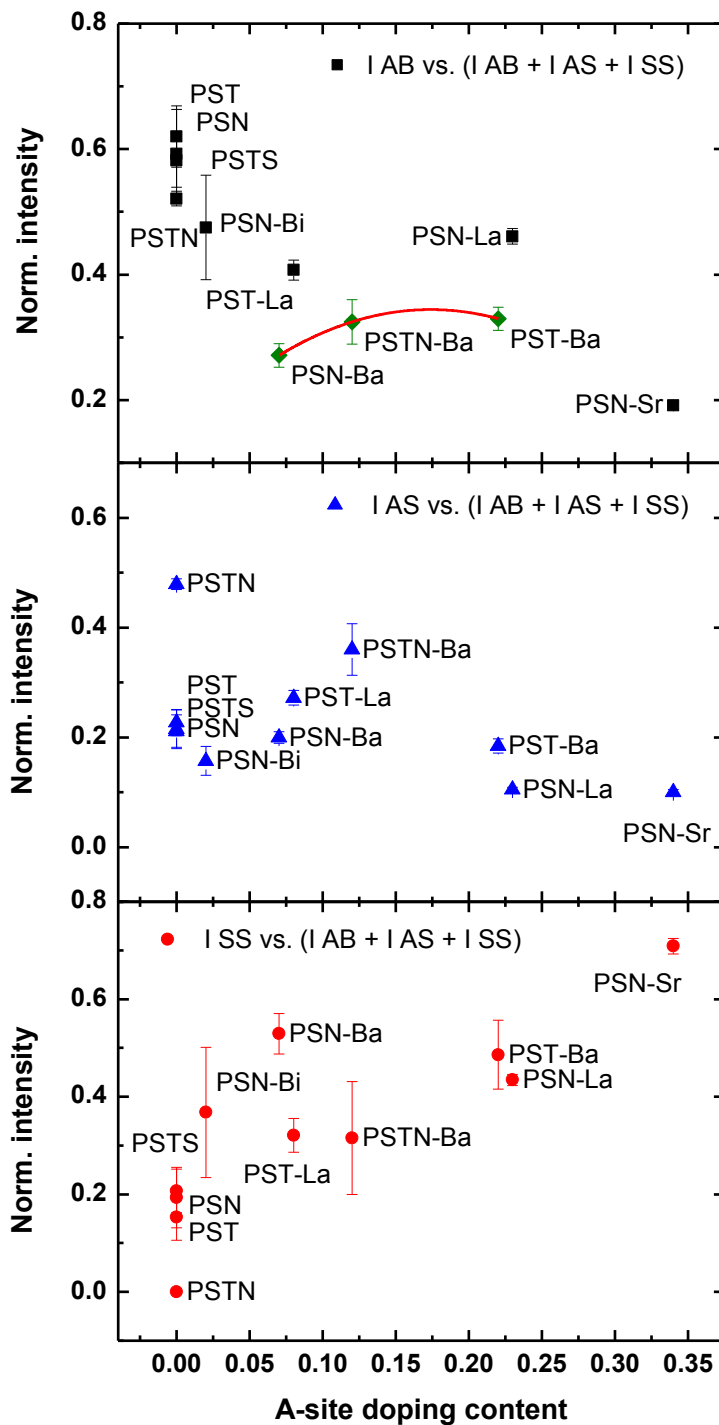


Fig. 23: Intensity of the single internal BO_6 vibrations with respect to the total scattering intensity from of all internal BO_6 vibrations. Especially for the fraction of antisymmetric bending in the upper plot it can be seen, that the Ba doped compounds behave differently compared with the other samples.

By comparing the normalized intensity of antisymmetric and symmetric BO_6 stretching in both Fig. 22 and Fig. 23 it can be seen that considerable differences can especially be seen for the Ba doped compounds.

By normalizing the intensity from single vibrations to the total scattering intensity of only all internal BO_6 modes (Fig. 23) it is possible to discriminate the effect of doping independently from the rest of the spectrum. Considering the upper plot of Fig. 23 it becomes apparent that the compounds doped with Ba follow another trend compared with the rest (green points). This trend is signified by a red spline. From this it follows that due to the strong influence of Ba on the electron band structure, the mechanism of resonance enhancement is different from the other materials. This is in accordance with the fact, that for Ba doped compounds an enhancement of A- and B-cation localized modes can be observed, although the electron-phonon coupling is most strong for internal BO_6 vibrations due to the formation of the energy gap by oxygen and B-cation electron levels.

Combining all observations one has to conclude that the enhancement of RRS for compounds doped with Ba is barely comparable with the compounds doped with La or Sr. In the following sections the different types of deformation for A-site cations with larger and smaller ionic radius with respect to Pb^{2+} are compared separately.

5.2.2 A-site substitution for Pb by cations with larger ionic radius: the effect of doping with Ba

In order to receive a more exact impression of how the doping of the perovskite A-site does influence the evolution of ferroic species i.e. PNR in corresponding materials, temperature dependent RRS spectra have been collected from PST-Ba. This compound is heavily doped with Ba substituting for Pb^{2+} . Since Ba^{2+} in the prevailing coordination has a larger ionic

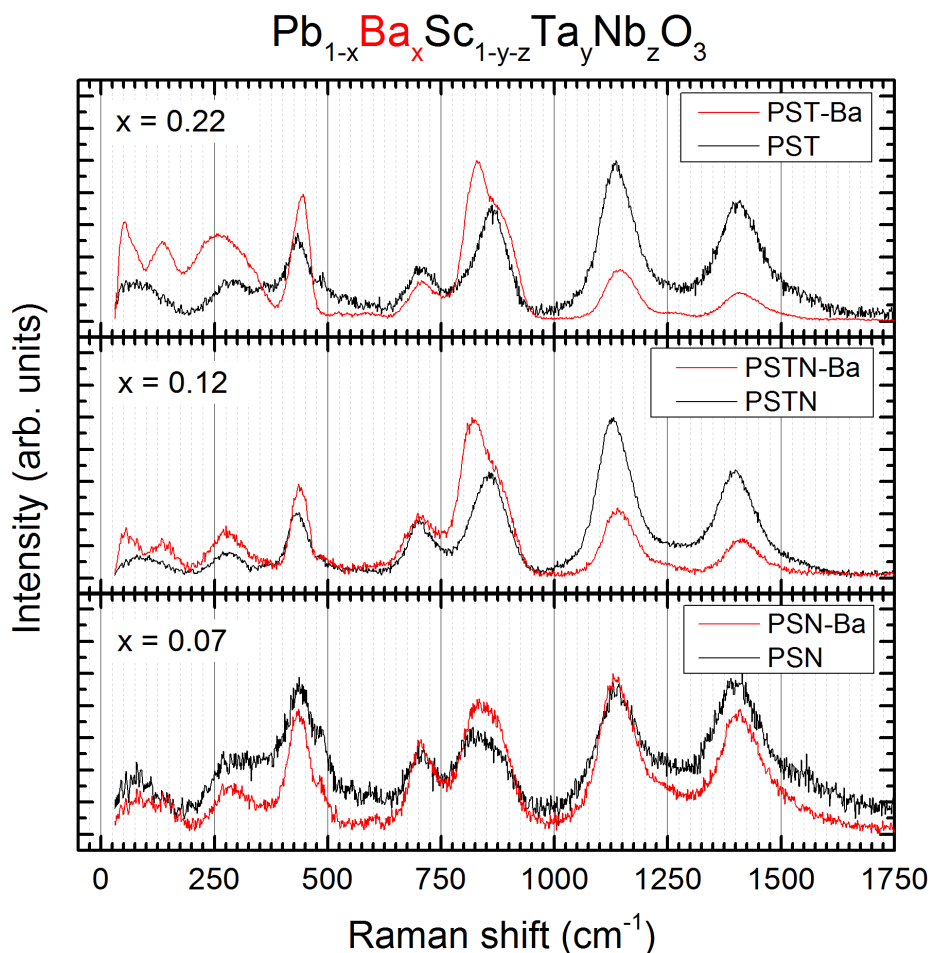


Fig. 24: Parallel polarized spectra of three different compounds with varying amount of Ta^{5+} and Nb^{5+} on the B-site and their corresponding materials doped with Ba^{2+} on the A-site at ambient conditions. The content of Ba increases from bottom to top. The spectra are normalized to unity for better comparability.

radius compared to Pb^{2+} , the tolerance factor of this compound is shifted to a higher value. The effect of Ba doping can be traced by considering Fig. 24. While a small amount of Ba, as for PSN has no striking impact on the spectrum, for PSTN-Ba and PST-Ba a significant change with respect to the undoped compounds can be observed. On the one hand the intensity of

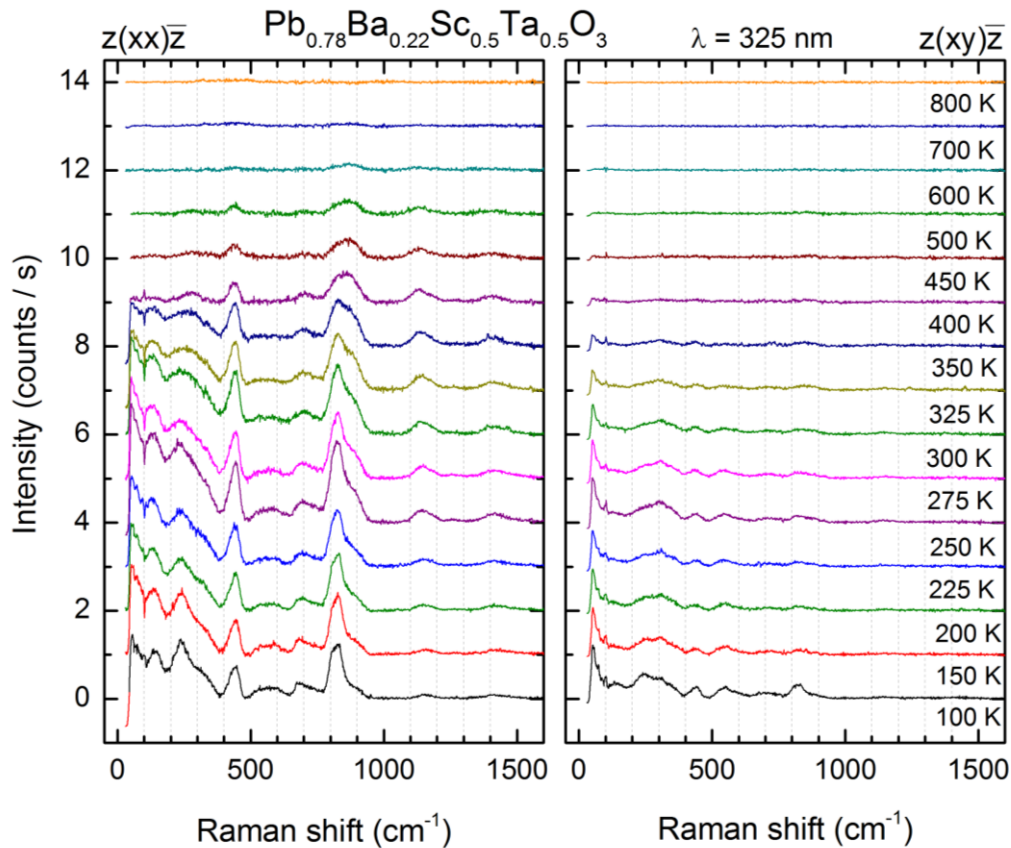


Fig. 25: Parallel and cross polarized RRS of PST-Ba as a function of temperature. Similar to pure PST no signals are detected at 800 K. Unlike pure PST, PST-Ba shows well pronounced RRS already well above T^* .

peaks related to the vibration of A- and B-site cations increases, while signals associated with 2nd-order scattering strongly decrease with respect to 1st-order scattering. Furthermore, a dominance of the symmetrical BO_6 stretching around 825 cm^{-1} can be recognized. For PST vs. PST-Ba this trend eventually continues.

The temperature evolution of RRS from PST-Ba can be seen in Fig. 25. At first glance it becomes apparent that as opposed to pure PST even above T^* RRS with distinctive intensity can be observed. By Raman spectroscopy under an applied electric dc field it has earlier been shown that the zero-field polar coupling of B-cations is suppressed in PST-Ba (Maier, et al., 2012). Thus, the appearance of well pronounced signals above T^* must be induced by

increased individual polarity on a local scale due to the distortion of BO_6 octahedra, that leads to a sufficient abundance of electric field magnitudes giving rise to RRS. Due to the incorporation of Ba the coupling of polar structural species has more anisotropic character than compared with pure PST (Maier, et al., 2012), for which the coupling explicitly is

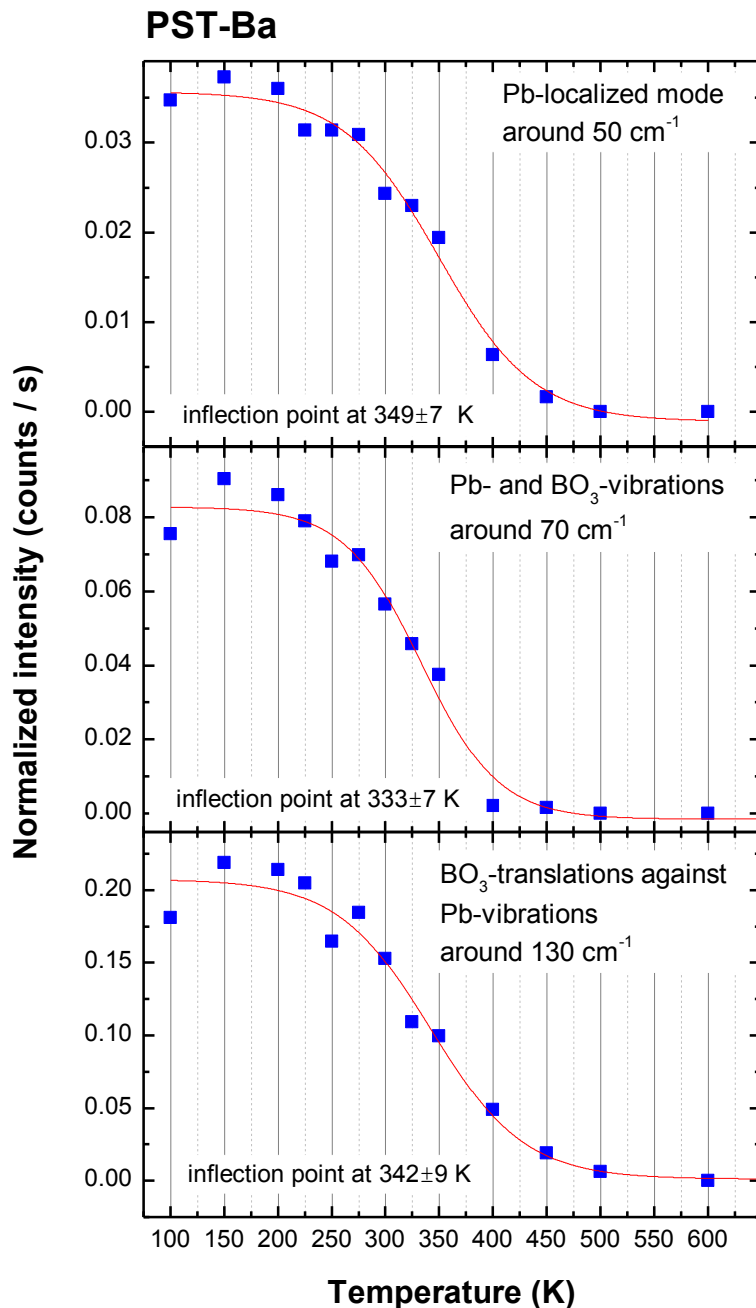


Fig. 26: Normalized intensity as a function of temperature for all three phonon modes with involved Pb-vibrations. The lines represent fits to data points by Boltzmann functions. The inflection points for all three modes are around 340 K. The trend of all three modes represents the evolution of fraction and size of PNR in PST-Ba with decreasing temperature.

preferably along the cubic body diagonal $[111]$, which corresponds to the rhombohedral axis of symmetry. This allows PNR to increase in size without the affinity to form coherent long-range ordered domains. With decreasing temperature the scattering intensity increases until finally at 100 K the peaks in the range from 50 to 300 cm^{-1} associated with localized A- and B-cation as well as translational BO_3 -A-cation vibrations dominate the spectrum together with signals related to symmetrical BO_6 stretching. Although the depolarization ratio in total is low, a significant development of the localized Pb mode can be observed in the cross polarized spectra. The former confirms the absence of ferroelectric long-range order at low

temperatures opposed to pure PST. Fig. 26 shows the temperature evolution of the normalized intensity of the low wavenumber modes related to Pb vibrations, combined Pb and BO_3 vibrations and BO_3 against Pb translations, respectively. The development of all three intensities has been fitted with a Boltzmann function, which represents the limited increase of a quantity. The curve progression is suggested to be directly correlated with the growth of PNR. Around 450 K in the range of T^* , the intensity starts to increase which is associated with preformed PNR starting to merge to larger polar clusters. The maximum increase can be observed around 340 K, where the curves have their inflection points. Subsequently the increase ends in saturation around 200 K, which is close to the freezing temperature T_f . Thus for PST-Ba RRS reveals the pure growth of PNR and their attendant electric fields, since no ferroelectric phase transition appears for PST-Ba (Marinova, et al., 2006).

5.2.3 A-site substitution for Pb by cations with smaller ionic radius: the effect of doping with La & Sr

Temperature dependent resonance Raman spectroscopy has been applied to La and Sr doped PSN in order to further examine the structural evolution of compounds for which antiferrodistortive BO_6 tilts are favored at ambient conditions. Fig. 27 shows the spectra of La and Sr doped PSN together with the spectrum of the pure model compound. From bottom to the top the content of A-site substitution increases and it can be seen that La and Sr have a very similar effect on the RRS. Compared with the effect of incorporation of Ba into the structure, it clearly appears that the nature of deformation is rather different. With increasing substitution for Pb the dominance of scattering related to symmetric stretching of BO_6 octahedra becomes more promoted. The temperature evolution of RRS can be seen in Fig. 28. Like for pure PSN, by cooling down from high temperatures the first signals can be detected around T^* at 450 K. The spectra develop rather differently with respect to pure as well as Ba doped relaxors. The overall intensity increases only slowly while especially the spectral feature around 800 cm^{-1} associated with symmetric BO_6 stretching attracts attention. There are also remarkable intensities for the peaks related to antisymmetric bending and stretching. The spectral region from 50 to 150 cm^{-1} is quite noisy, nevertheless,

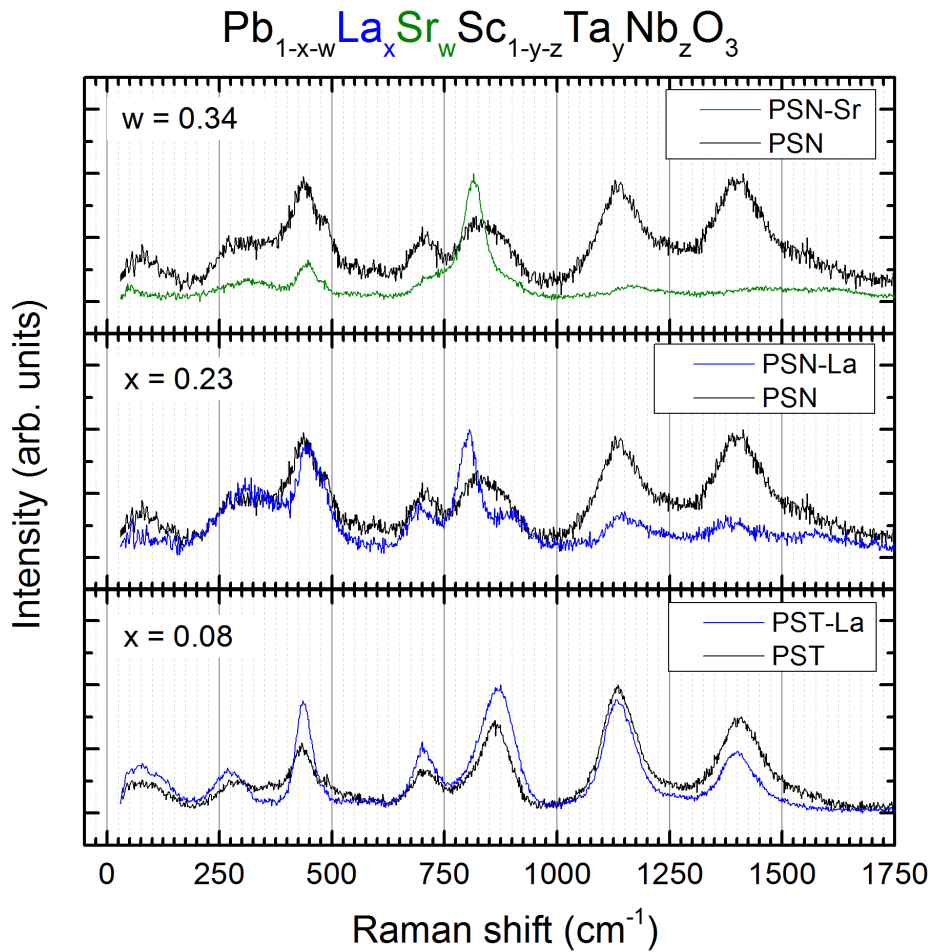


Fig. 27: Parallel polarized spectra of PST, PSN and their corresponding materials doped with La^{3+} or Sr^{2+} on the A site at ambient conditions, respectively. The amount of doping on the A-site increases from bottom to top. The spectra are normalized to unity for better comparability.

an increase of the intensity can be observed for this part of the spectrum for both polarizations. It is established due to earlier studies that heavy doping with La on the A-site induces the enhancement of antiphase BO_6 tilts at ambient conditions and facilitates the antipolar coupling between Pb cations, while simultaneously suppressing the off-centering of B-site cations (Maier, et al., 2011 a). This is in accordance with the spectra collected under resonance conditions, since the polarity associated with BO_6 octahedra appears strongly suppressed. Hence, the comparable high scattering intensity from the A-site localized vibrations can be suggested to arise from the dominance of antiferrodistortive ferroic order over the polar ferroic order.

In addition, the intensity of the peak around 800 cm^{-1} from symmetric BO_6 stretching seems also to be associated with the formation of antiferrodistortive tilts and thus with the doubling of the unit cell. Basically, the symmetric stretching does not carry polarity. Via long-range antiphase BO_6 tilts, the induced polarity by neighboring octahedra surrounding two different types of A-cations can order on a mesoscopic scale. In other words, due to the long range order of the antiferrodistortive structural species, the polarity induced by BO_6

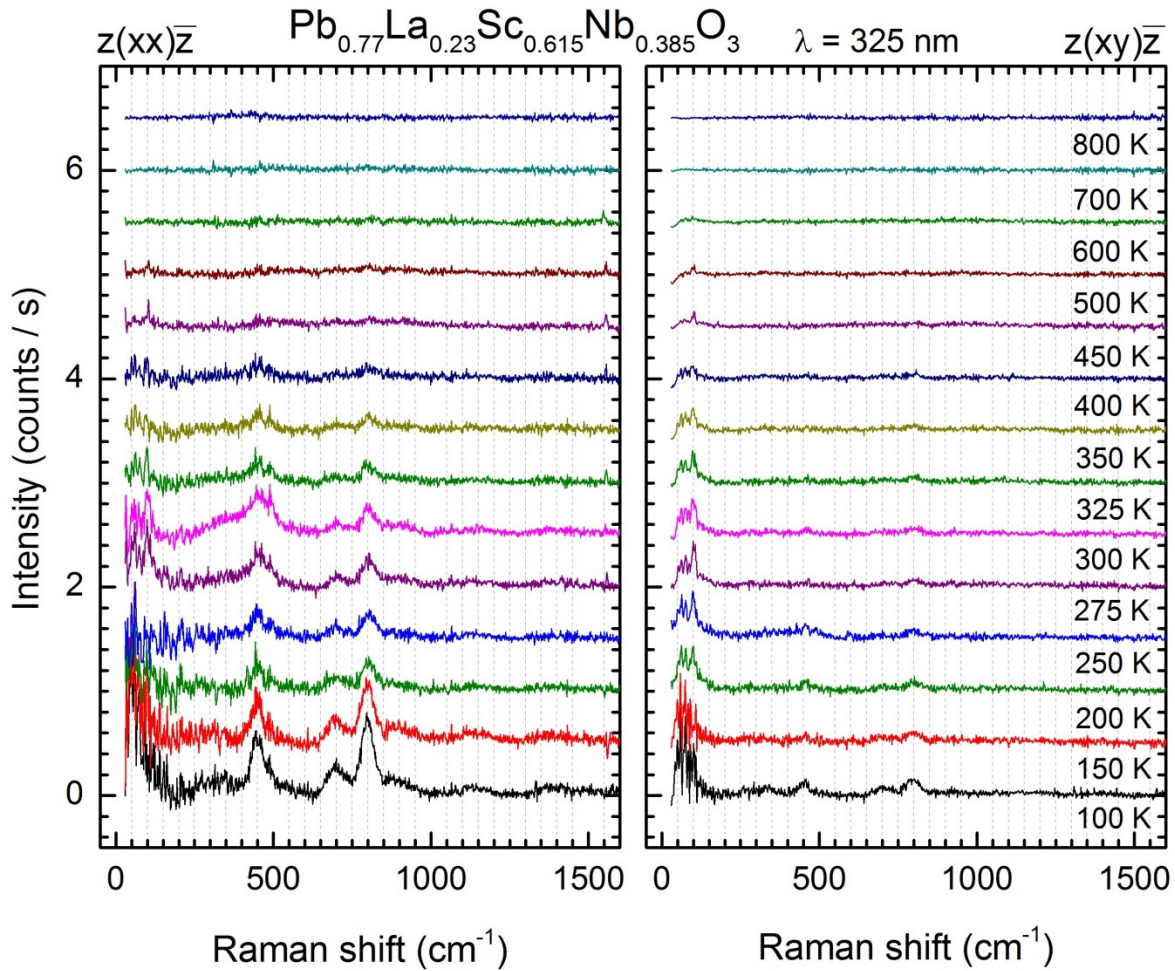


Fig. 28: Parallel and cross polarized resonance Raman spectra of PSN-La for different temperatures. At T^* considerable scattering signals appear, while 2nd-order RRS is nearly completely suppressed even at very low temperatures.

distortions can couple and hence the long-range antiphase tilts implicitly induce a certain type of polarity. This should work as long as there is a enough content of Pb-cations to create a sufficient amount of heteromorphic BO_6 surroundings. The presence of this peak for other materials shows, that at ambient conditions the structural state of lead-based perovskite-type relaxor ferroelectrics is characterized by the competitive behavior of antiferrodistortive and polar ferroic order. The temperature evolution of RRS from PSN-Sr

(Fig. 29) shows a similar behavior as PSN-La. The remarkable difference is made by the even more distinct attendance of the peak from symmetric BO_6 stretching. Even though the tolerance factor for PSN-Sr is smaller than for PSN-La, in fact despite of larger content of A-site doping, the missing extra charge and the high amount of A-site substitution leads to a facilitated antiferrodistortive structural state. The disturbance of the system of LPE is again

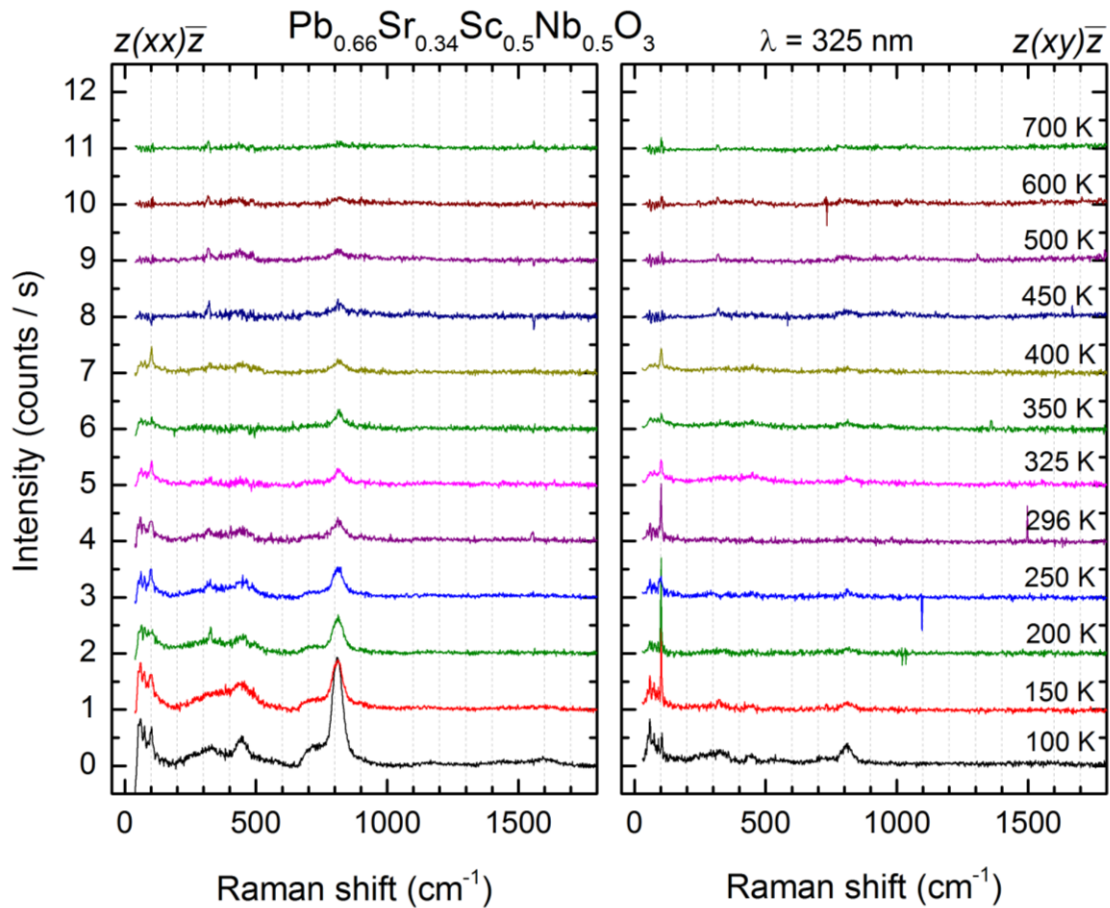


Fig. 29: Parallel and cross polarized resonance Raman spectra of PSN-Sr for different temperatures. In general 2nd-order RRS is nearly entirely suppressed, whereas especially a considerable intensity of the symmetrical stretching overtone can be observed. The overall scattering intensity remains minor even for low temperatures.

supposed to be the most striking effect when Pb is substituted by a cation with isotropic outermost electron shell and smaller ionic radius. Furthermore, due to homovalent doping in the form of Sr the individual distortion of BO_6 octahedra is continually reduced, although the coherence of antiphase ordered BO_6 tilting and therefore the accompanied polarity increases.

In summary, it can be stated that despite the additional random electric fields due to La^{3+} the polar coupling of off-centered B-site cations strongly decreases with A-site doping.

Especially due to the similarity of RRS from La and Sr doped compounds it must be concluded that the effect of random electric fields is not vital for the properties of perovskite-type relaxors. Instead the effect of local elastic fields and a lowered tolerance factor induced by different ionic radii of A-site cations, respectively, as well as the disturbance of the system of LPE has a striking impact on relaxor behavior. Thus the random electric field model is not appropriate to explain the origin of relaxor ferroelectric properties.

6 Conclusion

The lead-based perovskite-type $AB'_{0.5}B''_{0.5}O_3$ relaxor ferroelectric model compounds $PbSc_{0.5}Ta_{0.5}O_3$ (PST) and $PbSc_{0.5}Nb_{0.5}O_3$ (PSN) as well as their related A- and B-site doped derivatives have been studied by resonance Raman spectroscopy applying an excitation wavelength of 325 nm (3.815 eV), which corresponds to near the maximum of the optical dielectric permittivity and is above the energy gap formed by oxygen p and B-cation d level. Under resonance conditions an enhancement of BO_6 associated LO phonon modes namely antisymmetric bending (near 430 cm^{-1}) and stretching (near 700 cm^{-1}) associated with representation T_{1u} in the aristotype cubic perovskite structure due to Fröhlich interactions can be observed for all studied compounds. Furthermore, for PST and PSN intense 2nd-order resonance Raman scattering (RRS) from the same phonon modes is triggered in the form of overtones (near 860 and 1400 cm^{-1}) and a combination (near 1135 cm^{-1}).

RRS selection rules calculated by applying group theory analysis to electron and phonon states as well as the temperature clearly indicate that RRS exclusively arises from polar structural species. By cooling down from high temperatures RRS at first appears around T^* for pure compounds. The ratio between 2nd- and 1st-order RRS is predominantly sensitive for the coherence of polar off-centered shifts, while the fraction of two-phonon scattering strongly decreases with the disturbance of the system of lone-pair electrons associated with Pb^{2+} and Bi^{3+} , respectively. The pressure evolution of RRS collected from PST reveals that the polarity of the structure persists up to 10 GPa.

Doping with Ba^{2+} leads to a decrease in coherence of polar coupling and simultaneously enhances the individual polarity of BO_6 octahedra due to local elastic-field-induced distortion of B-cation surroundings. A selective development of the size of PNR can be observed by taking into account the temperature evolution of RRS from A-site cation localized as well as A-cation- BO_3 vibrations and translations.

Doping with La^{3+} and Sr^{2+} clearly hampers the mesoscopic polar ferroic order and leads to a decrease in the overall polarity. The enhancement of RRS related with symmetrical stretching around 800 cm^{-1} indicates that the doubling of the unit cell via rhombohedral antiphase octahedral tilting does implicitly induce coherence of polarity due to the distortion of BO_6 octahedra by heterogenic surroundings of different A-cations.

It becomes apparent that resonance Raman scattering is a promising method to study the complex inhomogeneous nanoscale structure of advanced ferroelectric materials due to high and selective sensitivity for polar structural distortions when the electron-phonon coupling is dominated by Fröhlich interactions. RRS allows it to compare the nature of deformation within different compounds and additionally enables the particular investigation of the local structure which is supposed to be responsible for relaxor behavior.

7 References

- Abrashev, M. V., Litvinchuk, A. P. & Thomsen, C., 1997. Froehlich-interaction-induced multiphonon Raman scattering in SrCuO₂ and Sr_{0.5}Ca_{0.5}CuO₂. *Physical Review B*, 55(14), p. R8638(R).
- Andreasson, J. et al., 2008. Electron-phonon interactions in perovskites containing Fe and Cr studied by Raman scattering using oxygen-isotope and cation substitution. *Physical Review B*, 78(23).
- Angel, R. J. et al., 2007. Effective hydrostatic limits of pressure media for high-pressure crystallographic studies. *Journal of Applied Crystallography*, 40(1), pp. 26-32.
- Aroyo, M. I. et al., 2006 a. Bilbao Crystallographic Server II: Representations of crystallographic point groups and space groups. *Acta Crystallographica Section A*, 62(2), pp. 115-128.
- Aroyo, M. I. et al., 2006 b. Bilbao Crystallographic Server I: Databases and crystallographic computing programs. *Zeitschrift Für Kristallographie*, 221(1), pp. 15-27.
- Aroyo, M. I. et al., 2011. Crystallography online: Bilbao Crystallographic Server. *Bulgarian Chemical Communications*, 43(2), pp. 183-197.
- Blinc, R., Gregorovič, A., Zalar, B. & Pirc, R., 2000. ²⁰⁷Pb NMR study of the relaxor behavior in PbMg_{1/3}Nb_{2/3}O₃. *Physical Review B*, 63(2), p. 024104.
- Bokov, A. A. & Ye, Z.-. G., 2006. Recent progress in relaxor ferroelectrics. *Journal Of Materials Science*, 41(1), pp. 31-52.
- Burns, G. & Scott, B., 1973. Index of refraction in 'dirty' displacive ferroelectrics. *Solid State Communications*, 13(3), pp. 423-426.

Bursill, L., JuLin, P., Hua, Q. & Setter, N., 1995. Relationship between nanostructure and dielectric response of lead scandium tantalate - (l) structure and domain textures. *Physica B: Condensed Matter*, 205(3-4), pp. 305-326.

Cardona, M. & Yu, P. J., 2005. *Fundamentals of Semiconductors*. 3rd ed. Berlin, Heidelberg, New York: Springer-Verlag Berlin Heidelberg.

Cohen, R. E., 1992. Origin of ferroelectricity in perovskite oxides. *Nature*, Volume 358, pp. 136 - 138.

de la Flor Martin, G., 2013. (*Doctoral dissertation*) *New computer tools of the Bilbao Crystallographic Server for materials structural analysis*, Bilbao: s.n.

de la Flor, G. et al., 2014. Resonance Raman scattering of perovskite-type relaxor ferroelectrics under nonambient conditions. *Physical Review B*, 90(6).

Du, H., Yao, X. & Wang, H., 2008. Relaxor-like behavior of bismuth-based pyrochlores containing Sn. *Journal of Electroceramics*, 21(1-4), pp. 222-225.

Dul'kin, E. et al., 2010. Evidence of local anisotropic strains in relaxor ferroelectrics below intermediate temperature T^* detected by acoustic emission. *Journal of Physics: Condensed Matter*, 22(22), p. 222201.

Ferraro, J. & Nakamoto, K., 1994. *Introductory Raman Spectroscopy*. London: Academic Press.

Granzow, T. et al., 2004. Change from 3D-Ising to Random Field-Ising-Model Criticality in a Uniaxial Relaxor Ferroelectric. *Physical Review Letters*, 92(6).

Jacobs, P. W. M., 2005. *Group Theory With Applications in Chemical Physics*. Cambridge, New York: Cambridge University Press.

Jeong, I.-K. et al., 2005. Direct Observation of the Formation of Polar Nanoregions in $\text{PbMg}_{1/3}\text{Nb}_{2/3}\text{O}_3$ Using Neutron Pair Distribution Function Analysis. *Physical Review Letters*, 94(14), p. 147602.

Kim, T. H., Kojima, S. & Ko, J.-H., 2012. Phase transition behaviors in relaxor ferroelectric [001]-poled $\text{Pb}(\text{In}_{1/2}\text{Nb}_{1/2})\text{O}_3\text{-Pb}(\text{Mg}_{1/3}\text{Nb}_{2/3})\text{O}_3\text{-PbTiO}_3$ single crystals studied by Brillouin light scattering and dielectric spectroscopies. *Journal of Applied Physics*, 111(5), p. 054103.

Kirsever, D. & Yılmaz, H., 2015. Electrical Properties of Lead-Free $\text{Na}_{1/2}\text{Bi}_{1/2}\text{TiO}_3$ Relaxor Ferroelectric Ceramics Doped with Hafnium or Zirconium. *Journal of the American Ceramic Society*.

Kitai, A. H., 1993. *Solid State Luminescence - Theory, materials and devices*. 1st ed. Dordrecht: Springer Netherlands.

Kuzmany, H., 2009. *Solid-State Spectroscopy - An Introduction*. 2nd ed. Heidelberg, Dordrecht, London, New York: Springer-Verlag Berlin Heidelberg.

La-Orauttapong, D., Toulouse, J., Robertson, J. L. & Ye, Z.-. G., 2001. Diffuse neutron scattering study of a disordered complex perovskite $\text{Pb}(\text{Zn}_{1/3}\text{Nb}_{2/3})\text{O}_3$ crystal. *Physical Review B*, 64(21), p. 212101.

Maier, B. J. et al., 2009. Effect of local elastic strain on the structure of Pb-based relaxors: A comparative study of pure and Ba- and Bi-doped $\text{PbSc}_{0.5}\text{Nb}_{0.5}\text{O}_3$. *Physical Review B*, 79(22).

Maier, B. J. et al., 2012. Influence of electric field on local phase transformations in relaxor ferroelectrics $\text{PbSc}_{0.5}\text{Ta}_{0.5}\text{O}_3$ and $\text{Pb}_{0.78}\text{Ba}_{0.22}\text{Sc}_{0.5}\text{Ta}_{0.5}\text{O}_3$. *Journal of Applied Physics*, 112(12), p. 124111.

Maier, B. J. et al., 2011 b. Structural state of relaxor ferroelectrics $\text{PbSc}_{0.5}\text{Ta}_{0.5}\text{O}_3$ and $\text{PbSc}_{0.5}\text{Nb}_{0.5}\text{O}_3$ at high pressures up to 30 GPa. *Physical Review B*, 84(17), p. 174104.

Maier, B. J. et al., 2011 a. Effect of La doping on the ferroic order in Pb-based perovskite-type relaxor ferroelectrics. *Physical Review B*, 83(13).

Marinova, V. et al., 2006. Structural, optical and dielectric properties of relaxor-ferroelectric $\text{Pb}_{0.78}\text{Ba}_{0.22}\text{Sc}_{0.5}\text{Ta}_{0.5}\text{O}_3$. *Journal Of Physics: Condensed Matter*, 18(31).

Mihailova, B. et al., 2011. The Structural State of Lead-Based Relaxor Ferroelectrics Under Pressure. *IEEE Transactions on Ultrasonics, Ferroelectrics and Frequency Control*, 58(9), pp. 1905-1913.

Mihailova, B. et al., 2008 b. Pressure-Induced Phase Transition in $\text{PbSc}_{0.5}\text{Ta}_{0.5}\text{O}_3$ as a Model Pb-Based Perovskite-Type Relaxor Ferroelectric. *Physical Review Letters*, 101(1), p. 017602.

Mihailova, B. et al., 2007 a. Resonance Raman scattering of relaxors $\text{PbSc}_{0.5}\text{Ta}_{0.5}\text{O}_3$ and $\text{PbSc}_{0.5}\text{Nb}_{0.5}\text{O}_3$. *Applied Physics Letters*, 90(4).

Mihailova, B. et al., 2002. Local structure and dynamics in relaxor-ferroelectric $\text{PbSc}_{1/2}\text{Nb}_{1/2}\text{O}_3$ and $\text{PbSc}_{1/2}\text{Ta}_{1/2}\text{O}_3$ single crystals. *Journal Of Physics: Condensed Matter*, 14(5), p. 1091–1105.

Mihailova, B. et al., 2005. Nanoscale phase transformations in relaxor-ferroelectric lead scandium tantalate and lead scandium niobate. *Zeitschrift für Kristallographie*, 220(8), pp. 740-747.

Mihailova, B. et al., 2007 b. Ferroic nanoclusters in relaxors: the effect of oxygen vacancies. *Journal Of Physics: Condensed Matter*, 19(24).

Mihailova, B. et al., 2007 c. Ferroic clustering and phonon anomalies in Pb-based perovskite-type relaxors. *Journal of Physics: Condensed Matter*, 19(27), pp. 275205-275214.

Mihailova, B. et al., 2015. Electric-Field-Induced Local Structural Phenomena in Pb-Based ABO₃-Type Relaxor Ferroelectrics. *IEEE Transactions on Ultrasonics, Ferroelectrics, and Frequency Control*, 62(1), pp. 7 - 17.

Mihailova, B. et al., 2008 a. High-temperature structural transformations in the relaxor ferroelectrics $\text{PbSc}_{0.5}\text{Ta}_{0.5}\text{O}_3$ and $\text{Pb}_{0.78}\text{Ba}_{0.22}\text{Sc}_{0.5}\text{Ta}_{0.5}\text{O}_3$. *Physical Review B*, 77(17).

Mihailova, B. et al., 2013. Chemically induced renormalization phenomena in Pb-based relaxor ferroelectrics under high pressure. *Journal of Physics: Condensed Matter*, 25(11), pp. 115403-115414.

Miller, S. C. & Love, W. F., 1967. *Tables of irreducible representations of space groups and co-representations of magnetic space groups*. s.l.:Pruett Press.

Munro, R. G., Piermarini, G. J., Block, S. & Holzapfel, W. B., 1985. Model line-shape analysis for the ruby R lines used for pressure measurement. *Journal of Applied Physics*, 57(2), p. 165.

Okawa, T., Imaeda, M. & Ohsato, H., 2002. Site occupancy of Bi ions and microwave dielectric properties in Ba_{6-3x}Nd_{8+2x}Ti₁₈O₅₄ solid solutions. *Materials Science and Engineering: B*, 88(1), pp. 58-61.

Paściak, M., Wołczyr, M. & Pietraszko, A., 2007. Interpretation of the diffuse scattering in Pb-based relaxor ferroelectrics in terms of three-dimensional nanodomains of the <110>-directed relative interdomain atomic shifts. *Physical Review B*, 76(1), p. 014117.

Quinn, J. & Yi, K.- S., 2009. *Solid State Physics: Principles and Modern Applications*. Dordrecht, Heidelberg, London, New York: Springer-Verlag Berlin Heidelberg.

Saïd, S. & Mercurio, J.- P., 2001. Relaxor behaviour of low lead and lead free ferroelectric ceramics of the Na_{0.5}Bi_{0.5}TiO₃-PbTiO₃ and Na_{0.5}Bi_{0.5}TiO₃-K_{0.5}Bi_{0.5}TiO₃ systems. *Journal of the European Ceramic Society*, 21(10-11), p. 1333.

Scott, J. F., 1969. Resonant Raman Effect in Semiconductors. *Physical Review*, 188(3), p. 1285.

Shannon, R. D., 1976. Revised effective ionic radii and systematic studies of interatomic distances in halides and chalcogenides. *Acta Crystallographica Section A*, 32(5), pp. 751-767.

Sherwood, P. M. A., 1972. *Vibrational spectroscopy of solids*. New York: Cambridge University Press.

Smith, G. & Dent, W. E., 2005. *Modern Raman Spectroscopy – A Practical Approach*. Chichester: John Wiley & Sons, Ltd.

Stephanovich, V. A., 2010. Tetragonal tungsten bronze compounds: relaxor versus mixed ferroelectric-dipole glass behavior. *Journal of Physics: Condensed Matter*, 22(23), p. 235902.

Tong, S., von Schirnding, Y. E. & Prapamontol, T., 2000. Environmental lead exposure: a public health problem of global dimensions. *Bulletin of the World Health Organization*, 78(9), p. 1068.

Waesermann, N., Mihailova, B., Gospodinov, M. & Bismayer, U., 2013. In situ high-temperature high-pressure Raman spectroscopy on single-crystal relaxor ferroelectrics $\text{PbSc}_{0.5}\text{Ta}_{0.5}\text{O}_3$ and $\text{PbSc}_{0.5}\text{Nb}_{0.5}\text{O}_3$. *Journal of Physics: Condensed Matter*, 25(15).

Waesermann, N. et al., 2011. Local structural phenomena in pure and Ru-doped $0.9\text{PbZn}_{1/3}\text{Nb}_{2/3}\text{O}_3 - 0.1\text{PbTiO}_3$ near the morphotropic phase boundary as revealed by Raman spectroscopy. *Physical Review B*, 83(21).

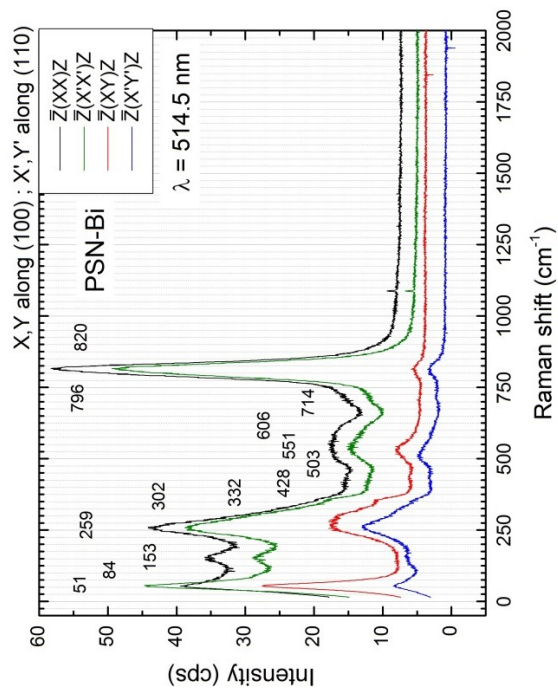
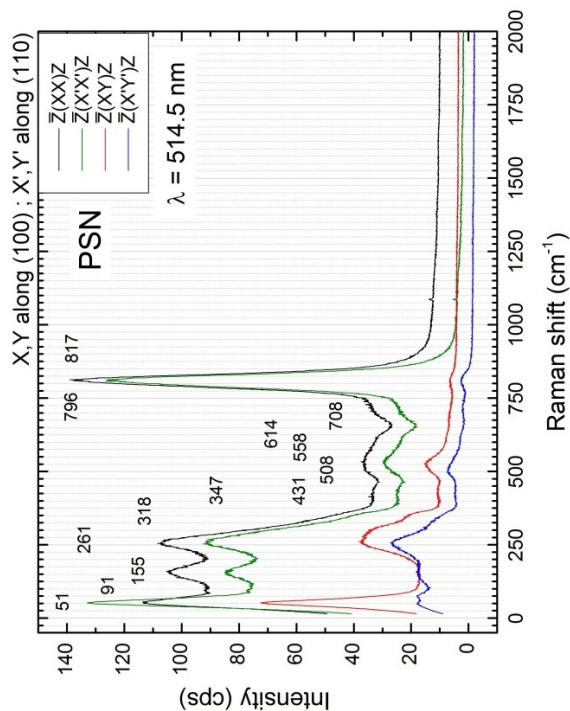
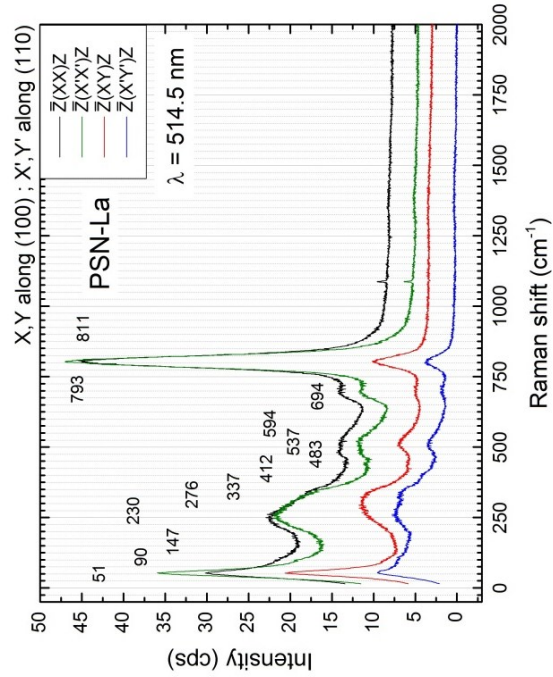
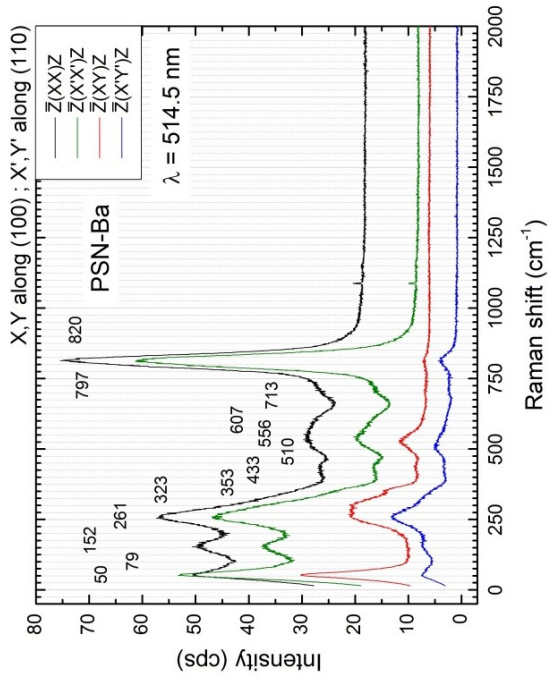
Welsch, A.-M. et al., 2011. Transformation processes in relaxor ferroelectric $\text{PbSc}_{0.5}\text{Ta}_{0.5}\text{O}_3$ heavily doped with Nb and Sn. *Zeit für Kristallographie*, 226(2), p. 126–137.

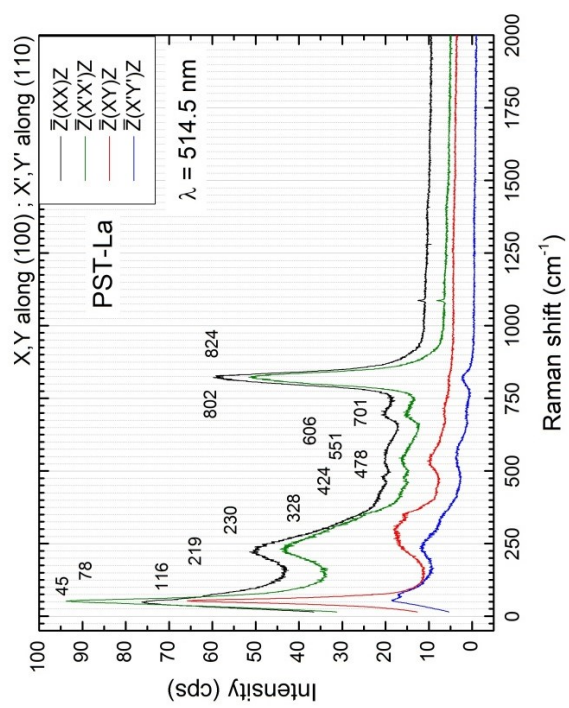
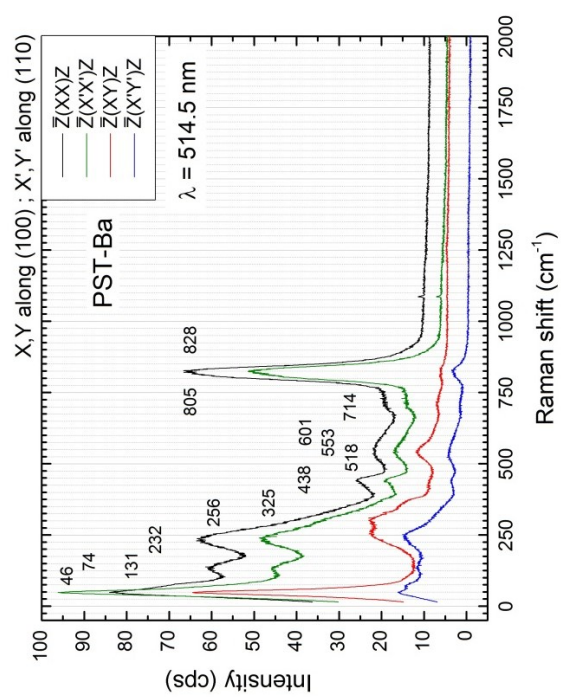
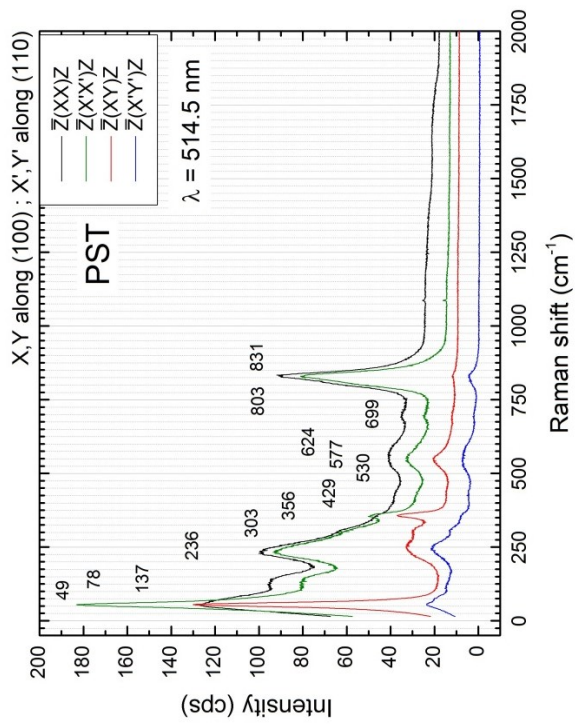
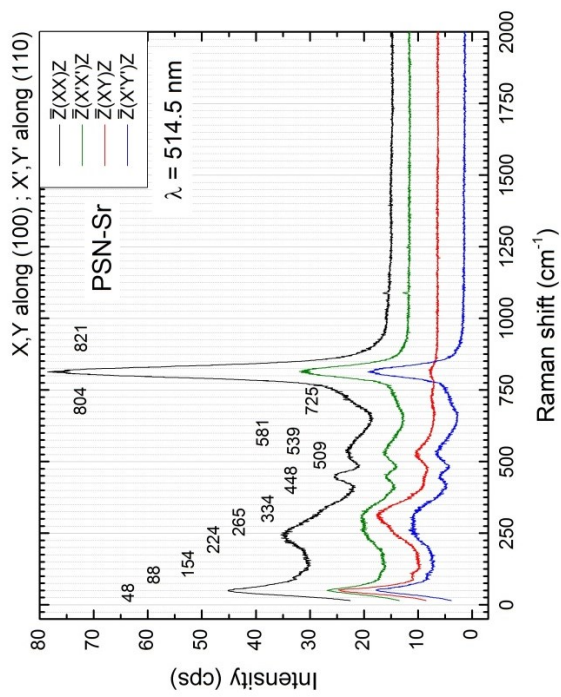
Wolfram, T. & Ellialtıoglu, S., 2006. *Electronic and Optical Properties of d-Band Perovskites*. Cambridge, New York: Cambridge University Press.

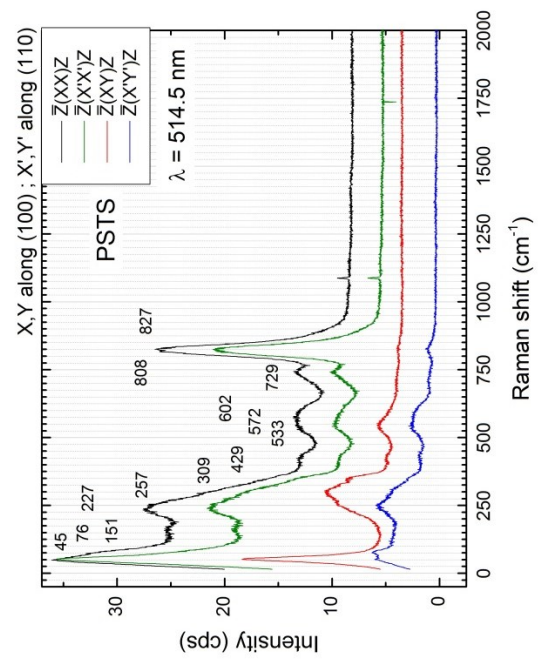
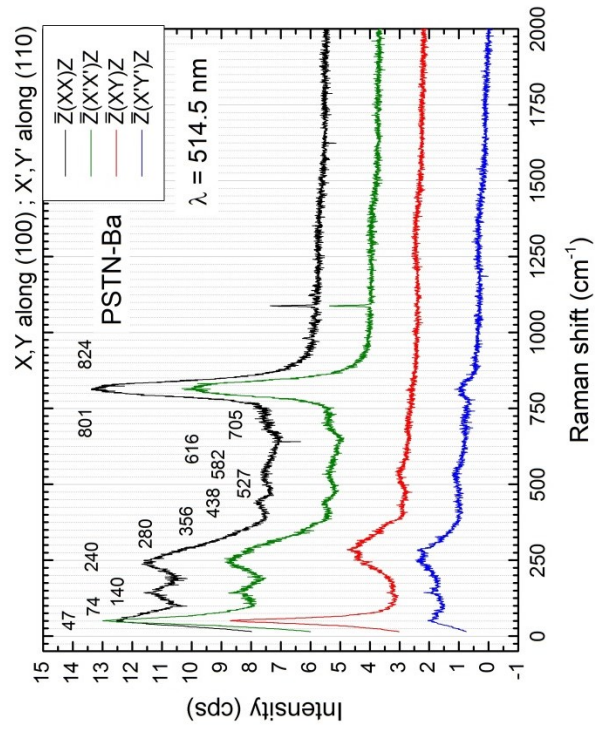
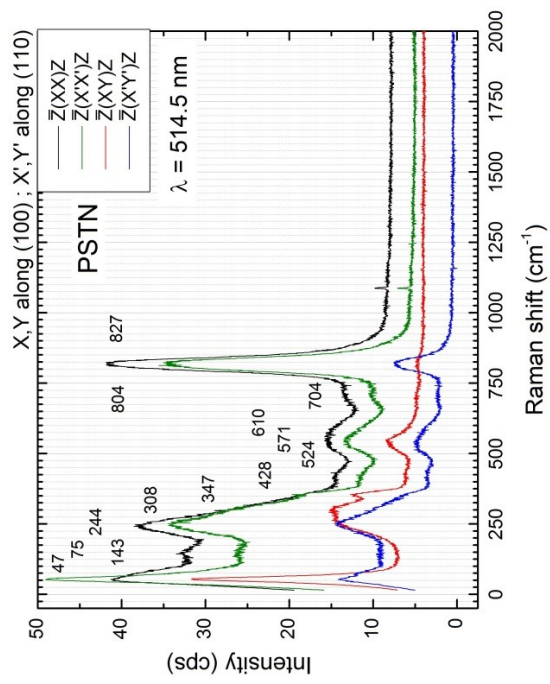
Yamashita, Y., Harada, K. & Saitoh, S., 1998. Recent applications of relaxor materials. *Ferroelectrics*, 221(1), pp. 29-36.

8 Appendix

8.1 Spectra collected under non-resonance conditions ($\lambda = 514.5$ nm)







8.2 Spectra collected under resonance conditions ($\lambda = 325$ nm)

